# LIGHT SCATTERING STUDY OF SALOL:

## EXPLORING THE EFFECT OF ROTATION-TRANSLATION COUPLING

by

Hepeng Zhang

A dissertation submitted to the Graduate Faculty in Physics in partial fulfillment of the requirements for the degree of Doctor of Philosophy, The City University of New York

2004

ProQuest Information and Learning Company
300 North Zeeb Road
P.O. Box 1346
Ann Arbor, MI 48106-1346

This manuscript has been read and accepted for the Graduate Faculty in Physics in satisfaction of the dissertation requirements for the degree of Doctor of Philosophy.

December 18, 2003
Date

Chair of Examining Committee

December 19, 2003
Date

Sultan Catto
Executive Officer

H. Z. Cummins

J. L. Birman

A. Z. Genack

M. Shattuck

H. Makse

Supervisory Committee

The City University of New York

# ABSTRACT

## LIGHT SCATTERING STUDY OF SALOL: EXPLORING THE EFFECT OF ROTATION-TRANSLATION COUPLING

by

Hepeng Zhang

Advisor: Professor H.Z. Cummins

Extensive light scattering experiments, including Brillouin, Raman and photon correlation spectroscopies, have been done to study the rotational and translational dynamics and their coupling in a glassforming liquid of anisotropic molecules, *Salol.* Pick-Franosch theory was used to fit the full set of data.

VH backscattering spectra were first fit with a hybrid function. This part of the analysis, together with photon correlation data, fixed all the parameters characterizing the pure rotational dynamics. The obtained rotational relaxation times agree with the results of dielectric and other experiments in the literature.

In VH $90^\circ$ fitting, the Pick-Franosch theory can produce excellent fits to all 23 spectra from 380 K to 210 K. At temperatures from 380 K to 310 K, the static shear viscosity values obtained from the fits agree with published rheological results. From 280 K to 210 K, the relaxation time for shear viscosity was found to be proportional to, and 15 times smaller than, the rotational relaxation time. The stretching coefficient $\beta$ for shear viscosity is smaller than that for rotational relaxation and the strength of rotation-translation coupling increases with decreasing temperature.

The difference spectra between VV 90° and VH backscattering spectra were analyzed last with the help of parameters obtained from both VH backscattering and VH90° fittings. The difference spectrum shows negative region-VV dip-at high temperatures and low frequencies. The difference spectra were first analyzed by a density-fluctuation-only model, which neglects the rotation-translation coupling. It can fit difference spectra well except where VV dip is. However, the Pick-Franosch theory, which includes rotation-translation coupling, can fit all the difference spectra including the VV dips. Thus we conclude that the VV dip is a consequence of rotation-translation coupling and related to -- but less apparent than -- the Rytov dip in the VH 90° spectra. The bulk viscosity was found to be roughly equal to the shear viscosity from 250 K to 350 K. Compared with the shear viscosity obtained from density-fluctuation-only fits, we found that rotation-translation coupling reduces the shear viscosity by roughly 15%.

# ACKNOWLEDGEMENTS

It is a great pleasure to acknowledge the assistance I have received in the course of my doctoral studies at the City University of New York. First and foremost, I would like to thank my advisor Herman Z. Cummins for his continuous support, practical tutelage and profound influence on my way of doing physics.

I am very thankful to Alexander Brodin who taught me all kinds of tricks for doing light scattering experiments and did part of the experiments reported in this thesis. I thank Robert Pick for his help in understanding the Pick-Franosch theory, which guides the analysis of the experimental data.

I thank the members in my thesis committee, Joseph Birman, Azriel Genack, Mark Shattuck and Hernan Makse for their guidance and help.

I thank Yoon-Hwae Hwang, Jeong-Ah Seo and Jiyong Oh for their hospitality during my visit to Pusan.

I thank Tracy Turner, Sue Turner and Victor Chang for their assistance and help.

I thank all my friends in China and U.S., especially Yang Lu, Yifan Song, Xiaohui Ni, Rong Fan, Bin Liu and Yinpang Yu. Through their help and friendship, they have contributed to this thesis.

Without my parents, who provided me continuous support and encouragement, this thesis would not have been possible.

# Contents

# List of Tables

# List of Figures

# Chapter 1

# Introduction

In simple liquids composed of isotropic molecules, the polarized (VV) light-scattering spectrum exhibits the familiar Rayleigh-Brillouin triplet due to density fluctuations, while the depolarized (VH) spectrum is much weaker, arising from higher-order processes such as various collision-induced effects [1]. For liquids of anisotropic molecules, an additional broad quasielastic component is observed in both VV and VH spectra with similar intensity and attributed to rotational dynamics.

In the late 1960's, Fabelinski, Starunov *et al* [2], [3], [4] and Stegeman and Stoicheff [5], while studying this rotational component in the VH spectrum of liquids composed of anisotropic molecules, discovered a previously unknown feature - a narrow dip centered at $\omega = 0$. The possibility of such a dip had been previously suggested by Leontovich [6] and Rytov [7] based on concepts of generalized hydrodynamics. Initially, the appearance of the dip was interpreted as evidence for propagating heavily damped shear modes. However, it was soon recognized that the origin of the "Rytov dip" is rotation-translation (RT) coupling whose most familiar consequence is the flow birefringence of liquids subjected to shear flow [8].

A theoretical analysis based on a two-coupled variable version of the Zwanzig-Mori formalism, which predicts the central dip observed in the high temperature VH spectra, was proposed by Andersen and Pecora [9] and by Keyes and Kivelson [10], [11],

[12]. In this approach, depolarized light-scattering is assumed to originate entirely from the rotational dynamics of the optically anisotropic molecules which is, however, modified by the RT coupling. While the Andersen-Pecora equations were originally derived using the Zwanzig-Mori formalism, Wang, in the small-$q$ limit appropriate to continuum hydrodynamics, showed that they can also be derived phenomenologically if the conventional hydrodynamic equations of motion of the liquid are extended to include rotational dynamics as well as coupling of rotational motion to shear flow [13], [14]. We note that in Andersen-Pecora theory rotational dynamics is described by a purely relaxational equation.

With decreasing temperature, the central (Rytov) dip in the VH spectrum disappears as the broad quasielastic line narrows; eventually a pair of symmetrically placed bumps appear on the wings of the rotational line and sharpen into well-defined transverse acoustic modes. This temperature evolution of the VH light-scattering spectra from doublet to singlet to triplet was studied in a series of papers by Wang *et al* [13], [14], [15], [16] who generalized the Andersen-Pecora analysis by explicitly introducing viscoelasticity, i.e. by replacing the shear viscosity constant $\eta_s$ by a memory function $\eta_s(t)$. However, as Wang noted, a similar viscoelastic generalization should also be included for the other transport coefficients in the dynamic equations [15], [16]. Dreyfus, Pick and their coworkers have further extended the phenomenological theory of depolarized light-scattering by introducing memory functions for all transport coefficients and writing the equation of motion of the rotational variable as a damped oscillator equation rather than a simple relaxation equation as used in the Andersen-Pecora theory. Their approach has been applied, so far, to depolarized light-scattering studies of the molecular glassformers *metatoluidine* [17], [18], [19] and *ortho-terphenyl* [20], [21].

While the VH spectrum is determined by rotational dynamics, the VV spectrum and its evolution with temperature primarily reflects the interaction of longitudinal sound waves with $q \sim 10^5$ cm$^{-1}$ with structural relaxation. Typically, for liquids of isotropic molecules, as $T$ decreases from above the melting temperature $T_M$ to below the glass-transition temperature $T_g$, the Brillouin linewidth $\Delta\omega_B$ first increases, passes through a maximum, and then decreases again, while the Brillouin peak position $\omega_B$ shifts monotonically to higher frequencies. The frequency increase occurs predominantly in the temperature range where $\Delta\omega_B$ is largest. As this temperature evolution occurs, another central component- the Mountain mode-due to viscoelasticity in supercooled liquids, appears, centered at $\omega = 0$, and narrows as $T$ decreases, eventually disappears inside of the instrumental resolution function.

For liquids of anisotropic molecules, as we have mentioned above, a broad quasielastic component due to rotational dynamics is present in the VV spectrum. It has been assumed in the literature for a long time that the VV spectrum is simply a sum of this rotational component and a typical density fluctuation spectrum appropriate for a liquid of isotropic molecules. This assumption is correct if rotational and translational motions are independent. However, as shown by flow birefringence and by the Rytov dip and transverse acoustic modes in the VH spectrum, these two degrees of motion are actually coupled. Thus Wang [16], Dreyfus *et al* [18], and Chappel and Kivelson [22] suggested the existence of RT coupling should invalidate the conventional assumption in analyzing the VV spectrum. Approximate expressions for the VV spectrum including rotation-translation coupling were given in Refs. [16] and [18].

Recently, Pick, Franosch, Dreyfus, and Latz, have undertaken a new unified analysis of both VV and VH light-scattering spectra using both a phenomenological analysis [18], [23] and a microscopic Zwanzig-Mori approach [24]. Their analysis provides a consistent theory of both VV and VH light-scattering spectra that includes all the effects of RT coupling and viscoelasticity. The light-scattering investigation of *Salol* reported in this thesis was undertaken primarily to see if the VV and VH light-scattering spectra of this much-studied molecular glassforming liquid could be successfully analyzed using this new formulation, and, in particular, to see if the effects of rotation-translation coupling on the VV spectra could be unambiguously demonstrated. As we will show, the theory is able to consistently describe our three sets of *Salol* spectra: VH backscattering, VH 90°, and VV 90°. In particular, we looked for - and observed - the signature of RT coupling in the VV spectrum predicted by these papers: a "VV-dip" feature in the $q$-dependent part of the VV spectrum which becomes negative at high temperatures and low frequencies.

The research in this thesis is also relevant to the ongoing effort to fully understand the dynamics of the liquid-glass transition. The fundamental quantitative theory of this transition is Mode Coupling Theory (MCT) which is primarily a microscopic theory of density fluctuation dynamics. Often, however, experimental data that is compared to MCT predictions mainly reflects orientational dynamics (as in our depolarized *Salol* spectra or dielectric spectroscopy). Thus, a detailed understanding of the interaction between orientational and translational dynamics should be included in the comparison of such data with MCT.

This thesis is organized as following. Chapter **2** is a brief review of the field of supercooled liquids and liquid-glass transition, including the basic phenomenology, features and a microscopic theory of the liquid-glass transition: Mode Coupling Theory(MCT), which provides important guiding information on how to model memory functions in data analysis. In Chapter **3**, we discuss the theory of low-frequency inelastic light-scattering in liquids and focus on the Pick-Franosch theory. In Chapter **4**, the experimental apparatus, including Brillouin, Raman and photon correlation spectroscopies, and our raw data are shown. In Chapter **5**, we discuss how all sets of spectra are analyzed using the Pick-Franosch theory. Finally, we conclude in Chapter **6**.

# Chapter 2

# Supercooled Liquid and The Liquid-Glass Transition

In everyday language, glass designates a fragile and transparent material, silica, well-known since antiquity as well as certain objects made of this material. In scientific language, especially in physics, glass is a non-crystalline solid that lacks the periodicity of crystals. This modern definition has gone far beyond its meaning in everyday language and, besides silica, includes the large group of molecular and polymeric glass, also more exotic materials such as amorphous metals.

Glass belongs to the oldest materials used by mankind [25]. Already in prehistoric times, our early ancestors used *obsidian*, a volcanic glass, to manufacture knives and arrow tips. Man-made glass is believed to have first emerged in the near east, some thousands of years BC in the form of glass beads. Nowadays glasses are almost ubiquitous in common lives, like window glasses and plastic soda bottles. Also glasses are materials of paramount importance in technology. Optical fibers are made of very pure amorphous silica, carefully doped. Some metallic glasses and alloys are of great technological importance [26]. Also glass is crucial in the processing of food [27] and preservation of insect life under extremes of cold and dehydration[28]. It is possible that most water in the universe is in glassy state [29].

Glasses are commonly made from supercooled liquids cooled through the liquid-glass transition. This Chapter is a brief review of the field of supercooled liquids and the liquid-glass transition. We will review the phenomenology in Sec.[**2.1**], together with ideas of potential energy landscape, which is a good way to get qualitative pictures of the phenomenology and some of the features discussed below. In Sec.[**2.2**], We list some basic features of supercooled liquids and the liquid-glass transition, including dynamics, relaxation, thermodynamics, heterogeneity and aging. In Sec.[**2.3**], Mode Coupling Theory, which is the only microscopic dynamical theory in this field and provides important quantitative information about the relaxation processes in supercooled and glassy materials, is discussed.

Excellent reviews can be found in the literature. References [30] and [31] are good general introductions for nonspecialists. A thorough coverage of topics and detailed discussions can be found in [32] and [33]. The relevance and usefulness of energy landscape idea in this field are elaborated in [34] and [35]. Besides these reviews, a few monographs, for example [25] and [29], are worthy of attention too.

## 2.1 Sketch of the Phenomenology and Potential Energy Landscape Description

The specific entropy $s$ as a function of temperature for a typical system, which can both crystallize and form a glass, is shown in Fig.[2-1] (a). Upon cooling from high temperatures, crystallization may happen at the melting temperature $T_m$, which is a first order phase transition and is marked by a discontinuous change in $s$. However, crystallization can be avoided by fast quenching. A liquid that manages to get below $T_m$ without crystallization is called a supercooled liquid. Instead of the discontinuous change observed in crystallization, $s$ changes smoothly in a supercooled liquid and is initially what would be expected by extrapolating the value of the liquid above $T_m$.

As a supercooled liquid is cooled to lower temperatures, its dynamics slows dramatically. Typically, viscosity increases by 15 orders of magnitude, as shown in Fig.[2-3]. At some temperature around $T_g$, the system will fall out of equilibrium when the molecules move so slowly that they do not have a chance to rearrange significantly before the temperature is lowed further. Thus, the experimentally observed $s$ will begin to deviate from the equilibrium value at this point. At temperatures not much lower than this, the time scales for molecular rearrangements become extremely long compared to the time scale of the experimental observations. The structure of this material is "frozen" for practical purposes, and we call it a glass.

It is important to emphasize that the glass transition is not a phase transition, because it doesn't involve discontinuous change or divergence in any physical properties, such as the heat capacity $C_p$, correlation time $\tau$, or correlation length $l$ and there is no known order parameter. It is purely a kinetic event which marks the crossing of the time scale of the experimental observations and the time scale for molecular rearrangements. Furthermore, glasses are not crystals or liquid crystals. They are liquids which are "frozen" on the time scale of experimental observation with microscopic structure indistinguishable from liquids. As indicated by Fig.[2-1] (a), different cooling rates will lead to system arrested in different glassy states. The slower a liquid is cooled, the longer the time is available for configurational sampling at each temperature, and hence the lower the temperature it can reach before falling out of liquid-state equilibrium. Consequently, $T_g$, which is approximately $0.6T_m$ [25], increases with increasing cooling rates. The properties of a glass, therefore, depend on the process by which it is formed. In practice, the dependence of $T_g$ on the cooling rate is weak ( $T_g$ changes by $3-5\ ^oC$ when the cooling rate changes by one order of magnitude [32]), and the transformation range is narrow, so that $T_g$ is an important, though approximate, material characteristic.

After this summary of basic phenomenology, we will discuss the concept of the potential energy landscape, which provides a convenient framework to understand the complex phenomenology in supercooled liquids and glasses. More than thirty years ago, Goldstein [36] pictured a glass-forming system as a point moving in a Potential

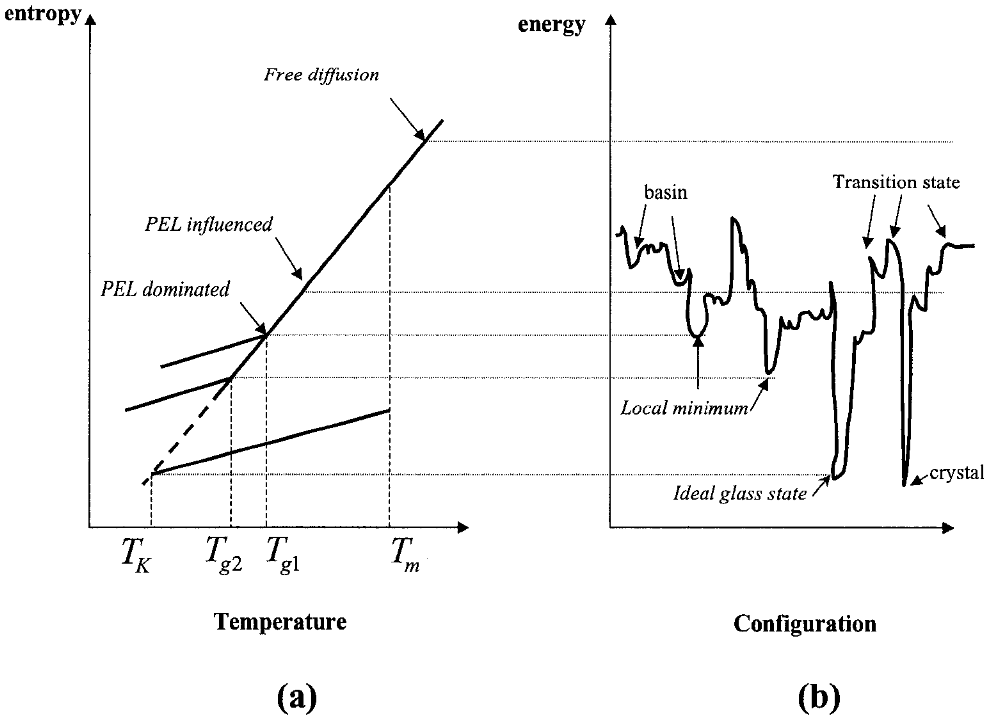

Figure 2-1: a) Specific entropy as a function of temperature for a liquid which can both crystallize and form a glass and the separation of temperature regions according to the role PEL plays. $T_m$ is the melting temperature, $T_{g1}$ and $T_{g2}$ are glass transition temperatures under two different cooling rates, $T_K$ is the Kauzmann temperature. b) Schematic PEL(Potential Energy Landscape) description of supercooling and glass formation. ( after [32] )

Energy Landscape(PEL), which is the name generally given to the potential energy function of an $N$-body system $F(\vec{r}_1, \ldots, \vec{r}_N)$, where the vectors $\vec{r}_i$ comprise position, orientation and vibration coordinates. In condensed phases, whether liquid or solid, every molecule experiences simultaneous interactions with numerous neighbors. Thus the landscape is a complex hyper-surface in a multidimensional space. For the case of $N$ structureless particles, possessing no internal rotational and vibrational degrees of freedom, the landscape is a $3N$-dimensional object. One PEL is shown schematically in Fig.[2-1] (b), where the total potential energy $F(\vec{r}_1, \ldots, \vec{r}_N)$ is the vertical axis and the horizontal axis represents all the coordinates $(\vec{r}_1, \ldots, \vec{r}_N)$. Goldstein suggested to focus on the local minima of the PEL, in which the system is supposed to be trapped at low enough temperature, in deeply supercooled and glassy regions. The system relaxes via occasional hoppings between neighboring minima. In the early 1980s, Stillinger and Weber [37] formulated this idea by partitioning the PEL into 'basins', which are called *inherent structures* and are essentially local minima as shown in Fig.[2-1] (b).

In [38], Sastry *et al* showed how the PEL is sampled in different temperature regions through detailed analysis of temperature dependence of the inherent structure system visits. From this work, the role of the PEL can be clearly seen. Fig.[2-2] shows the average inherent structure energy for a mixture of unequal-sized atoms, as a function of the temperature of the liquid [38]. In this calculation, molecular dynamics simulations of the binary mixture were performed to generate configurations. Periodically, the system's potential energy was minimized locally by Steepest-Decent or other standard minimization procedure, yielding inherent structures, the average energy of which is reported in the Fig.[2-2]. At high temperatures the inherent structure energy is virtually temperature-independent, and appears to have reached a plateau, when the system has sufficient kinetic energy to sample its entire energy landscape. In this regime, the system point can diffuse freely in the PEL. But as the temperature decreases below about $T = 1$, the system is unable to surmount the highest energy barriers due to the decreasing of kinetic energy, and is therefore forced to

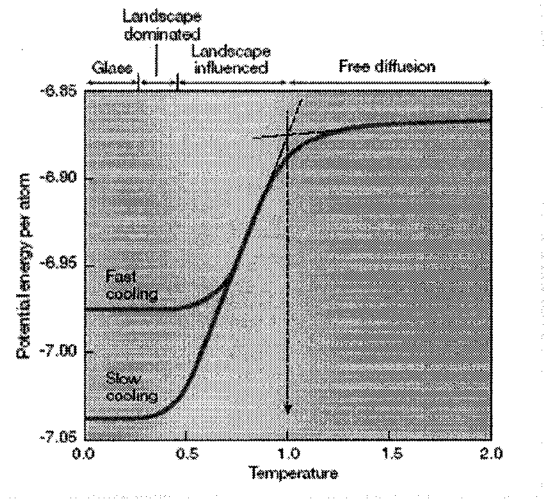

Figure 2-2: Average energy of inherent structure as a function of temperature of liquid from which the inherent structures were generated by potential energy minimization. (From [38])

sample deeper minima. When this happens, structural relaxation changes from exponential to stretched exponential(see below), and the activation energy (and entropy) associated with structural relaxation becomes super-Arrhenius [38]. Thus the PEL properties start to influence the dynamics. This calculation established a connection between changes in dynamics and the manner in which the static and thermodynamic energy landscape is sampled as a function of temperature. Fig.[2-2] also shows that at a low enough temperature the system becomes stuck in a single minimum, the depth of which increases as the cooling rate decreases. These correspond to different glassy states. The whole temperature-evolution picture is also shown schematically in Fig.[2-1].

A further approach, based on the idea of PEL and beyond the inherent structure analysis, has been introduced [39],[40],[41]. This approach studies saddles of the PEL and provides new insight in the analysis of the dynamic crossover taking place on lowering the temperature.

Recently, a "universal" concept of "jamming" has emerged to describe a many-body system blocked in a static configuration far from equilibrium, from which it takes too long a time to relax on the experiment time scale. The concept of "jamming" is thought to cover a diverse range of systems from the thermal systems like structural and spin glasses to non-thermal systems like granular matter and colloid (or emulsion) glass, where extremely slow relaxation can be found. Discussion of this concept is beyond the scope of thesis and can be found in several reviews [42], [43], [44].

## 2.2 Basic Features of The Glass Transition

In this subsection, some of the basic aspects of the glass transition, including dynamics, relaxation, thermodynamics, heterogeneity and aging, will be discussed. Among these five aspects, the discussion of dynamics and relaxation is closely related to our data analysis, while the others are less important and are included for the sake of completeness.

### 2.2.1 Dynamics

On approaching the glass transition, the dynamics in supercooled liquids slows down rapidly. The temperature dependence of viscosity for several glassforming liquids is shown in Fig.[2-3], in a so-called Angell plot. In this type of Arrhenius plot, temperature is scaled so that $T_g$ for each liquid occurs at the right edge of the graph ($x = T_g/T = 1$) and the viscosity axis is logarithmic. One definition of $T_g$ is the temperature at which the shear viscosity reaches $10^{13}$ Poise ($10^{12}$ $Pa \cdot s$). Supercooled liquids near $T_g$ flow extremely slowly, compared to $10^{-2}$ Poise for liquids like water, benzene, and ethanol at room temperature. The liquids shown in Fig.[2-3] have different temperature dependences as $T_g$ is approached. The viscosity of network glasses like $S_iO_2$ has almost an Arrhenius dependence while the viscosity of molecular liquids like $o-terphenyl$ is quite non-Arrhenius. People found that almost all materials fall between these two curves in this type plot. On the basis of this property and others, supercooled liquids have been classified by Angell as strong or fragile [45]. Strong liquids (e.g., $S_iO_2$) show Arrhenius temperature dependence and typically have three-dimensional network structures of covalent bonds. Fragile liquids (e.g., $o-terphenyl$) have quite non-Arrhenius behavior and typically consist of molecules interacting through nondirectional, noncovalent short-range interactions.

A property intimately related to the viscosity is the relaxation time for various processes, which also increases dramatically as a supercooled liquid is cooled toward $T_g$. This is illustrated in Fig.[5-5], where rotational relaxation time, measured by light-scattering techniques for *Salol*, are shown. The relaxation time at $T_g$ is about $10^2\ s$. This is an astoundingly long time compared to the *picosecond* or *nanosecond* relaxation times observed in "typical" liquids above $T_m$.

The temperature dependence of relaxation times (or the viscosity) for supercooled liquids is often described by the Vogel-Tammann-Fulcher (VTF) equation:

$$\tau = \tau_o \exp(\frac{B}{T - T_\infty}) \tag{2.1}$$

When $T_\infty = 0$, the familiar Arrhenius equation is recovered. Since $\tau$ in the VFT equation diverges when $T = T_\infty$, people [29] argued that it reveals a real phase transition at $T_\infty$, which is typically tens of degrees below $T_g$ and is close to the Kauzmann temperature $T_K$ discussed below. But current experimentally accessible liquid temperatures usually can't go below $T_g$, due to the extremely long relaxation time there. Thus this argument depends on a large temperature extrapolation, and is therefore questionable [29], [46].

In practice, the VTF equation, a three-parameter expression, is found to be able to fit the relaxation time over a limited temperature range. Free-Volume theory [47] gives a four-parameter formula, which has been shown to be able to cover the whole temperature range from above $T_m$ to $T_g$. The curve in Fig.[5-5] is a free-volume fit to the data by Eq.[2.2]

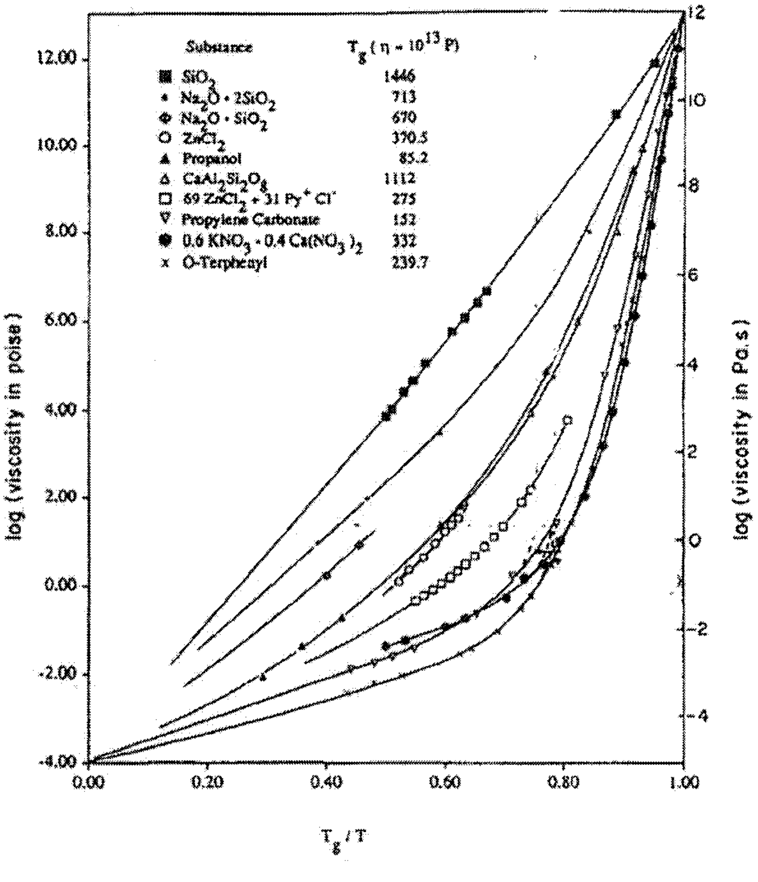

Figure 2-3: $T_g$ scaled Arrhenius plot for viscosity of different glassforming liquids (Angell plot) showing the spread between strong and fragile limits. (From [32])

$$\log(\tau) = A + \frac{B}{T - T_0 + \left[(T - T_0)^2 + CT\right]^{1/2}} \tag{2.2}$$

where if $C = 0$, the VFT is recovered.

### 2.2.2 Relaxation

Besides the dramatic increase of relaxation time, relaxation processes in the supercooled and glassy region also have other complicated and interesting aspects. The evolution with temperature of the density-density correlation function [48] for a supercooled Lennard-Jones binary mixture is shown in Fig.[2-4]. We notice that, with decreasing temperature, the relaxation changes from a single-step process into a two-step one. The first decay is single particle motion on a microscopic scale and depends only weakly on the temperature. The second relaxation, which depends strongly on temperature, usually involves many particles moving together collectively and is called $\alpha$ relaxation or structural relaxation. This two-step relaxation scenario will be discussed in detail later as an important prediction of Mode Coupling Theory.

Quantitative analysis of $\alpha$ relaxation reveals a striking and universal feature: it is non-exponetial. Often the Kohlrausch-Williams-Watts (KWW) or stretched exponential function is used to characterize $\alpha$ relaxation:

$$\phi(t) = \phi_o e^{-(t/\tau_k)^{\beta_k}} \tag{2.3}$$

where $\beta_{kww}$ is a value between 0 and 1. If $\beta_{kww} = 1$, a single exponential is recovered. The smaller the value of $\beta_{kww}$, the less exponential the correlation function. For experiments in the frequency domain, where the spectral density is usually measured, a Cole-Davison function

$$CD(\omega) = \frac{1}{\omega}[1 - (1 + i\omega\tau_{cd})^{-\beta_{cd}}] \tag{2.4}$$

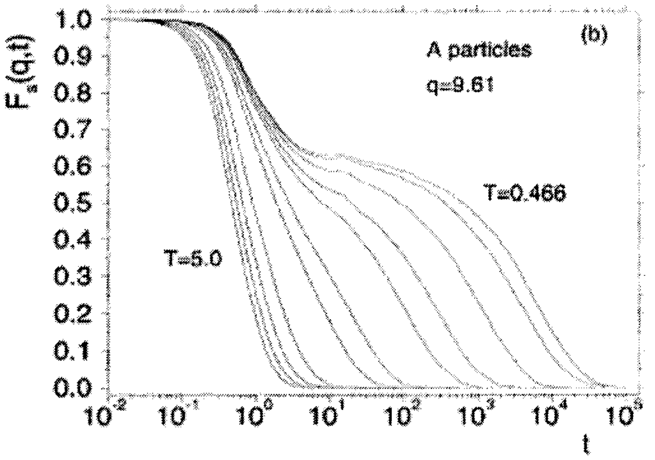

Figure 2-4: Evolution of Density-density Correlation function with decreasing temperature( from left to right: 5.0, 4.0, 3.0, 2.0, 1.0, 0.8, 0.6, 0.55, 0.5 ,0.475and 0.466) in a simulated binary L-J mixture. (From [48])

which is approximately the Fourier transform of the KWW function, is frequently used to analyze data. The relations between parameters in Eqs.[2.3] and [2.4] are given in [49] and Appendix **D**. A rough correlation has been noted between the value of $\beta_{kww}$ and the extent to which the temperature dependence of the relaxation time is non-Arrhenius. Generally, systems whose temperature dependences show the largest deviations from Arrhenius behavior (more fragile )also have very nonexponential relaxation functions[32]. In [34], Debenedetti and Stillinger associate the fragility and degree of stretching to the topographic characteristics of the PEL, namely the diversity of deep landscape traps and of the pathways of configuration space connecting the traps.

### 2.2.3 Thermodynamics

The most interesting thermodynamic quantity of a supercooled liquid is the specific entropy, $s$. Even though the system is not in state of lowest free energy, $s$ can

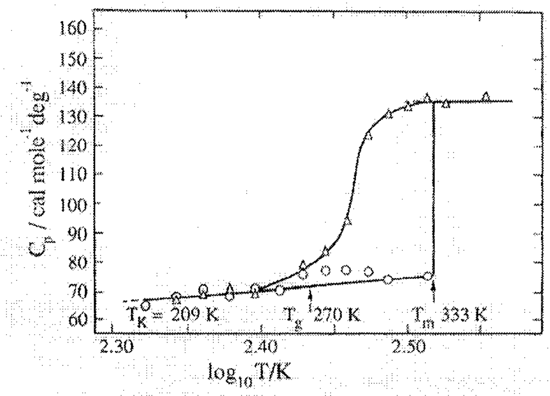

Figure 2-5: Isobaric heat capacities of the crystalline (circles), glassy and liquid (triangles)state of $(CH_3CO_2)_2 M_g \cdot 4H_2O$ as a function of temperature. ( From [50])

be determined in the usual way by integrating over the specific heat, which can be measured experimentally by differential scanning calorimetry. Fig.[2-5] shows a typical specific heat curve for the crystal (circles), liquid, supercooled liquid, and glass (triangles) from differential scanning measurements. On cooling, the specific heat $C_p(T)$ drops rapidly near $T_g$, due to the fact that many degrees of freedom have been 'frozen' during the transition from liquid to glass. The position of this drop can be used to define $T_g$.

The thermodynamic relation:

$$s(T_2) - s(T_1) = \int_{T_1}^{T_2} \frac{C_p(T)}{T} dT$$

allows a determination of the entropy from such $C_p(T)$ data. The typical result is shown schematically in Fig.[2-1] (a). The slope of $s$ versus $T$ is larger in the liquid phase than in the crystal. Thus, as the temperature drops, the entropies of the supercooled liquid and the crystal must approach one another. If the specific heat did not drop at $T_g$, and the rapid decrease of the liquid entropy were to continue to arbitrarily low temperature, then the liquid would eventually have the same entropy as the crystal. This extrapolated point is known as the "Kauzmann temperature", $T_K$. The vanishing entropy difference between the liquid and crystal led Angell *et al* [50] to propose an ideal glass transition. Contrary to the experimentally observed glass transition, this ideal glass transition would be a true thermodynamic transition that occurs precisely at $T_K$. At $T_K$, the entropy of the liquid is the same as the entropy of the crystal; therefore the system must be settled into the deepest of all the amorphous potential minima shown in Fig.[2-1] (b), which has been separated from other comparable deep minima, if there are any. It is this mutual inaccessibility that makes the entropy of the disordered ideal glass equal to that of the ordered crystal, assuming that difference of vibrational entropy in ordered and disordered system is small at this temperature. Both entropies would then approach $s = 0$ as $T \rightarrow 0$.

### 2.2.4 Heterogeneity

The nonexponentiality of $\alpha$ relaxation, discussed in Sec.[**2.2.2**], can be explained in two fundamentally different ways, as shown in Fig.[2-6]. One can imagine that a heterogeneous set of environments exists in a supercooled liquid; relaxation in a given environment is nearly exponential, but the relaxation time varies significantly among environments. Alternatively, one can imagine that supercooled liquids are homogeneous and that each molecule relaxes nearly identically in an intrinsically nonexponential manner. Evidences from optical-hole burning [52], NMR [53], single molecule spectroscopy [54], and computer simulation [55] indicate that the dynamics in the supercooled and glassy regions is spatially heterogenous.

One other interesting problem related to heterogeneity is the decoupling of translational and rotational diffusion from viscosity, in supercooled liquids below approximately $1.2T_g$ [52], [56], [57]. At higher temperatures, the translational diffusion coefficient and the rotational relaxation time are related to the shear viscosity $\eta_s$ by the Stokes–Einstein equation:

$$\eta_s = \frac{k_B T}{lD}$$

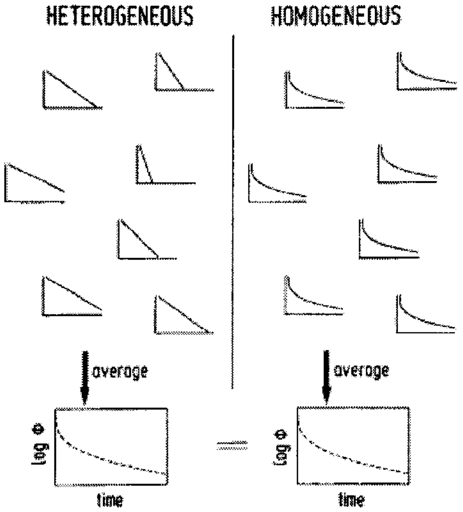

Figure 2-6: Heterogeneous and homogeneous explanations for a nonexponetial relaxation function. Different locations in the figure represents different locations in the sample. Observation of only the ensemble averaged relaxation function can not distinguish between these explanations. (From [51])

where $l$ and $D$ are the effective length and the diffusion coefficient of the molecule and by the Debye equation:

$$\eta_s = \frac{k_B T}{V} \tau_R \tag{2.5}$$

where $V$ and $\tau_R$ are the volume and the rotational relaxation time of the molecule. Below approximately $1.2T_g$, the inverse relationship between translational motion and viscosity breaks down, the so-called decoupling between $\eta_s$ and $D$. Near $T_g$, it is found that molecules translate faster than expected value from Stokes–Einstein equation and their viscosity, by as much as two orders of magnitude, whereas decoupling between rotational motion and viscosity is much weaker [53], [58]. This therefore means that, as the temperature is lowed, molecules on average translate progressively more for every rotation they execute. One plausible explanation comes from a heterogeneous picture of supercooled liquids. The basic idea is that translation and rotation average in different ways for a spatially heterogenous system [56].

### 2.2.5 Aging

For a system close to and below $T_g$, the thermodynamic state of the system deviates from that anticipated by extrapolations of higher temperature measurements because the system has lost equilibrium and the system is arrested in some quasi-equilibrium state as shown in Fig.[2-1]. Because this arrest is purely kinetic in nature, a period of waiting at a temperature not too far below $T_g$ will allow the system to find the state that is preferred by the thermodynamic driving forces, so the system will be observed to "relax". This means that any property of the system (e.g., specific entropy $s$) will show a time dependence. Because relaxation times depend upon the values of properties like $s$ (see eq 5), the rate at which relaxation occurs will also vary with time. Provided $T$ is not too far below $T_g$, and after sufficient time, all properties should ideally attain values expected from extrapolation of liquid properties above $T_g$. This process is called "annealing" when it is something which we can manipulate to our advantage (for instance, in stabilizing refractive index or enhancing mechanical strength and relaxing internal stress), or "aging" when it is happening naturally under conditions in which we would prefer it not to happen at all. Aging constitutes a serious practical problem in systems which have strongly nonexponential relaxation and $T_g$ not too far above ambient, which unfortunately is the case with many chain polymers used in practical applications. Because of aging, the polymer properties will change over time to the detriment of such things as the original molded dimensions and in some cases the mechanical strength.

## 2.3 Mode Coupling Theory

After this brief review of the basic phenomenology and features of the liquid-glass transition, we now discuss some theoretical aspects of the field. The lack of translational symmetry in supercooled liquids and glasses prevents the use of those sophisticated and powerful analytical methods used for the crystalline state and poses a great theoretical challenge for physicists, as commented on by P. W. Anderson [59] in 1995 :"The deepest and most interesting unsolved problem in solid state theory is probably the theory of the nature of glass and the glass transition."

Several phenomenological theories, e.g. Gibbs' cooperative relaxation and entropic theory [29], [60], and Cohen's free volume theory [29], [47], have been proposed and can successfully reproduce some of the features. However, before 1984 there was no microscopic theory which, starting from a microscopic Hamiltonian specified by the intermolecular potential, can both explain the occurrence of the glass transition and provide predictions for static and dynamic properties.

Beginning in 1984. a microscopic theory of the liquid-glass transition, usually referred to as the Mode-Coupling Theory (MCT), has been developed by W. Gotze, L. Sjogren and their coworkers [61], [65]. MCT is based on the Zwanzig-Mori theory and analyzes the nonlinear interaction between density fluctuation modes. The resulting equations were found to predict a dynamic transition from a normal liquid state to a structurally-arrested glass state and to also provide a detailed quantitative description of the dynamics.

In this section, we will discuss the "ideal" version of MCT. First, the statistical mechanics of many-body system is reviewed. Then, the Zwanzig-Mori formalism, which is the basis of MCT, is discussed. In subsection [**2.3.3**], the ideal version of MCT is derived and the predictions related to our data analysis are discussed.

### 2.3.1 Statistical Mechanics

We consider a system of $N$ identical classical particles of mass $m$, contained in a volume $V$. The $6N$-dimentional phase space is spanned by the particle positions $\overrightarrow{r}^i$ and momenta $\overrightarrow{p}^j$, $i, j = 1...N$. The particles $i$ and $j$ interact via a pair potential $e(\overrightarrow{r}^i - \overrightarrow{r}^j)$. Dynamical variables, $A(\vec{\Theta})$, are functions defined in the phase space, where $\vec{\Theta}$ represents all the coordinates and momenta in phase space: $\vec{\Theta} \equiv \vec{r}^1, ..., \vec{r}^N, \vec{p}^1, ..., \vec{p}^N$. The Hamiltonian

$$H(\vec{\Theta}) = \sum_{i=1}^{N} \frac{|\vec{p}^i|^2}{2m} + \sum_{i=1}^{N-1} \sum_{j=i+1}^{N} e(\vec{r}^i - \vec{r}^j)$$

plays the most important role in the system. First, it determines $\langle A \rangle$, the statistical average of $A$, via the phase space density distribution

$$\rho(\vec{\Theta}) \propto \exp(-H(\vec{\Theta})/k_B T),$$

where $T$ is the temperature. Also, the Hamiltonian determines the time evolution of $A(t)$, via the canonical equation of motion:

$$\frac{dA(t)}{dt} = \{H, A(t)\} = i\hat{L}A(t) \tag{2.6}$$

where $\{...\}$ is the Poisson Bracket and $\hat{L}$ is the Liouvillian, which is the Hermitian generator of the time evolution operator:

$$A(t) = \exp(i\hat{L}t)A(0) \quad .$$

### 2.3.2 Zwanzig-Mori Formalism

Taking the complete set of dynamical variables as vectors, a Hilbert space can be constructed if we define the inner product properly. In this thesis, following Gotze [61], the inner product is defined as the statistical average normalized by $k_B T$:

$$\langle A|B \rangle \equiv \langle A^* B \rangle / (k_B T) = \int d\Gamma \rho(\vec{\Theta}) A^*(\vec{\Theta}) B(\vec{\Theta})/(k_B T) \tag{2.7}$$

The fundamental idea of the Zwanzig-Mori Formalism is, first, to select a limited set of dynamical variables of interest in the Hilbert space, the so-called selected variables.

Then the time evolution of these selected variables is split into a part within the subspace spanned by them and a part orthogonal to them. The complicated dynamics of the orthogonal part can be represented by memory kernels, which can be further transformed and approximated. Finally the closed set of dynamic equations of the selected variables can be obtained.

First, we consider the simple case with one selected variable $A(t)$. In this case, we define a projection operator

$$\widehat{P} \equiv \frac{|A(0)\rangle\langle A(0)|}{\langle A(0)|A(0)\rangle} \tag{2.8}$$

which projects any vector onto $A(0)$, the initial value of the dynamical quantity $A(t)$. This operator has the following properties:

$$\begin{aligned} &(a) \quad \widehat{P}|A(0)\rangle = A(0) \\ &(b) \quad \widehat{P}\widehat{P} = \widehat{P} \\ &(c) \quad \langle B(t)|\widehat{P}|A(0)\rangle^* = \langle A(0)|\widehat{P}|B(t)\rangle \quad . \end{aligned}$$

Properties $(b)$ and $(c)$ are necessary and sufficient conditions for an operator to be a Hermitian projection operator. An operator that projects vectors onto the subspace orthogonal to $A(0)$ can be defined as

$$\widehat{Q} = 1 - \widehat{P} \, . \tag{2.9}$$

The Zwanzig-Mori Formalism (see [1], [62], [63] and Appendix **A**) gives an equation of motion for a dynamical variable $A(t)$ as:

$$\frac{dA(t)}{dt} = i\Omega A(t) - \int_o^t d\tau \Gamma(t-\tau)A(\tau) + F(t) \tag{2.10}$$

which has the form of a generalized Langevin equation. $\Omega$ is the vibration frequency, defined as

$$\Omega = \frac{\langle \hat{L}A(0)|A(0)\rangle}{\langle A(0)|A(0)\rangle} = -i\frac{\left\langle \dot{A}(0)|A(0)\right\rangle}{\langle A(0)|A(0)\rangle}$$

which vanishes if $A(0)$ has definite parity. $F(t)$ is the random force:

$$F(t) = \exp(i\hat{Q}\hat{L}t)\hat{Q}|\dot{A}(0)\rangle$$

which is orthogonal to $A\,(0)$, namely $\langle F\,(t)\,|A\,(0)\rangle = 0$. $\Pi(t)$ is the memory function :

$$\Pi(t) = \frac{\langle F(0)|\exp(-i\hat{Q}\hat{L}\hat{Q}t)|F(0)\rangle}{\langle A(0)|A(0)\rangle}$$

which is basically the time correlation function of the random force evolving in time via a "Projected Liouville Operator": $\hat{Q}\hat{L}\hat{Q}$. If we take the inner product of both sides of Eq.[2.10] with $|A\,(0)\rangle$ we get the equation of motion for the autocorrelation function:

$$\frac{dC(t)}{dt} = i\Omega C(t) - \int_o^t d\tau \Pi(t-\tau)C(\tau)$$

where $C(t) = \langle A(t)|A(0)\rangle$ and the last term $F(t)$ in Eq.[2.10] vanishes because $\langle F(t)|A(0)\rangle = 0$.

We can extend the Zwanzig-Mori Formalism from a single selected variable, $A$, to set of selected variables, which can be represented by a column vector: $\vec{A} = \begin{bmatrix} A_1 \\ \cdots \\ \cdots \\ A_M \end{bmatrix}$.

The correlation matrix can be defined as:

$$\overleftrightarrow{C}(t) \equiv \langle \vec{A}(t)|\vec{A}(0)\rangle, \text{ such that } C_{ij}(t) = \langle A_i(t)|A_j(0)\rangle \ .$$

Similar to the single variable case, we define projection operators as:

$$\begin{aligned} \widehat{P} &\equiv \langle ...|\vec{A}(0)\rangle \times \langle \vec{A}(0)|\vec{A}(0)\rangle^{-1} \times \vec{A}(0) \\ \hat{Q} &\equiv 1 - \widehat{P} \end{aligned} \tag{2.11}$$

where × stands for matrix multiplication. $\widehat{P}$ acts on any arbitrary vector $\vec{B}$ and projects it onto the subspace spanned by $\vec{A}(0)$. In this case, the equations of motion, written in a vector form, are:

$$\frac{d\vec{A}(t)}{dt} = i\overleftrightarrow{\Omega} \times \vec{A}(t) - \int_o^t d\tau \overleftrightarrow{\Pi}(t-\tau) \times \vec{A}(\tau) + \vec{F}(t) \tag{2.12}$$

where

$$\overleftrightarrow{\Omega} = \frac{\langle \widehat{L}\vec{A}(0)|\vec{A}(0)\rangle}{\langle \vec{A}(0)|\vec{A}(0)\rangle} = -i\frac{\langle \overrightarrow{\dot{A}}(0)|\vec{A}(0)\rangle}{\langle \vec{A}(0)|\vec{A}(0)\rangle}\ , \tag{2.13}$$

$$\vec{F}(t) = \exp(i\widehat{Q}\widehat{L}t)\widehat{Q}|\overrightarrow{\dot{A}}(0)\rangle \tag{2.14}$$

and

$$\overleftrightarrow{\Pi}(t) = \frac{\langle \vec{F}(0)|\exp(-i\widehat{Q}\widehat{L}\widehat{Q}t)|\vec{F}(0)\rangle}{\langle \vec{A}(0)|\vec{A}(0)\rangle}\ . \tag{2.15}$$

In most applications of the Zwanzig-Mori formalism [1], the selected variables are chosen to be "slow" variables and the Markov approximation is made for the memory matrix. Finally, a set of ordinary kinetic differential equations for the selected variables are obtained.

### 2.3.3 Mode Coupling Theory

In this subsection, we review Mode Coupling Theory (MCT) [61], [64], [65], which, in its simplest form, analyzes interactions between different modes of the density autocorrelation function in a liquid of spherical molecules. More elaborate versions of MCT that include orientational variables have been described but will not be considered here [115], [116]. First, the dynamical equations [2.30] of density-density autocorrelators, namely mode coupling equations, are derived from the Zwanzig-Mori formalism. Then the memory kernel in Eq.[2.25] is expressed as a function of products of the different modes of the density autocorrelation function. After making four approximations the resulting mode coupling equations are closed. In the third subsection, one important prediction of MCT, the two-step relaxation scenario, is discussed in detail. Finally, one semi-empirical function, the hybrid model, which mimics the two-step relaxation scenario and will be used in our data analysis later, is discussed.

### Mode Coupling Equation

The particle density fluctuation is the central quantity of mode coupling theory. The conservation of particle density reads :

$$\delta\dot{\rho}(\vec{r},t) = \triangledown \cdot \vec{J}(\vec{r},t) \tag{2.16}$$

where $\delta\rho(\vec{r},t)$ and $\vec{J}(\vec{r},t) = \rho(\vec{r},t)\vec{u}(\vec{r},t)$ are the local particle density fluctuation and density flux respectively. If we do the spatial Fourier transform

$$F(\vec{q}) = \int d\vec{r} \exp\left(i\vec{q}\cdot\vec{r}\right) F(\vec{r}) \tag{2.17}$$

to Eq.[2.16], we will get

$$\delta\dot{\rho}(\vec{q},t) = -i\vec{q}\cdot\vec{J}\left(\vec{q},t\right) \ ,$$

which says that local density fluctuation couples directly to the longitudinal flux: $J^L\left(\vec{q},t\right) = \vec{q}\cdot\vec{J}\left(\vec{q},t\right)$.

In this subsection, we choose $\delta\rho\left(\vec{q},t\right)$ and $J^L\left(\vec{q},t\right)$ as the selected variables and write down their equations of motion using the Zwanzig-Mori formalism. By eliminating $J^L\left(\vec{q},t\right)$, we end up with the Mode Coupling Equation, which is the starting point of MCT calculations. Readers not interested in mathematical details may go directly to Eq.[2.30].

Let's first write down some related static averages. The normalization of $\delta\rho\left(\vec{q},t\right)$

is given in terms of the structure factor

$$S_q = \frac{\left\langle \left|\delta\rho\left(\vec{q},0\right)\right|^2\right\rangle}{N} \tag{2.18}$$

Thus:

$$\left(\delta\rho\left(\vec{q},0\right)|\delta\rho\left(\vec{q},0\right)\right) = NS_q/\left(k_BT\right)$$

Also $S_q$ is related to the pair distribution function

$$g\left(r\right) = \left\langle \sum_{i\neq j} \delta(\vec{r} - \vec{r^i} + \vec{r^j}) \right\rangle /(Nn) \ ,$$

by

$$S_q = 1 + n \int d\vec{r} \exp(i\vec{q}\cdot\vec{r}) \left[g\left(r\right) - 1\right]$$

The Ornstein-Zernike equation relates $S_q$ to the direct correlation function $C_q$ :.

$$S_q = 1/\left[1 - nC_q\right]$$

Where $n$ is the average density: $n = N/V$.

Since the average velocity: $\langle u_i(\vec{r},0)^* u_j(\vec{r},0)\rangle = v^2$, where $v = \sqrt{k_BT/m}$ is the thermal velocity, we have $\left(J_\alpha\left(\vec{q},0\right)|J_\beta\left(\vec{q},0\right)\right) = N\delta_{\alpha\beta}/m$. Because of the time inversion symmetry, the inner products, like $\left(\delta\rho\left(\vec{q},0\right)|J^L\left(\vec{q},0\right)\right)$, $\left(\delta\dot{\rho}\left(\vec{q},0\right)|\delta\rho\left(\vec{q},0\right)\right)$ and $\left(\dot{J}^L\left(\vec{q},0\right)|J^L\left(\vec{q},0\right)\right)$, are zero. However $\left(\delta\dot{\rho}\left(\vec{q},0\right)|J^L\left(\vec{q},0\right)\right)$ and $\left(J^L\left(\vec{q},0\right)|\rho\left(\vec{q},0\right)\right)$ are nonzero: $\left(\delta\dot{\rho}\left(\vec{q},0\right)|J^L\left(\vec{q},0\right)\right) = \left(\dot{J}^L\left(\vec{q},0\right)|\delta\rho\left(\vec{q},0\right)\right) = -iq\left(J^L\left(\vec{q},0\right)|J^L\left(\vec{q},0\right)\right)$.

Suppose $\vec{A} = \begin{bmatrix} \delta\rho\left(\vec{q},t\right) \\ J^L\left(\vec{q},t\right) \end{bmatrix}$, thus the normalization matrix is

$$\begin{aligned} \langle\vec{A}(0)|\vec{A}(0)\rangle &= \begin{pmatrix} \langle\delta\rho\left(\vec{q},0\right)|\delta\rho\left(\vec{q},0\right)\rangle & \langle\delta\rho\left(\vec{q},0\right)|J^L\left(\vec{q},0\right)\rangle \\ \langle J^L\left(\vec{q},0\right)|\delta\rho\left(\vec{q},0\right)\rangle & \langle J^L\left(\vec{q},0\right)|J^L\left(\vec{q},0\right)\rangle \end{pmatrix} \\ &= \begin{pmatrix} NS_q/\left(k_BT\right) & 0 \\ 0 & N/m \end{pmatrix}. \end{aligned} \tag{2.19}$$

Following the definition Eq(2.11), the projection operator is

$$\widehat{P}\vec{B} = \langle ...|\vec{A}(0)\rangle \times \langle\vec{A}(0)|\vec{A}(0)\rangle^{-1} \times \vec{A}(0)$$

and acts on an arbitrary $\vec{B} = \begin{bmatrix} B_1 \\ B_2 \end{bmatrix}$,

$$\begin{aligned} \widehat{P}\vec{B} &= \begin{bmatrix} \langle\delta\rho\left(\vec{q},0\right)|B_1\rangle\frac{k_BT}{NS_q}|\delta\rho\left(\vec{q},0\right)\rangle + \langle J^L\left(\vec{q},0\right)|B_1\rangle\frac{m}{N}|J^L\left(\vec{q},0\right)\rangle \\ \langle\delta\rho\left(\vec{q},0\right)|B_2\rangle\frac{k_BT}{NS_q}|\delta\rho\left(\vec{q},0\right)\rangle + \langle J^L\left(\vec{q},0\right)|B_2\rangle\frac{m}{N}|J^L\left(\vec{q},0\right)\rangle \end{bmatrix} = \widehat{P}^L\vec{B} \\ &\text{where } \widehat{P}^L = \frac{k_BT}{NS_q}|\delta\rho\left(\vec{q},0\right)\rangle\langle\delta\rho\left(\vec{q},0\right)| + \frac{m}{N}|J^L\left(\vec{q},0\right)\rangle\langle J^L\left(\vec{q},0\right)| \quad . \end{aligned} \tag{2.20}$$

This means the matrix of projection operator $\widehat{P}$ is equivalent to a scalar operator $\widehat{P}^L$. This is due to the fact $\langle\delta\rho\left(\vec{q},0\right)|J^L\left(\vec{q},0\right)\rangle$ vanishes, which means the directions of $|\rho\left(\vec{q},0\right)\rangle$ and $|J^L\left(\vec{q},0\right)\rangle$ are orthogonal to each other in the Hilbert space. We can project the vector independently into two directions.

With all the static averages above, we can write

$$\begin{aligned}\overleftrightarrow{\Omega} &= \begin{pmatrix} \langle \delta\dot{\rho}(\vec{q},0)\,|\delta\rho(\vec{q},0)\rangle & \langle \delta\dot{\rho}(\vec{q},0)\,|J^L(\vec{q},0)\rangle \\ \langle \dot{J}^L(\vec{q},0)\,|\delta\rho(\vec{q},0)\rangle & \langle \dot{J}^L(\vec{q},0)\,|J^L(\vec{q},0)\rangle \end{pmatrix} \times \\ &\quad \begin{pmatrix} \langle \delta\rho(\vec{q},0)\,|\delta\rho(\vec{q},0)\rangle & \langle \delta\rho(\vec{q},0)\,|J^L(\vec{q},0)\rangle \\ \langle J^L(\vec{q},0)\,|\delta\rho(\vec{q},0)\rangle & \langle J^L(\vec{q},0)\,|J^L(\vec{q},0)\rangle \end{pmatrix}^{-1} \\ &= \begin{pmatrix} 0 & q \\ \dfrac{qk_BT}{mS_q} & 0 \end{pmatrix}\end{aligned} \tag{2.21}$$

The random force is

$$\vec{F}_1(\vec{q},t) = \exp(i\widehat{Q}^L\widehat{L}t)\widehat{Q}^L\overrightarrow{\dot{A}} = \exp(i\widehat{Q}^L\widehat{L}t)\widehat{Q}^L\begin{pmatrix} \dot{\rho}(\vec{q},0) \\ \dot{J}^L(\vec{q},0) \end{pmatrix} \tag{2.22}$$

where $\widehat{Q}^L = 1 - \widehat{P}^L$. Thus $\vec{F}_1(\vec{q},0) = \widehat{Q}^L\begin{pmatrix} |\dot{\rho}(\vec{q},0)\rangle \\ |\dot{J}^L(\vec{q},0)\rangle \end{pmatrix} = \begin{pmatrix} 0 \\ i\frac{1}{m}|F(\vec{q},0)\rangle \end{pmatrix}$,

$$|F(\vec{q},0)\rangle = m\widehat{Q}^L\widehat{L}|J^L(\vec{q},0)\rangle\ . \tag{2.23}$$

Therefore the memory matrix is

$$\begin{aligned}\overleftrightarrow{\Gamma}(t) &= \tfrac{\langle \vec{F}_1(0)|\exp(-i\widehat{Q}^L\widehat{L}\widehat{Q}^Lt)|\vec{F}_1(0)\rangle}{\langle \vec{A}(0)|\vec{A}(0)\rangle} = \begin{pmatrix} 0 & 0 \\ 0 & \langle F(\vec{q},0)\,|\exp(-i\widehat{Q}^L\widehat{L}\widehat{Q}^Lt)|F(\vec{q},0)\rangle\frac{1}{Nm} \end{pmatrix} \\ &= \begin{pmatrix} 0 & 0 \\ 0 & M(\vec{q},t) \end{pmatrix}\end{aligned} \tag{2.24}$$

where

$$M(\vec{q},t) = \frac{\langle F(\vec{q},0)\,|\exp(-i\widehat{Q}^L\widehat{L}\widehat{Q}^Lt)|F(\vec{q},0)\rangle}{Nm}\ . \tag{2.25}$$

Finally the equations of motion read as follows:

$$\begin{aligned} \dot{\rho}\left(\vec{q},t\right)+iqJ\left(\vec{q},t\right)=0 \\ \dot{J}^{L}\left(\vec{q},t\right)+i\left(\tfrac{qk_{B}T}{mS_{q}}\right)J^{L}\left(\vec{q},t\right)+\textstyle\int_{0}^{t}M(\vec{q},t-s)J^{L}\left(\vec{q},s\right)ds=F\left(\vec{q},0\right) \end{aligned} \tag{2.26}$$

With the Laplace transform convention

$$F(z)=\int_{0}^{\infty}\exp(izt)F(t)dt \tag{2.27}$$

applied to the above two equations and eliminating $J^{L}\left(\vec{q},z\right)$; we obtain

$$\rho\left(\vec{q},z\right)=\frac{\rho\left(\vec{q},0\right)}{-iz+\frac{\Omega_{q}^{2}}{-iz+M(\vec{q},z)}} \tag{2.28}$$

where

$$\Omega_{q}^{2}=\frac{q^{2}k_{B}T}{S_{q}m}\ .$$

The normalized autocorrelation function of density fluctuation is defined as:

$$\phi(\vec{q},t)\equiv\frac{\left\langle\delta\rho\left(\vec{q},t\right)|\delta\rho\left(\vec{q},0\right)\right\rangle}{\left\langle\delta\rho\left(\vec{q},t\right)|\delta\rho\left(\vec{q},0\right)\right\rangle}$$

whose Laplace transform is

$$\phi(\vec{q},z)=\left\langle\delta\rho\left(\vec{q},z\right)|\delta\rho\left(\vec{q},0\right)\right\rangle/NS_{q}\ .$$

Inner multiply both sides of Eq.[2.28] with $|\delta\rho\left(\vec{q},0\right)\rangle$:

$$\phi(\vec{q},z)=\frac{1}{-iz+\frac{\Omega_{q}^{2}}{-iz+M(\vec{q},z)}} \tag{2.29}$$

Eq.[2.29] is the Laplace transform of

$$\ddot{\phi}(\vec{q},t)+\Omega_{q}^{2}\phi(\vec{q},t)+\int_{0}^{t}M\left(\vec{q},t-\tau\right)\dot{\phi}(\vec{q},t)d\tau=0 \tag{2.30}$$

where $M\left(\vec{q},t\right)$ is defined in Eq.[2.25]. Eq.[2.30] is the standard Mode Coupling Equation and is the starting point of Mode Coupling theory.

### Mode Coupling Approach

In order to solve the mode coupling equations Eq.[2.30] which is exact, we have to construct an analytic approximation for the random force. Following Kawasaki [66], the standard approach is to project the memory function $M(\vec{q},t)$ in Eq.[2.25] onto the subspace of products of selected variables. In this subsection, we will show $M(\vec{q},t)$ can be expressed as a sum of products of density fluctuation modes, shown in Eqs.[2.39], [2.40] and [2.41], under four simplifications. Again, readers not interested in details can skip the mathematics and go directly to Eqs.[2.39], [2.40] and [2.41].

Since $\widehat{Q}^L\delta\rho\left(\vec{q},0\right)=0$, $F\left(\vec{q},0\right)=m\widehat{Q}^L\widehat{L}J^L\left(\vec{q},0\right)$ has no overlap with $\delta\rho\left(\vec{q},0\right)$. The simplest combination of $\delta\rho\left(\vec{q},0\right)$, which has overlap with $F\left(\vec{q},0\right)$ is pair products:

$$A(\vec{k},\vec{l})=\delta\rho\left(\vec{k},0\right)\delta\rho\left(\vec{l},0\right)\ .$$

So the *first simplification* is to project $F\left(\vec{q},0\right)$ on to the subspace spanned by the pair products, neglecting higher-order contributions:

$$F(\vec{q},0)\simeq\sum_{\vec{k}\vec{l},\vec{k}'\vec{l}'}\overleftrightarrow{g}(\vec{k}\vec{l},\vec{k}'\vec{l}')\left\langle A(\vec{k}',\vec{l}')|F(t)\right\rangle A(\vec{k},\vec{l}) \tag{2.31}$$

where $\overleftrightarrow{g}$ is the normalization matrix:

$$\sum_{\vec{i}\vec{j}}\left\langle A(\vec{k},\vec{l})|A(\vec{i},\vec{j})\right\rangle\overleftrightarrow{g}(\vec{i}\vec{j},\vec{k}'\vec{l}')=\delta_{\vec{k}\vec{k}'}\delta_{\vec{l}\vec{l}'} \tag{2.32}$$

Insert Eq.[2.32] into Eq.[2.25]:

$$M\left(\vec{q},t\right)=\sum_{\vec{k}_1\vec{l}_1,\vec{k}_1'\vec{l}_1'}\sum_{\vec{k}_2\vec{l}_2,\vec{k}_2'\vec{l}_2'}\overleftrightarrow{g}(\vec{k}_1\vec{l}_1,\vec{k}_1'\vec{l}_1')\overleftrightarrow{g}(\vec{k}_2\vec{l}_2,\vec{k}_2\vec{l}_2')\cdot$$
$$\left\langle A(\vec{k}_1',\vec{l}_1)|\vec{F}(\vec{q},0)\right\rangle^*\left\langle A(\vec{k}_2',\vec{l}_2)|\vec{F}(\vec{q},0)\right\rangle\left\langle A(\vec{k}_1,\vec{l}_1)|\exp(-i\widehat{Q}^L\widehat{L}\widehat{Q}^Lt)|A(\vec{k}_2,\vec{l}_2)\right\rangle \tag{2.33}$$

In order to evaluate $\left\langle A(\vec{k}_1,\vec{l}_1)|\exp(-i\widehat{Q}^L\widehat{L}\widehat{Q}^Lt)|A(\vec{k}_2,\vec{l}_2)\right\rangle$, we have to make the *second simplification*: factorizing the averages of products, evolving with generator $\widehat{Q}^L\widehat{L}\widehat{Q}^L$, into products of averages:

$$\left\langle A(\vec{k}_1,\vec{l}_1)|\exp(-i\widehat{Q}^L\widehat{L}\widehat{Q}^Lt)|A(\vec{k}_2,\vec{l}_2)\right\rangle\simeq\left\langle\delta\rho\left(\vec{k}_1,t\right)^*\delta\rho\left(\vec{k}_2,0\right)\right\rangle\left\langle\delta\rho\left(\vec{l}_1,t\right)^*\delta\rho\left(\vec{l}_2,0\right)\right\rangle \tag{2.34}$$

This approximation, factorizing the averages of products into products of averages, is the so-called **mode-mode-coupling factorization** first applied by Kawasaki [66] to explain liquid-vapour critical phenomenon in the 1970s. Thus the left side of Eq.[2.34] can be calculated

$$\left\langle\delta\rho\left(\vec{k}_1,t\right)^*\delta\rho\left(\vec{k}_2,0\right)\right\rangle=\delta_{\vec{k}_1,\vec{k}_2}S_k\phi(\vec{k}_1,t) \tag{2.35}$$

where $S_k$ is defined in Eq.[2.18]. Put Eq.[2.35] into Eq.[2.34] and set $t=0$:

$$\left\langle A(\vec{k},\vec{l})|A(\vec{k}',\vec{l}')\right\rangle=\delta_{\vec{k},\vec{k}'}\delta_{\vec{l}',\vec{l}'}N^2S_kS_p/k_BT\ .$$

Therefore one finds

$$g(\vec{k}\vec{l},\vec{k}'\vec{l}')=k_BT\delta_{\vec{k},\vec{k}'}\delta_{\vec{l},\vec{l}'}/[N^2S_kS_l]\ .$$

Thus we have:

$$M\left(\vec{q},t\right)=(v^2/N)\sum_{\vec{k}\vec{l}}\left|\left\langle F(\vec{q},0)|A(\vec{k}\vec{l})\right\rangle/[NS_kS_l]\right|^2S_kS_l\phi_k(t)\phi_l(t) \tag{2.36}$$

Next we calculate the inner product

$$\begin{aligned} \left\langle F(\vec{q},0)|A(\vec{k}\vec{l})\right\rangle &= m\left\langle (1-\hat{P}^L)\widehat{L}J^L(\vec{q},0))|A(\vec{k}\vec{l})\right\rangle \\ &= \left[\left\langle m\widehat{L}J^L(\vec{q},0)\,|A(\vec{k}\vec{l})\right\rangle - \left\langle m\hat{P}^L\widehat{L}J^L(\vec{q},0)\,|A(\vec{k}\vec{l})\right\rangle\right] . \end{aligned}$$

We calculate these two terms one by one. The first term $\left\langle m\widehat{L}J^L(\vec{q},0)\,|A(\vec{k}\vec{l})\right\rangle$ can be evaluated exactly as :

$$\begin{aligned} &\left\langle m\widehat{L}J^L(\vec{q},0)\,|A(\vec{k}\vec{p})\right\rangle \\ &= -im\left\langle \left\{ J^L(\vec{q},0)^*, \delta\rho\left(\vec{k},0\right)\delta\rho\left(\vec{l},0\right)\right\}\right\rangle \\ &= -im\left[\left\langle \left\{ J^L(\vec{q},0)^*, \delta\rho\left(\vec{k},0\right)\right\}\delta\rho\left(\vec{l},0\right)\right\rangle + \vec{k}\longleftrightarrow\vec{l}\right] \\ &= \vec{k}\left\langle \delta\rho\left(\vec{q}-\vec{k},0\right)^*\delta\rho\left(\vec{l},0\right)\right\rangle + \vec{k}\longleftrightarrow\vec{l} \\ &= \delta_{\vec{q},\vec{k}+\vec{l}}N\left[\vec{k}S_k + \vec{p}S_p\right] \\ &= \delta_{\vec{q},\vec{k}+\vec{l}}NS_kS_p\left[\vec{q} - nc_k\vec{k} - nc_l\vec{l}\right] \end{aligned} \tag{2.37}$$

In the first step, we have used the Yvon Theorem: $\left\langle A|\hat{L}B\right\rangle = -i\left\langle\{A^*, B\}\right\rangle$, where $\{\cdots\}$ is the Poisson bracket. The last step follows from the Ornstein-Zernike Equation $S_k = \frac{1}{1-nC_K}$.

Since $\widehat{L}J^L(\vec{q},0)$ has different time reversal symmetry than $J^L(\vec{q},0)$, the second term:

$$\begin{aligned} &\left\langle m\hat{P}^L\widehat{L}J^L(\vec{q},0)\,|A(\vec{k}\vec{l})\right\rangle \\ &= m\left\langle \tfrac{k_BT}{NS_q}|\delta\rho(\vec{q},0)\rangle\langle\delta\rho(\vec{q},0)\,|\widehat{L}J^L(\vec{q},0)\,|A(\vec{k}\vec{l})\right\rangle \\ &= m\tfrac{k_BT}{NS_q}\left\langle \delta\rho(\vec{q},0)\,|\widehat{L}J^L(\vec{q},0)\right\rangle\left\langle \delta\rho(\vec{q},0)\,\delta\rho\left(\vec{k},0\right)\delta\rho\left(\vec{l},0\right)\right\rangle \\ &= N\delta_{\vec{q},\vec{k}+\vec{l}}S_kS_lS_q + C(\vec{q},\vec{k},\vec{l}) \end{aligned} \tag{2.38}$$

where $C(\vec{q},\vec{k},\vec{l})$ is a triple correlation, which is irreducible and will be neglected. This is the *third simplification.* Finally, there are, of course, other contributions, such as from intramolecular degrees of freedom, to the kernel. As the *fourth simplification* they are replaced by a white noise term $\nu$. After all these steps, we obtain the following expression for the memory function:

$$M\left(\vec{q},t\right) = \nu\delta(t) + \Omega_q^2 m(\vec{q},t) \tag{2.39}$$

$$m(\vec{q},t) = (1/2V) \sum_{\vec{q}=\vec{k}+\vec{l}} V\left(\vec{q},\vec{k},\vec{l}\right) \phi_{\vec{k}}(t)\phi_{\vec{l}}(t) \tag{2.40}$$

$$V\left(\vec{q},\vec{k},\vec{l}\right) = nS_qS_kS_l\left\{\vec{q}\cdot\left[\vec{k}C_k + \vec{l}C_l\right]/q\right\}^2/q^2 \tag{2.41}$$

$m(\vec{q},t)$ in Eq.[2.40] is usually called the mode coupling functional and consists of a sum of products of density fluctuation modes $\phi_{\vec{k}}(t)\phi_{\vec{l}}(t)$ with the coupling vertices $V\left(\vec{q},\vec{k},\vec{l}\right)$ determined by the structure factors $S_k$, $S_l$ and $S_q$.

Equations [2.30], [2.39], [2.40] and [2.41] constitute the simplified (or idealized) version of MCT, given as a closed set of equations. If the intermolecular potential is known, the structure factors can be computed with well-established approximation methods (e.g. the Percus–Yevick equation) and used to evaluate the vertices $V\left(\vec{q},\vec{k},\vec{l}\right)$. The equations are then solved self-consistently for a discrete set of wave vectors (typically 100 to 400). A numerical solution of the full MCT equations was first carried out for a system of particles interacting via a Lennard-Jones potential by Bengtzelius [67] and has also been performed for the hard-sphere system [68], [69]. Most recently, it has been used for the Baxter model of sticky hard spheres by Fabbian et al [70]. This analysis predicted a surprising reentrant glass transition which was subsequently observed in experiments [71], [72]. Fig.[2-7] shows the numerical solution of MCT equations for the hard-sphere system [1] with structure factors calculated via the Percus–Yevick equation for two $q$-values. The different curves represent different packing fractions labelled with the index $n$, where $\phi = \phi_c(1 \pm 10^{-n/3})$. The

---

[1]. The hard-sphere model mimics non-themal system like a colloid or emulsion glass. In such systems, the constituent particles interact with each other only when they touch. Also the constituent particles are so large and heavy that thermal exicitation plays a minor role. Thus the control parameter in these system is the volume fraction, instead of temperature in normal thermal systems, and the complete structural arrest, predicted by MCT, can be observed experimentally.

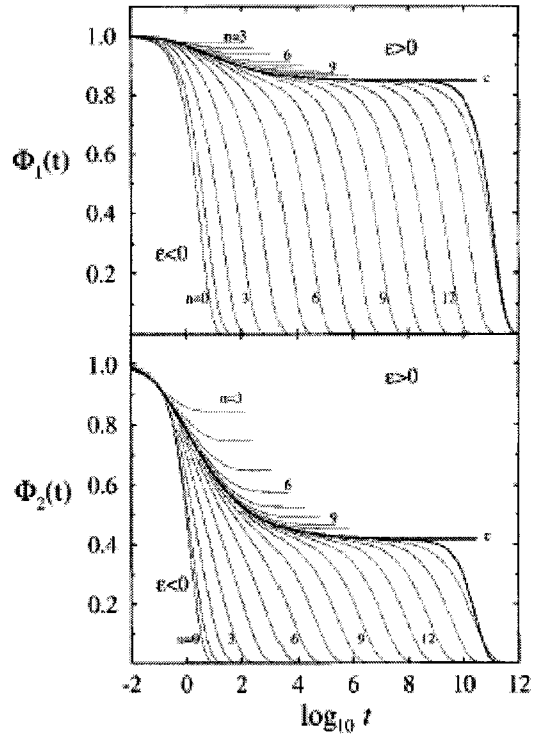

Figure 2-7: Solutions to the MCT equations for a hard-sphere system at two wavevectors $q_1 = 7.0$ and and $q_2 = 10.6$. The dark curves labelled $c$ are at the critical packing fraction $c$. The other curves are labelled with an index $n$ where $\phi = \phi_c(1+e)$ and $e = \pm 10^{-n/3}$ . From [68]

result for the critical packing fraction $\phi_c$ is indicated by the dark curve labelled c and $\phi_c = 0.518$ is close to experimental results 0.55. Note that for$\phi > \phi_c$, the correlators do not decay to zero, showing that the structure has been arrested.

Thus simplified MCT predicts a complete structural arrest under critical condition, like critical volume fraction $\phi_c$ in colloid system and critical temperature $T_c$ in thermal molecular or polymeric system, which is usually called the MCT critical temperature $T_c$. However, this complete structural arrest usually can't be observed in thermal systems and the correlation function $\phi_q(t)$ always decays to zero after a sufficiently long time, in contradiction with the simplified MCT's prediction. The reason for that is the simplified MCT contains only nonlinear interaction among the density fluctuation modes and the possibility of activated processes has been left out. Following a suggestion by Das and Mazenko [73], Gotze and Sjogen [74] added the leading correction terms, a temperature-dependent hopping parameter to represent the activated transport processes, to the memory function and developed the extended MCT.

The breakdown of the Simplified MCT below $T_c$ has recently been confirmed by computer simulation analysis of the saddles in PEL [39],[40],[41], which shows the system starts to be trapped in the local minima at $T_c$.

### The two-step relaxation scenario

One of the important successes of the simplified MCT is the prediction of a two-step relaxation scenario, which has been mentioned briefly in Sec.[**2.2.2**]. As shown in Fig.[2-7], we can see that at low volume fraction (or high temperature), $\phi(t)$ decays to zero within a time window of about one decade, which is essentially a microscopic transient. As volume fraction increases (or temperature decreases in thermal system), the microscopic transient is followed by decay towards a 'plateau', which is followed by a second decay ending in the familiar $\alpha$-relaxation process. As volume fraction increases further, the plateau extends to longer times as illustrated in Fig.[2-7], e.g., for $n = 12$. This splitting off of the structural relaxation from the initial microscopic transient produces the two-step relaxation scenario in the region between the microscopic dynamics and the $\alpha$-decay, which has been observed in many experiments and computer simulations. In MCT, the transition region centered at the plateau is designated as the $\beta$-relaxation region.

The development of the intermediate two-step decay as low volume fraction increases (or $T$ decreases) reflects the growing strength of the 'cage effect', i.e. temporary localization of a particle in the transient cage formed by its neighbors. One can roughly view the sequence of dynamic regimes of the relaxation process as an

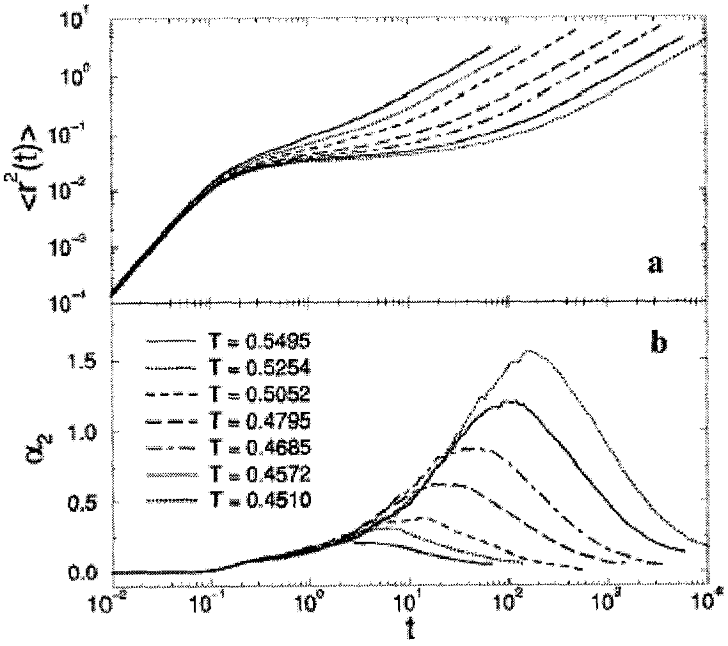

Figure 2-8: (a) Mean square displacement $\langle r^2(t)\rangle$ of species A particles in a binary L-J simulation. $\langle r^2(t)\rangle$ is plotted as function of time for several temperatures. (b) Non-Gaussian parameter $\alpha_2(t)$ as function of time for the same values of temperatures as in (a). ( From [75] )

initial microscopic motion of each particle within its transient cage followed, in the plateau region, by collective motion of the cage. The beginning of the decay away from the plateau, called the von Schweidler decay, corresponds to the initial break-up of the cages which is followed, finally, by the long-time $\alpha$-relaxation. Besides correlation functions, the study of mean square displacement $\langle r^2(t)\rangle$ also indicates the same "cage" picture. In Fig.[2-8] (a), $\langle r^2(t)\rangle$ of one species in a L-J binary mixture simulation is shown [75]. At the earliest time, particle motion is ballistic ($\langle r^2(t)\rangle \propto t^2$), as they have not moved far enough to encounter the cage formed by their neighbors. As the displacement increases, their motion is impeded by the cage, leading to a plateau in the plot. This plateau becomes more long-lived with decreasing temperature, presumably because cage rearrangements involve cooperative rearrangements of a larger number of particles and relaxation time increases as the glass transition is approached. Finally the cage is broken and cage rearrangement leads to an upturn at the end of plateau. The motion becomes diffusive with $\langle r^2(t)\rangle \propto t$. A non-Gaussian parameter $\alpha_2(t)$, which describes the degree of deviation of the displacement distribution at time $t$ from a Gaussian distribution, is shown in Fig.[2-8] (b). $\alpha_2(t)$ is essentially zero in the short and long time limits, which means the displacement distribution in these time windows is Gaussian, and non-zero in the "plateau" region, which indicates the distribution there is non-Gaussian and there are broad tails. In the PEL description, $\beta$ relaxation occurs when the system hops between adjacent minima, and $\alpha$ relaxation means hopping between two separated minima, as shown in Fig.[2-9].

The plateau level in $\phi(t)$ for $\phi > \phi_c$(or $T < T_c$) is $f_q^c(T)$, which shows a square root cusp behavior as a function of temperature separation. As $T$ approaches $T_c$, $f_q^c(T)$remains close to $f_q^c = f_q^c(T_c)$. In the region close to $T_c$, namely $(T - T_c)/T_c \ll 1$, the MCT equations can be expanded in the small parameter $\phi(\vec{q}, t) - f_q^c$.

First, one finds that

$$\phi(\vec{q}, t) - f_q^c = h_q G(t) \tag{2.42}$$

This factorization result predicts that the $\vec{q}$-dependence of $\phi_{\vec{q}}(t) - f_q^c$ in this asymptotic

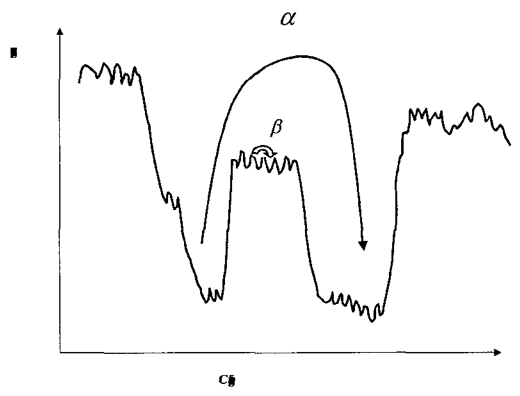

Figure 2-9: Two-step relaxation in PEL description, where $\beta$ relaxation corresponds the system hoping between two adjacent minima and $\alpha$ relaxation means hoping between two separated minima.

region is completely specified by $h_q$, while the time dependence of all correlators is given by the same $q$-independent function $G(t)$, which is called the $\beta$-correlator. $G(t)$ is the solution to the equation

$$\lambda G^2(t) + \sigma = \frac{d}{dt}\int_0^t G(t-t')G(t')dt' \tag{2.43}$$

Solving Eq.[2.43] for $\sigma < 0$, where $\sigma = T - T_c$ is the temperature separation, one finds that $G(t)$ first decays to zero as $t^{-a}$(the critical decay), and then decreases as $-t^b$(von Schweidler decay). The two exponents $a$ and $b$ are related to each other via an exponent parameter $\lambda$ $(1/2 < \lambda < 1)$ by

$$\lambda = \Gamma^2(1/a)/\Gamma(1-2a) = \Gamma^2(1+b)/\Gamma(1+2b) \tag{2.44}$$

where $\Gamma(x)$ is gamma function. Eq.[2.43] is the leading-order asymptotic result usually employed in comparing experimental data with MCT. The exponent parameter $\lambda$ is the only material-dependent quantity, and is usually treated as an adjustable fitting parameter. For the hard-sphere system, $\lambda$ was calculated with the Percus–Yevick approximation to be $\lambda = 0.74$.

In the frequency representation, the above two-step relaxation scenario will have the following structure. The susceptibility spectra in hard sphere system, which are obtained by dividing the intensity spectrum by the boson factor, see Eq.[4.7], are shown in Fig.[2-10]. The $\alpha$-peak, corresponding to the $\alpha$-decay in the time domain, exists in low frequency region and moves to lower frequency as the system approaches $T_c$. In the high frequency region, there are microscopic peaks. Between the $\alpha$-peak and the microscopic peaks, there are minima, which corresponds to the $\beta$ region and can be described by two-power law scaling to leading-order approximation:

$$\chi''(\omega) = \chi''_{\min}\left[b\left(\frac{\omega}{\omega_{\min}}\right)^{a} + a\left(\frac{\omega}{\omega_{\min}}\right)^{-b}\right]\frac{1}{a+b}\,.$$

The two-power law scaling has been tested by numerous experiments and simulations [76], [77], [78], [79].

### Hybrid model

Several recent publications [80],[81], have utilized a convenient semi-empirical function to model the two-step relaxation scenario predicted by the Simplified MCT in supercooled liquids. The hybrid function consists of the Cole-Davidson function, Eq.[2.4], representing the $\alpha$ relaxation, plus a power-law term $\omega^a$, which represents the fast relaxation processes related to the $t^{-a}$ critical decay of MCT.

$$H(\omega) = H_{CD}(\omega) + H_{crit}(\omega)$$

In order to avoid having the $t^{-a}$ term contribute in the $\alpha$ peak region, a cutoff term $e^{-t/\tau_{CD}}$ can be included : $H_{crit}(t) = Bt^{-a}e^{-t/\tau_{CD}}$. The resulting hybrid model memory

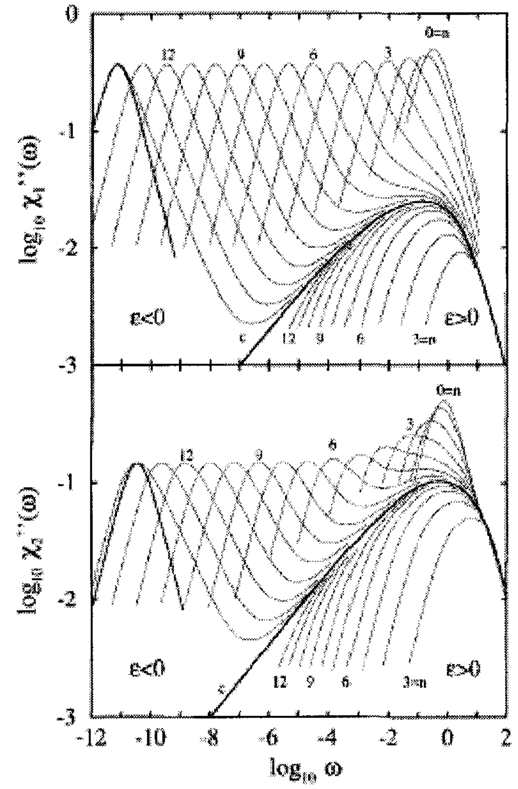

Figure 2-10: Susceptibility spectra for the correlation functions shown in Fig.[2-7]. [68]

function is then given by

$$H(\omega) = \left\{\left[(1 - (1 + i\omega\tau)^{-\beta}\right] + i\omega p(\tau^{-1} + i\omega)^{a-1}\right\} \tag{2.45}$$

where the Laplace transform convention of Eq.[3.36] has been used. Both real and imaginary parts of one hybrid function generated numerically are plotted in Fig.[2-11], using the parameters obtained from the hybrid fit to the Salol backscattering susceptibility spectrum at 295 $K$. The imaginary part mimics the MCT susceptibility spectra in Fig.[2-10].

The asymptotic behavior of the hybrid function can be evaluated. For the low frequency limit, where $\omega\tau \ll 1$, the critical part doesn't contribute due to the cut-off. Thus we have

$$H(\omega) \xrightarrow[\omega\tau\ll 1]{} i\omega\tau\beta \ . \tag{2.46}$$

For the high frequency limit ($\omega\tau \gg 1$), we have :

$$H(\omega)\xrightarrow[\omega\tau\gg 1]{} \left\{1 + p\omega^{a} \sin\left[\frac{\pi}{2}(1-a)\right]\right\} + i\left\{(\omega\tau)^{-\beta} \sin\left(\frac{\pi\beta}{2}\right) + p\omega^{a} \cos\left[\frac{\pi}{2}(1-a)\right]\right\} \tag{2.47}$$

Eq.[2.47] diverges at very high frequencies. However, that is not important for us because it *doesn't* diverge in the frequency range of the experiment (0-1000 GHZ), as shown in Fig.[2-11]. In high frequencies in our windows, we can see that the real part of $H(\omega)$ is basically constant, which indicates $p\omega^{a} \sin\left[\frac{\pi}{2}(1-a)\right] \ll 1$. Yet the critical contribution to the imaginary part is comparable to the tail of CD part, $(\omega\tau)^{-\beta} \sin\left(\frac{\pi\beta}{2}\right) \sim p\omega^{a} \cos\left[\frac{\pi}{2}(1-a)\right]$, which produce a minima around 100 $GHZ$.

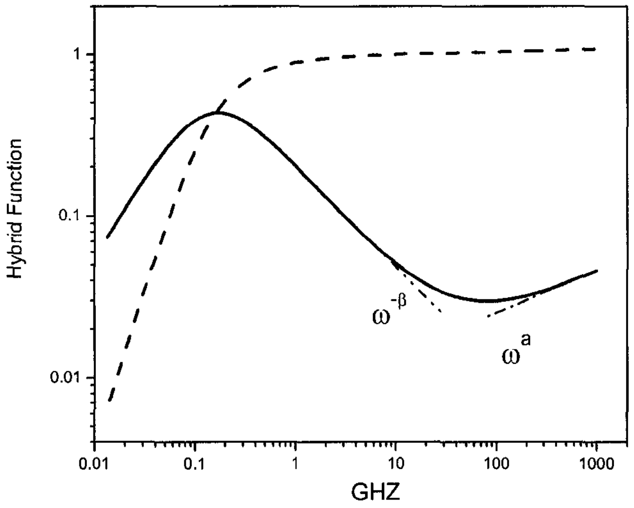

Figure 2-11: Real (dotted line) and imaginary (solid line) part of hybrid function, generated numerically with $\tau = 1.23$, $\beta = 0.74$, $p = 0.0062$ and $a = 0.3$ in Eq.[ 2.45]

# Chapter 3

# Theory of Low-Frequency Inelastic Light-scattering in Liquids

When lights impinges on matter, the electric field of the light induces an oscillating polarization in the molecules. The molecules then serve as secondary sources of light and subsequently radiate (scatter) light. The experimentally measurable light-scattering characteristics, such as frequency shifts, the angular distribution, the polarization and the intensity of the scattered light, are determined by the molecular properties and dynamics in the scattering medium. Therefore, with the help of electrodynamics and the theory of statistical mechanics, useful information about the molecular properties and dynamics can be extracted from experimental data.

More than one century ago, Rayleigh [82] developed a theory of light-scattering from gases of molecules, in which each molecule is treated as an independent scattering object. But it was soon found that the intensity of light-scattering by condensed phases was less than the prediction of his theory by more than an order of magnitude. This effect was correctly attributed to the destructive interference between the wavelets scattering from different molecules. But the means of how to calculate the extent of this interference was not known until Smoluchowski [83] and Einstein [84] elegantly circumvented this difficulty by considering the liquid to be a continuous medium in which thermal fluctuations give rise to local density fluctuation and thereby to dielectric fluctuations. This theory is called the fluctuation theory of light-scattering. According to this theory, the intensity of the scattered light can be calculated from the mean-square fluctuations in density which in turn can be determined from thermodynamic properties such as the isothermal compressibility via the equipartition theorem of statistical mechanics.

Most of the early studies mainly focused on the integrated intensity of the scattered light. Inspired by the idea of Smoluchowski and Einstein, Leon Brillouin [85] predicted a doublet in the frequency distribution of the scattered light, considering the thermal density fluctuations as sound waves. This doublet is now known as the Brillouin Doublet. In the early 1930s Gross [86] conducted a series of high-resolution light-scattering experiments on liquids and first observed the predicted Brillouin doublet. He also noticed the presence of another unshifted central component, which is now called Rayleigh line. The spectrum that Gross observed, consisting of a central Rayleigh line and a symmetrically shifted Brillouin Doublet, is usually called the Rayleigh-Brillouin spectrum. Landau and Placzek [87] suggested a theoretical explanation of the Rayleigh-Brillouin spectrum, based on hydrodynamics, and attributed the Rayleigh line to nonpropagating temperature fluctuations. The full analysis was later written down by Mountain [88].

Beyond the original hydrodynamics approach, which mainly deals with a simple liquid of spherical molecules, two more elements have been added to the theory of light-scattering from liquids since the 1950s. One is viscoelasticity, introduced by the Mountain [88], which leads to a new central line called the Mountain mode. Another is molecular anisotropy, which is responsible for the broad rotational background in both VV and VH spectra and also the well-known "Rytov dip". In a glassforming liquid of anisotropic molecules, both viscoelasticity and molecular anisotropy exist. Several theories [9], [10] [13] have been developed to incorporate these two elements into the interpretation of VV and VH spectra. But there was no complete theory, taking into account both viscoelasticity and molecular anisotropy consistently and completely, until recently. Pick, Franosch, Dreyfus, and Latz have undertaken a new unified analysis of light-scattering spectra using both a phenomenological analysis [18], [23], and a microscopic Zwanzig-Mori approach [24] for glassforming liquids of anisotropic molecules.

In this Chapter, we will review the theory of light-scattering. Some basic facts about light-scattering are discussed in Sec.[**3.1**]. Then the usual Rayleigh-Brillouin spectrum in simple liquids of spherical molecules will be derived by the hydrodynamic approach in Sec.[**3.2**]. The focus of this chapter is Sec.[**3.3**], where the light-scattering from a system of anisotropic molecules is discussed. We first consider the situation, where the rotational and translational motions are independent with other. Then Pick-Franosch theory, which includes rotation-translation coupling, is discussed in detail.

## 3.1 Basics of light-scattering

The light-scattering experimental arrangement is shown schematically in Fig.[3-1]. The incident light, which is assumed to be monochromatic,

$$\vec{E}_i(\vec{r},t) = \vec{n}_i E_0 \exp\left[i\left(\vec{k}_i \cdot \vec{r} - \omega_i t\right)\right]$$

with wave vector $\vec{k}_i$, polarization $\vec{n}_i$ and frequency $\omega_i$, is scattered by the scattering object. The scattering object is a nonmagnetic, nonconducting, nonabsorbing medium with average dielectric constant $\varepsilon_0$. Thus the dielectric tensor at space-time point $(\vec{r},t)$ can be written as

$$\overleftrightarrow{\varepsilon}(\vec{r},t) = \varepsilon_0 \overleftrightarrow{I} + \delta\overleftrightarrow{\varepsilon}(\vec{r},t)$$

where $\delta\overleftrightarrow{\varepsilon}(\vec{r},t)$ is the dielectric fluctuation tensor. The detector collects the scattered light along the direction of $\vec{k}_f$ with polarization $\vec{n}_f$. The scattering angle between $\vec{k}_i$

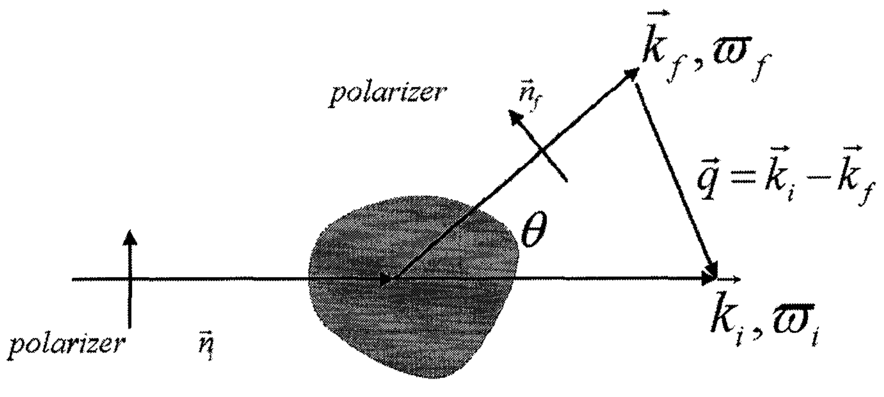

Figure 3-1: Light of polarization $\vec{n}_i$ and wave vector $\vec{k}_i$ is scattered in all direction. Only scattered light with polarization $\vec{n}_f$ and wave vector $\vec{k}_f$ is collected. The scattered wavevector $\vec{q} = \vec{k}_i - \vec{k}_f$ is defined by the geometry. The angle between $\vec{k}_i$ and $\vec{k}_f$ is $\theta$.

and $\vec{k}_f$ is $\theta$. The scattering vector is $\vec{q} = \vec{k}_i - \vec{k}_f$. The scattered light reaching the detector, which is $R$ away from the scattering center, has the spectral distribution $I_{if}(\vec{q}, \omega_f, R)$. Electrodynamics [1] gives the spectral distribution of the scattered light as:

$$I_{if}(\vec{q}, \omega_f, R) = \left[ \frac{|E_0|^2 k_f^4}{16\pi^2 R^2 \varepsilon_0^2} \right] \frac{1}{2\pi} \mathrm{Re} \int_{-\infty}^{\infty} dt \left\langle \delta\varepsilon_{if}(\vec{q}, 0)\, \delta\varepsilon_{if}(\vec{q}, t) \right\rangle \exp\left(i\left(\omega_f - \omega_i\right) t\right) \tag{3.1}$$

where $\delta\varepsilon_{if}(\vec{q}, t)$ is the $\vec{q}$ component of the spatial Fourier transform of $\delta\varepsilon_{if}(\vec{r}, t)$

$$\begin{aligned} \delta\varepsilon_{if}(\vec{r}, t) &= \vec{n}_i \cdot \delta\overleftrightarrow{\varepsilon}(\vec{r}, t) \cdot \vec{n}_f \\ \delta\varepsilon_{if}(\vec{q}, t) &= \int_v d\vec{r} \exp(i\vec{q} \cdot \vec{r})\, \delta\varepsilon_{if}(\vec{r}, t) \end{aligned} \tag{3.2}$$

Eq.[3.1] tells us that, apart form the prefactor $k_f^4$, the frequency distribution of $I_{if}$ depends only on the difference between $\omega_f$ and $\omega_i$ :

$$\omega = \omega_f - \omega_i \ .$$

The spectrum of the scattered light, with frequency shift measured respective to $\omega_i$, is :

$$I_{if}(\vec{q},\omega,R) = A\frac{1}{2\pi}\,\mathrm{Re}\left\{\int_{-\infty}^{\infty} dt\,\langle\delta\varepsilon_{if}(\vec{q},0)\,\delta\varepsilon_{if}(\vec{q},t)\rangle\exp(i\omega t)\right\} \tag{3.3}$$

where

$$A = \left[\frac{|E_0|^2\,k_f^4}{16\pi^2R^2\varepsilon_0^2}\right].$$

Since the range of frequencies of interest is very small compared to $\omega_i$, $A$ is effectively constant.

The expressions above are written in general tensor notation and are independent of any specific laboratory coordinate system. However, it is convenient for many applications to use a specific scattering geometry. The one commonly used is shown in Fig.[3-2] [1]. The plane defined by $\vec{k}_i$ and $\vec{k}_f$ is called the scattering plane. In Fig.[3-2], the $XZ$ plane is the scattering plane, the angle, $\theta$, between $\vec{k}_i$ and $\vec{k}_f$ is the scattering angle and the scattering vector $\vec{q} = \vec{k}_i - \vec{k}_f$ is along the $Z$ axis.

The subscriptions $V$ and $H$ are commonly used to indicate the polarization settings in a light-scattering experiment. $V$ and $H$ correspond to the directions which are perpendicular (vertical) and parallel (horizontal) to the scattering plane. $I_{VV}$ is usually called the polarized component and $I_{VH}$ is called the depolarized component, where the first subscript is for the incident polarization and the second is for the collected polarization. Using the geometry in Fig.[3-2], we can write down the components of the dielectric tensor involved in $I_{VV}$ and $I_{VH}$ according to Eq.[3.2]

$$\delta\varepsilon_{VV}(\vec{r},t) = \delta\varepsilon_{yy}(\vec{r},t) \tag{3.4}$$

$$\delta\varepsilon_{VH}(\vec{r},t) = \delta\varepsilon_{yx}(\vec{r},t)\sin(\theta/2) - \delta\varepsilon_{yz}(\vec{r},t)\cos(\theta/2) \tag{3.5}$$

where $\delta\varepsilon_{yy}(\vec{r},t)$, $\delta\varepsilon_{yx}(\vec{r},t)$ and $\delta\varepsilon_{yz}(\vec{r},t)$ are in the laboratory frame in Fig.[3-2].

In this thesis, we assume the molecules are rigid, both mechanically and dieletrically, which means that distortions in the inertia and dielectric tensors due to collisions

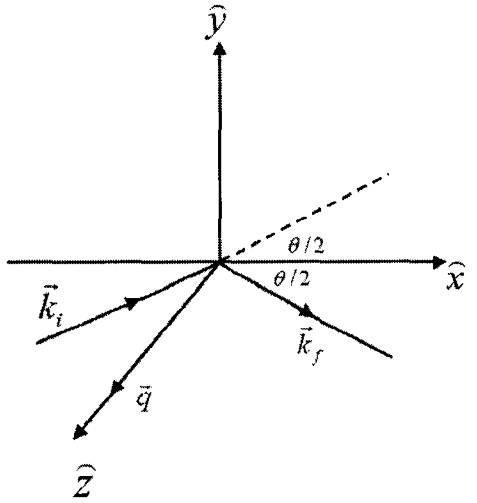

Figure 3-2: Scattering geometry used in this thesis, where the $XZ$ plane is the scattering plane, the angle$\left(\vec{k}_i, \vec{k}_f\right)$ is the scattering angle and the scattering vector $\vec{q} = \vec{k}_i - \vec{k}_f$ is parallel to the $Z$ axis. (following [1])

between molecules are negligible. If, in the liquid, there are $N$ identical molecules at positions: $\vec{r}_1(t), \vec{r}_2(t) \ldots \vec{r}_N(t)$, the $jth$ molecule has the polarizability tensor $\overleftrightarrow{\mu}_j(t)$ in the laboratory fixed frame and depends on its orientation at time $t$, the local dielectric tensor can be written as:

$$\overleftrightarrow{\varepsilon}(\vec{r}, t) = \sum_{j=1}^{N} \overleftrightarrow{\mu}_j(t)\, \delta\left(\vec{r} - \vec{r}_j(t)\right)$$

For a liquid of spherical molecules, whose molecular dielectric property is isotropic and the polarizability tensor $\overleftrightarrow{\mu}_j(t)$ reduces to a scalar $\mu$, the local dielectric tensor is proportional to the local density : $\overleftrightarrow{\varepsilon}(\vec{r}, t) = \mu\rho(\vec{r}, t)\overleftrightarrow{I}$, where $\mu$ is the polarizability of single molecule and $\rho(\vec{r}, t)$ is the number density. In this case, only the polarized light-scattering spectrum $I_{vv}(\vec{q}, \omega, R)$ exists and is proportional to the spectral density of density fluctuation:

$$I_{VV}(\vec{q},\omega) = A\mu^2 \frac{1}{2\pi} \operatorname{Re}\left\{ \int_{-\infty}^{\infty} dt \left\langle \delta\rho\left(\vec{q},0\right) \delta\rho\left(\vec{q},t\right)\right\rangle \exp\left(i\omega t\right) \right\} \tag{3.6}$$

which gives the usual Rayleigh-Brillouin spectrum as discussed in next section. (There will be a weak depolarized spectrum due to higher-order scattering processes, but we will not consider that here.) In the case of liquids of anisotropic molecules, the situation will be more complicated as discussed in detail below.

## 3.2 Brillouin Scattering in Simple Liquids of Spherical Molecules

After introducing the basics of light-scattering, we discuss how the Rayleigh-Brillouin spectrum can be derived from hydrodynamics in a simple liquid with spherical molecules following the analysis of Mountain [88]. Since the wavelength $\lambda$ of visible light, which is commonly used in the light-scattering experiment, is much larger than a typical intermolecular separation $d$ in condensed phases $\left(\lambda \sim 5 \times 10^3\text{Å},\ \lambda \sim 10\text{Å}\right)$. Also we are working in a relatively low frequency domain (*below* $10^3 GHZ$). Thus we can model the scatterer as a continuous medium, which can be divided into volume elements characterized locally. These volume elements are macroscopically small compared to the wavelength and microscopically large enough to contain many molecules. Each volume is equilibrated and thermodynamic relations can be applied locally.

Now let's first consider the simplest liquid: a monatomic liquid of spherical molecules. This system can be described by conventional hydrodynamics arising from conservation equations. The mass, momentum and energy conservation equations can be written as [1], [62], [89], [90], :

$$\frac{\partial\rho\left(\vec{r},t\right)}{\partial t} + \nabla\cdot\left[\rho\left(\vec{r},t\right)\vec{u}\left(\vec{r},t\right)\right] = 0 \tag{3.7}$$

$$\frac{\partial\left[m\rho\left(\vec{r},t\right)\vec{u}\left(\vec{r},t\right)\right]}{\partial t}+\nabla\cdot\left[m\rho\left(\vec{r},t\right)\vec{u}\left(\vec{r},t\right)\vec{u}\left(\vec{r},t\right)-\overleftrightarrow{\sigma}\left(\vec{r},t\right)\right]=0 \tag{3.8}$$

$$\frac{\partial e\left(\vec{r},t\right)}{\partial t}+\nabla\cdot\left[\vec{H}\left(\vec{r},t\right)+e\left(\vec{r},t\right)\vec{u}\left(\vec{r},t\right)-\vec{u}\left(\vec{r},t\right)\cdot\overleftrightarrow{\sigma}\left(\vec{r},t\right)\right]=0 \tag{3.9}$$

Eq.[3.7] is the mass conservation equation, where $\rho\left(\vec{r},t\right)$ and $\vec{u}\left(\vec{r},t\right)$ are the local particle density and velocity. Eq.[3.8] is the momentum conservation equation, where $m$ is the mass of one molecule and $\overleftrightarrow{\sigma}\left(\vec{r},t\right)$ is the stress tensor. Eq.[3.9] is the energy conservation equation, where $e\left(\vec{r},t\right)$ is the energy density, and $\vec{H}\left(\vec{r},t\right)$ is the heat flux.

In order to close the equations, we have to introduce the constitutive equation relating the stress tensor $\overleftrightarrow{\sigma}\left(\vec{r},t\right)$ to velocities $\vec{u}\left(\vec{r},t\right)$ :

$$\overleftrightarrow{\sigma}\left(\vec{r},t\right)=\left(-p\left(\vec{r},t\right)+\eta_b\nabla\cdot\vec{u}\left(\vec{r},t\right)\right)\overleftrightarrow{I}+\eta_s\overleftrightarrow{\tau} \tag{3.10}$$

where $\eta_s$ and $\eta_b$ are the shear and bulk viscosities, $p$ is the pressure, and $\overleftrightarrow{\tau}$ is the traceless strain rate tensor:

$$\tau_{ij}=\frac{\partial u_i}{\partial x_j}+\frac{\partial u_j}{\partial x_i}-\frac{2}{3}(\nabla\cdot\vec{u})\delta_{ij} \tag{3.11}$$

The heat flux $\vec{H}$ is related to the temperature gradient $\nabla T\left(\vec{r},t\right)$ by Fourier's law:

$$\vec{H}=-\lambda\nabla T\left(\vec{r},t\right)\ . \tag{3.12}$$

From Eq.[3.6], we know the spectrum of density fluctuation is our ultimate interest in this case, which can be solved from Eqs.[3.7] to [3.12]. We linearize Eq.[3.7], Eq.[3.8] and Eq.[3.9] up to the first order of fluctuations, with Eq.[3.10], Eq.[3.11] and Eq.[3.12] plugged in, and end up with the following equations if we assume there is no macroscopic flow, namely $\langle\vec{u}\left(\vec{r},t\right)\rangle=0$:

$$\frac{\partial\delta\rho\left(\vec{r},t\right)}{\partial t}+\rho_0\nabla\cdot\left[\vec{u}\left(\vec{r},t\right)\right]=0 \tag{3.13}$$

$$m\rho_0 \frac{\partial\left[\vec{u}\left(\vec{r},t\right)\right]}{\partial t} = -\nabla\delta p\left(\vec{r},t\right) + \eta_s \nabla^2 \vec{u}\left(\vec{r},t\right) + \left(\eta_b + \frac{1}{3}\eta_s\right)\nabla\left(\nabla\cdot\vec{u}\left(\vec{r},t\right)\right) \tag{3.14}$$

$$\frac{\partial\delta e\left(\vec{r},t\right)}{\partial t} + \left(e_0 + p_0\right)\nabla\cdot\vec{u}\left(\vec{r},t\right) = \lambda\nabla^2\delta T\left(\vec{r},t\right) \tag{3.15}$$

where $\rho_0$, $e_0$, $p_0$ are the averaged density, energy density and pressure; $\delta\rho\left(\vec{r},t\right)$, $\delta e\left(\vec{r},t\right)$, $\delta T\left(\vec{r},t\right)$ are the fluctuations of density, energy density and temperature. Eliminating $\nabla\cdot\left[\vec{u}\left(\vec{r},t\right)\right]$ in Eq.[3.15] by Eq.[3.13], we get:

$$\frac{\partial h\left(\vec{r},t\right)}{\partial t} = \lambda\nabla^2\delta T\left(\vec{r},t\right)$$

where $h\left(\vec{r},t\right) = \delta e\left(\vec{r},t\right) - \frac{\left(e_0+p_0\right)}{\rho_0}\delta\rho\left(\vec{r},t\right)$ is essentially the fluctuation in heat density. It can be written in terms of entropy density: $h\left(\vec{r},t\right) = T_0\delta S\left(\vec{r},t\right)$, where $\delta S\left(\vec{r},t\right)$ is the fluctuation of entropy density. Thus the energy conservation equation can be rewritten as:

$$T_0\frac{\partial\delta S\left(\vec{r},t\right)}{\partial t} = \lambda\nabla^2\delta T\left(\vec{r},t\right) \tag{3.16}$$

Introducing two thermodynamic relations locally:

$$\begin{aligned}\delta S\left(\vec{r},t\right) &= \left(\tfrac{\partial S}{\partial\rho}\right)_T\delta\rho\left(\vec{r},t\right) + \left(\tfrac{\partial S}{\partial T}\right)_\rho\delta T\left(\vec{r},t\right)\\ \delta p\left(\vec{r},t\right) &= \left(\tfrac{\partial p}{\partial\rho}\right)_T\delta\rho\left(\vec{r},t\right) + \left(\tfrac{\partial p}{\partial T}\right)_\rho\delta T\left(\vec{r},t\right)\end{aligned}$$

, where the partial differentials like $\left(\frac{\partial S}{\partial\rho}\right)_T$ can be expressed in terms of measurable thermodynamics quantity [1], we can eliminate $\delta S\left(\vec{r},t\right)$ and $\delta p\left(\vec{r},t\right)$ from Eq.[3.13], Eq.[3.14] and Eq.[3.16]. Then this set of equations can be closed and solved with Fourier-Laplace transform with appropriate initial condition [1], [62]. The final spectral expression, correct to the order $q^2$ [1], [62], can be written as:

$$\begin{aligned}S\left(\vec{q},\omega\right) = \tfrac{\left\langle\delta\rho(\vec{q},\omega)\delta\rho(\vec{q},0)\right\rangle}{\left\langle\delta\rho(\vec{q},0)\delta\rho(\vec{q},0)\right\rangle} = \tfrac{1}{\pi}V\rho_0^2k_BT\chi_T\Big\{\left(1-\tfrac{1}{\gamma}\right)\left[\tfrac{D_Tq^2}{\omega^2+\left[D_Tq^2\right]^2}\right]\\ +\tfrac{1}{\gamma}\left(\tfrac{\Gamma q^2}{\left(\omega-C_0q\right)^2+\left[\Gamma q^2\right]^2}+\tfrac{\Gamma q^2}{\left(\omega+C_0q\right)^2+\left[\Gamma q^2\right]^2}\right)\\ +\tfrac{1}{\gamma}b\left(q\right)\left(\tfrac{\omega+\Gamma q^2}{\left(\omega+\Gamma q^2\right)^2+\left[\Gamma q^2\right]^2}+\tfrac{\omega-\Gamma q^2}{\left(\omega-\Gamma q^2\right)^2+\left[\Gamma q^2\right]^2}\right)\Big\}\end{aligned} \tag{3.17}$$

where $\chi_T$ is the isothermal compressibility, $D_T = \lambda/(m\rho_0 C_p)$ is the thermal diffusivity, $C_0 = \left(\frac{\partial p}{\partial \rho}\right)_T$ is the isothermal sound speed, $C_p$ is isobaric specific heat and $\Gamma = \frac{1}{2}\left[\frac{(\gamma-1)\lambda}{m\rho_0 C_p} + \frac{\left(\eta_b + \frac{1}{3}\eta_s\right)}{m\rho_0}\right]$.

Except for the last term, which is usually small and difficult to observe experimentally, the light-scattering spectrum, given by Eq.[3.17], is the sum of three Lorentzian lines. The first term represents the unshifted *Rayleigh line* due to the heat fluctuation which is a Lorentzian line with half-width at half maximum $\Delta\omega_c = D_T q^2$ (typically $10^{-2}$ $GHZ$). $\Delta\omega_c$ is usually smaller than the instrumental resolution (0.2 $GHZ$ for the 6-pass tandem FP interferometer). The next two terms represents the symmetric doublet *Brillouin Doublet.* These are two Lorentzians, with half-width $\Delta\omega_b = \Gamma q^2$, symmetrically shifted by $\pm C_0 q$.

Physically, the *Rayleigh-Brillouin* spectrum arises from the inelastic interaction between a photon and the hydrodynamic modes of the fluids. These hydrodynamic modes are the result of conservation laws [1], [62], [89]. The Brillouin Doublet is due to the inelastic collision between a photon and the "phonons" or sound modes, which are longitudinal collective motions of the molecules in the fluid, producing a frequency shift $\pm C_0 q$. The width of these components gives the lifetime $(\Gamma q^2)^{-1}$ of this "phonon" with wave vector $\vec{q}$. The Rayleigh line, on the other hand, represents the scattering of light due to entropy fluctuation via its coupling to density, which is a purely diffusive mode of the fluid.

## 3.3 Brillouin Scattering in Glassforming Liquids of anisotropic Molecules

In Sec.[**3.2**], we have discussed the *Rayleigh-Brillouin* spectrum in a simple liquid of spherical molecules. Now let's consider a system of anisotropic molecules. If a molecule has an anisotropic shape, both its mechanical (inertia tensor) and dielectric ( dielectric tensor) properties will be anisotropic. Thus the immediate effect of

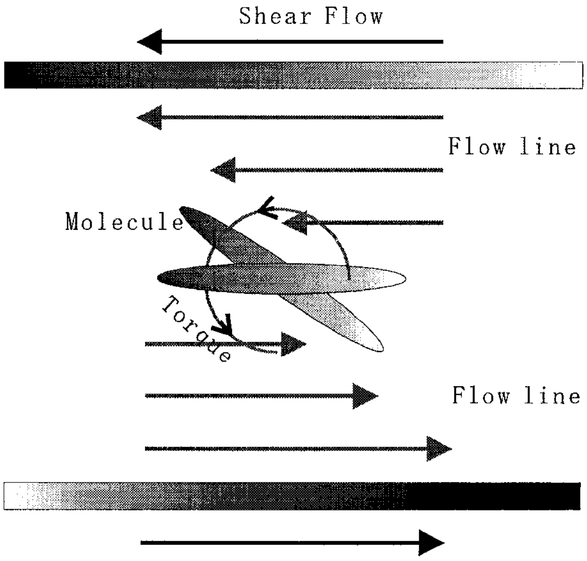

Figure 3-3: Illustration of RT coupling in dense liquid

anisotropy is that the dielectric tensor has non-zero off-diagonal term, which means a new light-scattering channel is opened and the depolarized light-scattering intensity is non-zero. The anisotropic inertia tensor also has consequences. In condensed matter, the rotational motion of the molecules will couple to the shear motion, as shown in Fig.[3-3]. When a molecule is in a shear flow, its neighbors will exert a torque through the molecule-molecule collisions. And this molecule will tend to align in the direction of flow. This is rotation-translation coupling (RT coupling), whose most well-known effect is flow birefringence [8]. In a dilute system, molecule-molecule collisions are infrequent and the RT coupling can be neglected. Therefore rotational and translational motions can be treated independently.

### 3.3.1 Dilute system of anisotropic molecules [1]

In this section, we consider the case of a dilute system. In this system, there are $N$ identical scatterers with polarizability tensor $\overleftrightarrow{\mu}(t)$ at positions: $\vec{r}_1(t), \vec{r}_2(t) ... \vec{r}_N(t)$.

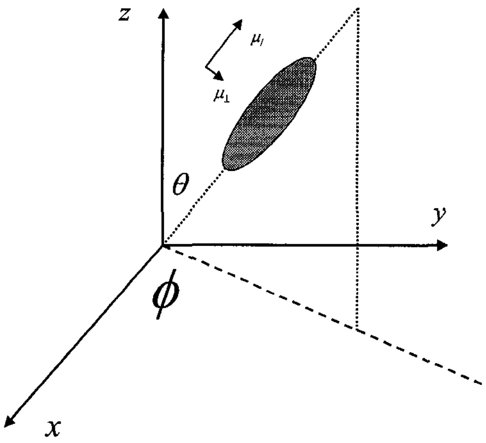

Figure 3-4: The laboratory-fixed axes are $XYZ$ and the symmetry axis of the dielectric ellipsoid points to $(\theta, \phi)$

Thus the dielectric tensor can be written as:

$$\overleftrightarrow{\varepsilon}(\vec{r},t) = \sum_{j=1}^{N} \overleftrightarrow{\mu}_j(t)\,\delta\left(\vec{r}-\vec{r}_j(t)\right) \tag{3.18}$$

We assume that, in this dilute system, light-scattering mainly comes from individual scatterers and the contribution of the average background is negligible, i.e. $\delta\overleftrightarrow{\varepsilon}(\vec{r},t) = \overleftrightarrow{\varepsilon}(\vec{r},t)$. Thus the light-scattering spectrum can be written as:

$$I_{if}(\vec{q},\omega) = \frac{1}{2\pi}\int_{-\infty}^{\infty} dt I_{if}(\vec{q},t)\exp(i\omega t)$$

and

$$I_{if}(\vec{q},t) = |E_0|^2 \sum_{j=1}^{N} \left\langle \mu_{if}^{j}(0)\,\mu_{if}^{j}(t)\exp\left(i\vec{q}\cdot\left[\vec{r}_j(t)-\vec{r}_j(0)\right]\right)\right\rangle$$

where $\mu_{if}^{j}(t)$ depends on the orientation of object $j$. In dilute systems, the rotational motion is independent of the translational motion and we will have

$$I_{if}(\vec{q},t) = |E_0|^2 \sum_{j=1}^{N} \left\langle \mu_{if}^{j}(0)\, \mu_{if}^{j}(t) \right\rangle \left\langle \exp\left(i\vec{q}\cdot\left[\vec{r}_j(t) - \vec{r}_j(0)\right]\right) \right\rangle \; .$$

Because the scattering objects are identical, we finally have:

$$I_{if}(\vec{q},t) = |E_0|^2 N \left\langle \mu_{if}(0)\, \mu_{if}(t) \right\rangle \left\langle \exp\left(i\vec{q}\cdot\left[\vec{r}(t) - \vec{r}(0)\right]\right) \right\rangle \tag{3.19}$$

Now we assume the scattering object is cylindrical. Therefore the dielectric ellipsoid is symmetric; its component parallel to the symmetry axis is $\mu_{\|}$ and component perpendicular to the symmetry axis is $\mu_{\perp}$. The spherical polar coordinates specifying the symmetry axis in the laboratory-fixed frame are $(\theta,\phi)$ as shown in Fig.[3-4]. Under this geometry, we can express components of the dielectric tensor in the laboratory-fixed frame as function of $\mu_{\|}$, $\mu_{\perp}$ and $(\theta,\phi)$. For example

$$\mu_{zz} = \alpha + \left(\frac{16\pi}{45}\right)^{1/2} \beta Y_{2,0}(\theta,\phi) \tag{3.20}$$

$$\mu_{yz} = i\left(\frac{2\pi}{15}\right)^{1/2} \beta\left[Y_{2,1}(\theta,\phi) + Y_{2,-1}(\theta,\phi)\right] \tag{3.21}$$

where $Y_{m,n}$ is the spherical harmonic of order $(m,n)$. In Eq.[3.20],

$$\alpha = \frac{1}{3}\left(\mu_{\|} + 2\mu_{\perp}\right)$$

is $1/3$ of the trace of the dielectric tensor and represents the isotropic part the dielectric tensor which is independent of the orientation, and

$$\beta = \left(\mu_{\|} - \mu_{\perp}\right)$$

measures the anisotropy of the dielectric tensor. These two parameters determine the intensities of the different component of the light-scattering spectrum for this system. Inserting the components of the dielectric tensor in the laboratory-fixed frame into Eq.[3.19], we get:

$$I_{VV}(\vec{q},t) = N\left[\alpha^2 + \left(\frac{16\pi}{45}\right)\beta^2\left(F^{(2)}_{2,0}(t)\right)^2\right]\langle\exp\left(i\vec{q}\cdot[\vec{r}(t)-\vec{r}(0)]\right)\rangle \tag{3.22}$$

$$I_{VH}(\vec{q},t) = \left(\frac{2\pi}{15}\right)\beta^2\left[F^{(2)}_{1,1}(t) + F^{(2)}_{1,-1}(t) + F^{(2)}_{-1,1}(t) + F^{(2)}_{-1,-1}(t)\right]\langle\exp\left(i\vec{q}\cdot[\vec{r}(t)-\vec{r}(0)]\right)\rangle \tag{3.23}$$

where

$$F^{(l)}_{m,n}(t) = \left\langle Y^*_{l,m}(\theta(0),\phi(0))\,Y_{l,n}(\theta(t),\phi(t))\right\rangle$$

are the rotational correlation functions which reflect how the angles $\theta(t)$ and $\phi(t)$ change with time. Eq.[3.22] can be rewritten as

$$I_{VV}(\vec{q},t) = I_{iso}(\vec{q},t) + I_{anis}(\vec{q},t) \tag{3.24}$$

where $I_{iso}(\vec{q},t)$ is the isotropic term due to the translational motion of the center of mass

$$I_{iso}(\vec{q},t) = N\alpha^2\langle\exp\left(i\vec{q}\cdot[\vec{r}(t)-\vec{r}(0)]\right)\rangle$$

and $I_{anis}(\vec{q},t)$ is the anisotropic term due to the rotational dynamics:

$$I_{anis}(\vec{q},t) = N\left(\frac{16\pi}{45}\right)\beta^2\left(F^{(2)}_{2,0}(t)\right)^2\langle\exp\left(i\vec{q}\cdot[\vec{r}(t)-\vec{r}(0)]\right)\rangle\ .$$

Thus, without RT coupling, the polarized spectrum is a simple summation of the isotropic and anisotropic contributions.

If the rotational dynamics is assumed to be described by rotational diffusion, it can be proved that $I_{anis}(\vec{q},t)$ in Eq.[3.24] is proportional to $I_{VH}(\vec{q},t)$ in Eq.[3.23][1]:

$$I_{anis}(\vec{q},t) = \frac{4}{3}I_{VH}(\vec{q},t) \propto \exp(-6\Theta t)\langle\exp\left(i\vec{q}\cdot[\vec{r}(t)-\vec{r}(0)]\right)\rangle\ ,$$

where $\Theta$ is the rotational diffusion coefficient. If $\langle \exp(i\vec{q}\cdot[\vec{r}(t)-\vec{r}(0)])\rangle$ also exhibits simple exponential decay, which is the case for translational diffusion in the simple liquid described by hydrodynamics, Eq.[3.17] in Sec.[**3.2**], $I_{VH}(\vec{q},t)$ will be a simple exponential decay too, which means that the spectrum $I_{VH}(\vec{q},\omega)$ has a Lorentzian line shape in the frequency domain.

### 3.3.2 Pick-Franosch Theory

The discussion for dilute systems is based on the assumption that rotational motion is separable from translational motion. This assumption becomes invalid in a condensed phase, where the two degrees of freedom are coupled. As shown in Fig.[3-3], a molecule, under a shear flow, prefers to orient parallel to the flow direction, due to the torque produced by its neighboring molecules. Therefore, we have rotation-translation (RT) coupling.

One of the consequences of RT coupling in depolarized light-scattering is the so-called Rytov dip. The salol VH 90° (scattering angle) spectra at temperatures from 380 $K$ to 220 $K$ are shown in Fig.[3-5]. Instead of a simple Lorentzian line shape, at high temperatures, we have a small dip centered at $\omega = 0$. This small dip is usually called the Rytov dip and has been discovered by Fabelinski, Starunov *et al* [3] and Stegeman and Stoicheff [5] around 50 years ago. Even before the first experiment, the possibility of such a dip had been suggested by Leontovich [6] and Rytov [7] based on concepts of generalized hydrodynamics. Later, A theoretical analysis based on a two-coupled variable version of the Zwanzig-Mori formalism, which predicts the central dip observed in the high temperature depolarized spectra, was proposed by Andersen and Pecora [9] and by Keyes and Kivelson [10]. In this approach, depolarized light-scattering is assumed to originate entirely from the rotational dynamics of the optically anisotropic molecules which are, however, modified by the RT coupling. While these equations were originally derived using the Zwanzig-Mori formalism, in the small-$q$ limit appropriate to continuum hydrodynamics, Wang showed that they

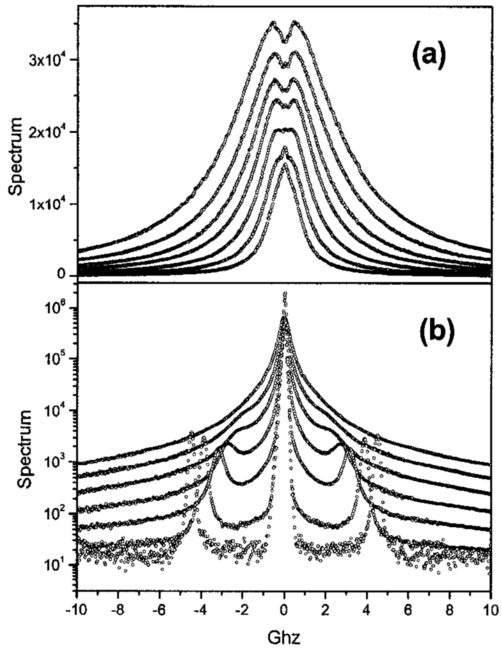

Figure 3-5: Spliced raw $90^0$ depolarized spectra of salol. (a) High temperature spectra in linear-linear plot, from top to bottom: 380 $K$, 370 $K$, 360 $K$, 350 $K$, 340 $K$, 330 $K$, 320 $K$. (b) Mediam and low temperature spectra in Log-linear plot, from top to bottom: 295 $K$, 285 $K$, 280 $K$, 270 $K$, 260 $K$, 240 $K$, 220 $K$. (The spectra have been shifted along $Y$ axis for clarity.)

can also be derived phenomenologically if the hydrodynamic equations of motion of the liquid are extended to include rotational dynamics as well as coupling of rotational motion to shear flow [13], [14].

With cooling of the material through the melting temperature and into the supercooled region, the central (Rytov) dip in the depolarized light-scattering spectrum $I_{VH}(\omega)$ disappears [1] as the broad quasielastic rotational line narrows; eventually a pair of symmetrically placed bumps appears on the wings of the rotational line and sharpen into well-defined transverse acoustic modes. This temperature evolution of $I_{VH}(\omega)$ from doublet to singlet to triplet was explained by Wang [13], who realized that memory effects must be taken into account in the supercooled region. He generalized the Andersen-Pecora analysis by explicitly introducing viscoelasticity, i.e. by replacing the shear viscosity constant $\eta_s$ with a memory function $\eta_s(t)$. However, as Wang noted, a similar viscoelastic generalization should also be included for the other transport coefficients in the dynamic equations[15]. Dreyfus, Pick and their coworkers have further extended the phenomenological theory of depolarized light-scattering by introducing memory functions for all transport coefficients and writing the equation of motion of the rotational variable as a damped oscillator equation. Their approach has been applied, so far, to depolarized light-scattering studies of the molecular glassformers *metatoluidine* [17], [18], [19] and *ortho-terphenyl* [20], [21].

Although the effect of RT coupling has been demonstrated clearly in the VH spectrum by the Rytov dip and transverse modes, it was conventionally ignored in the VV spectrum analysis. In the literature, the polarized Brillouin spectra have usually been analyzed assuming that the rotational contribution is simply added, as a background, to a typical density fluctuation spectrum $I_{VV}(\omega)$ appropriate for a liquid of isotropic molecules, with structural relaxation effects incorporated in a frequency-dependent longitudinal viscosity $\eta_l(\omega)$ [81], [92], [93]. This assumption would be true, if the RT coupling didn't affect the longitudinal motions characterizing $I_{VV}(\omega)$. However,

---

[1] The Rytov dip disappears because of the instrumental resolution, namely it becomes too narrow to be detected. In principle, it is alway present in the spectrum.

longitudinal motion is a superposition of pure compression and shear motion, and the shear component can couple to rotational motion. Thus Dreyfus *et al* [18], Wang [16], and Chappel and Kivelson [22] suggested the existence of RT coupling in longitudinal motions should invalidate the conventional assumption in analyzing $I_{VV}(\omega)$. Approximate expressions for the polarized spectrum $I_{VV}(\omega)$ including rotation-translation coupling were given in Refs. [18] and [16].

Recently, Pick, Franosch Dreyfus, and Latz, have undertaken a new unified analysis of both polarized and depolarized light-scattering spectra using both the phenomenological analysis [18], [23], and a microscopic Zwanzig-Mori approach [24]. Their analysis provides a consistent theory of both polarized and depolarized light-scattering spectra that includes all the effects of RT coupling and viscoelasticity. In particular, the theory predicts that the rotational degree of freedom will change the lineshape of a polarized spectrum through the RT coupling, besides providing a broad background.

In this subsection, we will review the Pick-Franosch theory in detail both phenomenologically and microscopically. First, we will generalize the hydrodynamic equations to include non-hydrodynamic rotational dynamics and introduce a symmetric second rank tensor $\overleftrightarrow{Q}$ to characterize the local anisotropy and write down phenomenologically a damped oscillator equation for it. $\overleftrightarrow{Q}$ and the traceless strain tensor are linearly coupled, again phenomenologically. Thus, the ordinary hydrodynamic equations and the equation for $\overleftrightarrow{Q}$ form a complete set. Then we solve this set of equations analytically to get expressions for the spectra. Finally, we will discuss the microscopic approach, from which all the phenomenological results can be derived.

### $\overleftrightarrow{Q}$ parameter and phenomenological equations

For linear (or axially symmetric) molecules in Fig.[3-4], if $P(\theta, \phi, \vec{r}, t)$ is the probability of finding a molecule at $\vec{r}$ with its symmetry axis pointing in the direction $(\theta, \phi)$, an additional non-hydrodynamic variable, required to describe the departure from isotropy of the average molecular orientations within a small volume element, can be defined as

$$Q_{ij}(\vec{r},t) = \int_V \sin\theta d\theta d\phi P(\theta,\phi,\vec{r},t)[\hat{u}_i(\theta,\phi)\hat{u}_j(\theta,\phi) - \frac{1}{3}\delta_{ij}] \tag{3.25}$$

which forms a symmetric traceless second-rank tensor $\overleftrightarrow{Q}$. More general molecular shapes can be analyzed also. The resulting equations are identical to those derived for the axially symmetric case, but the microscopic definitions of the parameters are modified [91].

In order to generalize the hydrodynamic equations to include $\overleftrightarrow{Q}$, one needs to construct an equation of motion for $\overleftrightarrow{Q}$. Pick and Franosch *et al* used a damped harmonic oscillator equation

$$\frac{\partial^2 Q_{ij}(\vec{r},t)}{\partial t^2} = -\omega_R^2 Q_{ij}(\vec{r},t) - \Gamma\frac{\partial Q_{ij}(\vec{r},t)}{\partial t} + \Lambda' \mu\tau_{ij}(\vec{r},t) \tag{3.26}$$

where $\omega_R$ is a librational frequency, $\Gamma$ is the rotational friction coefficient, $\mu$ is the RT coupling constant, $\Lambda'$ is a constant required because $Q_{ij}(\vec{r},t)$ has different units than $\rho(\vec{r},t)$, and the last term incorporates the coupling of orientation to shear flow. On the other hand, RT coupling also modifies the stress tensor in Eq.[3.10]:

$$\overleftrightarrow{\sigma}(\vec{r},t) = (-p(\vec{r},t) + \eta_B \nabla\cdot\vec{u}(\vec{r},t))\overleftrightarrow{I} + \eta_s\overleftrightarrow{\tau}(\vec{r},t) - \mu\frac{\partial}{\partial t}\overleftrightarrow{Q}(\vec{r},t) ,$$

which can be linearized for small fluctuations:

$$\delta\overleftrightarrow{\sigma}(\vec{r},t) = (-\delta p + \eta_B \nabla\cdot\vec{u}(\vec{r},t))\overleftrightarrow{I} + \eta_s\overleftrightarrow{\tau}(\vec{r},t) - \mu\frac{\partial}{\partial t}\overleftrightarrow{Q}(\vec{r},t) \tag{3.27}$$

where $\delta p = C_0^2\delta\rho(\vec{r},t)$ is the pressure fluctuation. Eq.[3.26] and Eq.[3.27] can be completed with the linearized hydrodynamic equations for small fluctuations:

$$\frac{\partial\delta\rho(\vec{r},t)}{\partial t} + \rho_0\nabla\cdot\vec{u}(\vec{r},t) = 0 \tag{3.28}$$

$$\rho_0 \frac{\partial \vec{u}(\vec{r},t)}{\partial t} - \nabla \cdot \delta \overleftrightarrow{\sigma}(\vec{r},t) = 0 \tag{3.29}$$

We neglect the energy conservation equations, because it only leads to a narrow Rayleigh line, which is beyond the resolution of our instrument.

We note that in the publications of Wang [13], [14], the equations of motion for $\overleftrightarrow{Q}$ was assumed to be a first order relaxation equation rather than a second-order damped oscillation equation. This form reduces to the Anderson-Pecora theory at high temperatures where it is correct. However, at low temperatures when memory effects are important, it leads to anomalies in the memory functions as discussed by Franosch *et al* [24].

As we have discussed in Chapter **2**, relaxation in the supercooled and glassy region is ultra-slow. And the memory effect must be taken into account in the frequency region of our experiment, which means we have to deal with viscoelasticity. A viscoelastic liquid shows liquid-like rheological behavior under low frequency perturbation and solid-like behavior under high frequency perturbation. For example, with a shear perturbation, e.g. $\vec{V} = V_y(z)\vec{j}$, the shear strain is $\gamma_{yz}(t) = \frac{dy(t)}{dz}$ and the shear rate is $\tau_{yz}(t) = \frac{dV_y(t)}{dz} = \dot{\gamma}_{yz}(t)$. For a simple liquid, the shear stress is $\sigma_{yz}(t) = \eta_s \tau_{yz}(t) = \eta_s \dot{\gamma}_{yz}(t)$, whose frequency representation, using the Laplace transform convention in Eq.[3.36], is

$$\sigma_{yz}(\omega) = i\eta_s\omega\gamma_{yz}(\omega) \tag{3.30}$$

and for an ideal Hooke's law solid, the shear stress is $\sigma_{yz}(t) = G_s\gamma_{yz}(t)$, whose frequency representation is:

$$\sigma_{yz}(\omega) = G_s\gamma_{yz}(\omega) \quad . \tag{3.31}$$

In Eq.[3.30] and Eq.[3.31], $\eta_s$ and $G_s$ are the shear viscosity and shear modulus respectively and $\gamma_{yz}(\omega)$ is the Fourier transform of the shear strain $\gamma_{yz}(t) = \frac{dy(t)}{dz}$.

We can incorporate viscoelasticity by generalizing either $\eta_s$ or $G_s$ into a memory function [62]. In our case, we start from a liquid formalism. Thus the generalization can be made to $\eta_s$, for $\vec{V} = V_y(z)\vec{j}$:

$$\sigma_{yz}(t) = \int_0^t \eta_s(t-t')\frac{dV_y(t')}{dz}dt' \equiv \eta_s(t) \otimes \dot{\gamma}_{yz}(t) \tag{3.32}$$

where the symbol $\otimes$ stands for convolution. In principle, the memory function $\eta_s(t)$ can be determined microscopically by the Kubo relation [62]: $\eta_s(t) = \frac{n}{k_B T}\langle\sigma_{zx}(t)\,\sigma_{zx}(0)\rangle$, However, in practice, $\eta_s(t)$ is usually modeled phenomenologically [62], [88], [94]. The constraint of the generalization is that Eq.[3.32] has solid- and liquid-like behavior in the high and low frequency limit respectively, as shown in Eq.[3.30] and Eq.[3.31].

In the frequency domain, Eq.[3.32] reads:

$$\sigma_{yz}(\omega) = \omega\eta_s(\omega)\,\gamma_{yz}(\omega) \ .$$

In order to satisfy the constraints in the low and high frequency limits (Eq.[3.30] and Eq.[3.31]), we must require $\eta_s(\omega) \to i\eta_s\,(\omega\tau \ll 1)$ and $\eta_s(\omega) \to \frac{G}{\omega}\,(\omega\tau \gg 1)$, where $\tau$ is the characteristic relaxation time. One expression satisfying these requirements is :

$$\eta_s(\omega) = \frac{iG\tau}{1+i\omega\tau}$$

which was first introduced in the study of viscoelasticity by Maxwell [62], [94] and gives $\eta_s = G\tau$ (the Maxwell relation). In the Maxwell model $\eta_s(t)$ decays exponentially.

In the Pick-Franosch theory, all transport coefficients are generalized following Eq.[3.32], and the constitutive relation is written as

$$\delta\overleftrightarrow{\sigma}(\vec{r},t) = \left(-C_0^2\delta\rho(\vec{r},t) + \eta_b(t)\otimes\nabla\cdot\vec{u}(\vec{r},t)\right)\overleftrightarrow{I} + \eta_s(t)\otimes\overleftrightarrow{\tau}(\vec{r},t) - \mu(t)\otimes\frac{\partial}{\partial t}\overleftrightarrow{Q}(\vec{r},t) \tag{3.33}$$

and Eq.[3.26] is:

$$\frac{\partial^2 Q_{ij}(\vec{r},t)}{\partial t^2} = -\omega_{_R}^2 Q_{ij}(\vec{r},t) - \Gamma(t)\otimes\frac{\partial Q_{ij}(\vec{r},t)}{\partial t} + \Lambda'\mu(t)\otimes\tau_{ij}(\vec{r},t) \tag{3.34}$$

where $\eta_b(t)$, $\eta_s(t)$, $\mu(t)$ and $\Gamma(t)$ are, respectively, the bulk and shear viscosities, the RT coupling and the rotational friction functions.

After discussion of the dynamics, let's look at the dielectric properties. From symmetry considerations, the diagonal elements of $\delta\overleftrightarrow{\varepsilon}$ can couple to fluctuations in both density and orientation, while the off-diagonal elements can couple only to orientation:

$$\delta\overleftrightarrow{\varepsilon}(\vec{r},t) = a\delta\rho(r,t)\overleftrightarrow{I} + b\overleftrightarrow{Q}(r,t) \tag{3.35}$$

where $a$ and $b$ are material-dependent constants.

### Spectral expressions for polarized and depolarized scattering

After laying down the close set of equations, in this section we will solve Eqs.[3.28], [3.29], [3.33] and [3.34], to get the spectral expressions by Fourier and Laplace transformation:

$$F(\vec{q},\omega) = LFT(F(\vec{r},t)) = i\int_0^\infty dt\exp(-i\omega t)\int d\vec{r}\exp(i\vec{q}\cdot\vec{r})\,F(\vec{r},t)$$

where

$$LT.(F(\vec{r},t)) = i\int_0^\infty dt\exp(-i\omega t)\,F(\vec{r},t) \tag{3.36}$$

is the Laplace transform[2] and

$$FT.(F(\vec{r},t)) = \int d\vec{r}\exp(i\vec{q}\cdot\vec{r})\,F(\vec{r},t) \tag{3.37}$$

---

[2] This follows R. M. Pick's convention, which is different from the one used in MCT derivations Eq.[2.27] and the conventional definition : $LT.(F(\vec{r},t)) = \int_0^\infty dt\exp(-st)\,F(\vec{r},t)$. This convention is used in the derivation of Pick-Franosch theory.

is the Fourier transform. The appropriate initial conditions are : $\vec{u}\left(\vec{q},0\right)=0$, $\partial_t\overleftrightarrow{Q}\left(\vec{q},0\right)=0$.

From Eqs.[3.3], [3.4], [3.5] and [3.35], we can express the polarized and depolarized spectra using this Fourier-Laplace transform convention as:

$$I_{VV}(\vec{q},\omega)=\begin{array}{c}A\mathcal{I}m\{a^2\left\langle\delta\rho\left(\vec{q},\omega\right)\delta\rho\left(\vec{q},0\right)\right\rangle+\\ 2ab\left\langle Q_{yy}\left(\vec{q},0\right)\delta\rho\left(\vec{q},0\right)\right\rangle+b^2\left\langle Q_{yy}\left(\vec{q},\omega\right)Q_{yy}\left(\vec{q},0\right)\right\rangle\}\end{array}\tag{3.38}$$

$$\begin{gathered}I_{VH}(\vec{q},\omega)=Ab^2\mathcal{I}m\{\left\langle Q_{xy}\left(\vec{q},\omega\right)Q_{xy}\left(\vec{q},0\right)\right\rangle\sin\left(\theta/2\right)\\ -2\left\langle Q_{xy}\left(\vec{q},\omega\right)Q_{yz}\left(\vec{q},0\right)\right\rangle\sin\left(\theta/2\right)\cos\left(\theta/2\right)+\left\langle Q_{yz}\left(\vec{q},\omega\right)Q_{yz}\left(\vec{q},0\right)\right\rangle\cos\left(\theta/2\right)\}\end{gathered}\tag{3.39}$$

where $\mathcal{I}m\{...\}$ stands for the imaginary part, $A=\left[\frac{|E_0|^2k_f^4}{32\pi^3R^2\varepsilon_0^2}\right]$ and $\theta$ is the scattering angle. In Eqs.[3.38] and [3.39], $Q_{ij}$ is the element of $\overleftrightarrow{Q}$ tensor, $Q_{ij}\left(\vec{q},0\right)$ is the Fourier transform of the initial value of $Q_{ij}\left(\vec{r},t\right)$

$$Q_{ij}\left(\vec{q},0\right)=\int d\vec{r}\exp\left(i\vec{q}\cdot\vec{r}\right)Q_{ij}\left(\vec{r},0\right)$$

and $Q_{ij}\left(\vec{q},\omega\right)$ is the Laplace-Fourier transform of $Q_{ij}\left(\vec{r},t\right)$

$$Q_{ij}\left(\vec{q},\omega\right)=LFT\left(Q_{ij}\left(\vec{r},t\right)\right)\ .$$

Thus the calculation of the spectrum boils down to calculating the averages like $\left\langle\delta\rho\left(\vec{q},\omega\right)\delta\rho\left(\vec{q},0\right)\right\rangle$, $\left\langle Q_{yy}\left(\vec{q},\omega\right)Q_{yy}\left(\vec{q},0\right)\right\rangle$ and so on, which can be obtained from the set of dynamical equations. For completeness, we show most of the mathematical details. Readers can skip the derivations and go directly to Eq.[3.55] and Eq.[3.60] for the VV and VH spectral expressions.

Apply $\nabla\cdot$ to Eq.[3.29]:

$$\rho_0\frac{\partial\left(\nabla\cdot\vec{u}\left(\vec{r},t\right)\right)}{\partial t}-\nabla\cdot\left(\nabla\cdot\delta\overleftrightarrow{\sigma}\left(\vec{r},t\right)\right)=0\tag{3.40}$$

and $\nabla \cdot (\nabla \cdot)$ to Eq.[3.33]:

$$
\begin{aligned}
\nabla \cdot \left(\nabla \cdot \delta \overleftrightarrow{\sigma}\left(\vec{r}, t\right)\right) &= \partial_i \left(\left(\nabla \cdot \delta \overleftrightarrow{\sigma}\left(\vec{r}, t\right)\right)_j\right) \\
&= \nabla^2 \left(-C_0^2 \delta \rho\left(\vec{r}, t\right) + \eta_b\left(t\right) \otimes \nabla \cdot \vec{u}\left(\vec{r}, t\right)\right) \\
&+ \tfrac{4}{3}\eta_s\left(t\right) \otimes \nabla^2 \left(\nabla \cdot \vec{u}\left(\vec{r}, t\right)\right) - \mu\left(t\right) \otimes \partial_j \left\{\partial_i[\partial_t Q_{ij}\left(\vec{r}, t\right)]\right\}
\end{aligned}
\qquad (3.41)
$$

[3]. Thus we can eliminate $\delta \overleftrightarrow{\sigma}\left(\vec{r}, t\right)$ by inserting Eq.[3.41] into Eq.[3.40] and then do Laplace-Fourier transform:

$$
i\Psi\left(\vec{q}, \omega\right)\left[\omega \rho_0 - q^2 \left(\eta_b\left(\omega\right) + \frac{4}{3}\eta_s\left(\omega\right)\right)\right] - C_0^2 q^2 \delta p\left(\vec{q}, \omega\right) - q^2 \omega \mu\left(\omega\right) Q_{zz}\left(\vec{q}, \omega\right) = 0 \qquad (3.42)
$$

where

$$
\Psi\left(\vec{q}, \omega\right) = LFT\left(\nabla \cdot \vec{u}\left(\vec{r}, t\right)\right)
$$

and only $Q_{zz}\left(\vec{q}, \omega\right)$ survives, see Appendix B. Laplace-Fourier transform Eq.[3.34] for $i = j = z$:

$$
Q_{zz}\left(\vec{q}, \omega\right) = \frac{1}{\omega}\left(1 - \frac{\omega_R^2}{D\left(\omega\right)}\right) Q_{zz}\left(\vec{q}, 0\right) - i\Lambda' \frac{\mu\left(\omega\right)}{D\left(\omega\right)} \frac{4}{3} \Psi\left(\vec{q}, \omega\right) \qquad (3.43)
$$

where

$$
D\left(\omega\right) = \omega_R^2 + \omega \Gamma\left(\omega\right) - \omega^2 \, . \qquad (3.44)
$$

Laplace-Fourier transform Eq.[3.28]:

$$
-i\left(\omega \delta \rho\left(\vec{q}, \omega\right) - \delta \rho\left(\vec{q}, 0\right)\right) = \rho_0 \qquad (3.45)
$$

---

[3] Sum over the repeated indices.

Solving Eqs.[3.42],.[3.43] and [3.45], we will have

$$\begin{aligned}
&\delta\rho\left(\vec{q},\omega\right) = \tfrac{q^2}{\omega}P_l\left(\omega\right)\left[C_0^2\delta\rho\left(\vec{q},0\right) - r\left(\omega\right)\omega_{_R}^2 Q_{zz}\left(\vec{q},0\right)\right] && (a)\\
&\Psi\left(\vec{q},\omega\right) = \tfrac{-i}{\rho_0}q^2 P_l\left(\omega\right)\left[C_0^2\delta\rho\left(\vec{q},0\right) - r\left(\omega\right)\omega_{_R}^2 Q_{zz}\left(\vec{q},0\right)\right] && (b)\\
&Q_{zz}\left(\vec{q},\omega\right) = \tfrac{1}{\omega}\left(1 - \tfrac{\omega_{_R}^2}{D(\omega)}\right)Q_{zz}\left(\vec{q},0\right)\\
&-i\Lambda'\tfrac{\mu(\omega)}{D(\omega)}\tfrac{4}{3}\left\{\tfrac{-i}{\rho_0}q^2 P_l\left(\omega\right)\left[C_0^2\delta\rho\left(\vec{q},0\right) - r\left(\omega\right)\omega_{_R}^2 Q_{zz}\left(\vec{q},0\right)\right]\right\} && (c)
\end{aligned} \tag{3.46}$$

where

$$P_l\left(\omega\right) = \left[\omega^2 - \frac{q^2}{\rho_0}\left(C_0^2\rho_0 + \omega\eta_l\left(\omega\right)\right)\right]^{-1}, \tag{3.47}$$

$$\omega\eta_l\left(\omega\right) = \omega\eta_b\left(\omega\right) + \frac{4}{3}\left(\omega\eta_s\left(\omega\right) - \Lambda' r^2\left(\omega\right)D\left(\omega\right)\right)$$

and

$$r\left(\omega\right) = \omega\frac{\mu\left(\omega\right)}{D\left(\omega\right)}. \tag{3.48}$$

Laplace-Fourier transforming Eq.[3.34] for $i = j = 2$ and plugging in Eq.[3.46].$(b)$, we have:

$$Q_{yy}\left(\vec{q},\omega\right) = \frac{1}{\omega}\left(1 - \frac{\omega_{_R}^2}{D\left(\omega\right)}\right)Q_{yy}\left(\vec{q},0\right) + \frac{2}{3}\frac{\Lambda'}{\omega}\frac{r\left(\omega\right)}{\rho_0}q^2 P_l\left(\omega\right)\left[C_0^2\delta\rho\left(\vec{q},0\right) - r\left(\omega\right)\omega_{_R}^2 Q_{zz}\left(\vec{q},0\right)\right] \tag{3.49}$$

Substituting Eq.[3.49] and Eq.[3.46] in to Eq.[3.38], we will be able to express the polarized spectrum in terms of various static averages like $\left\langle\left|\delta\rho\left(\vec{q},0\right)\right|^2\right\rangle$ and $\left\langle\delta\rho\left(\vec{q},0\right)Q_{zz}\left(\vec{q},0\right)\right\rangle$, which are actually related. Let's look at various static averages. First, due to the different rotational symmetry of $\delta\rho\left(\vec{q},0\right)$ and $Q_{zz}\left(\vec{q},0\right)$, cross terms like $\left\langle\delta\rho\left(\vec{q},0\right)Q_{zz}\left(\vec{q},0\right)\right\rangle$ are negligible. Second, because $\overleftrightarrow{Q}$ is a traceless, second rank tensor and the liquid is isotropic macroscopically, we have

$$\left\langle Q_{ij}\left(\vec{q},0\right)Q_{kl}\left(\vec{q},0\right)\right\rangle = \Phi^2\Delta_{ij,kl} \tag{3.50}$$

where $\Delta_{ij,kl}$ is a fourth-rank tensor,

$$\Delta_{ij,kl} = \left( \delta_{ik}\delta_{jl} + \delta_{il}\delta_{jk} - \frac{2}{3}\delta_{ij}\delta_{kl} \right) \tag{3.51}$$

Thus we have

$$\left\langle |Q_{zz}(\vec{q},0)|^2 \right\rangle = \left\langle |Q_{yy}(\vec{q},0)|^2 \right\rangle = \frac{4}{3}\Phi^2 \tag{3.52}$$

$$\left\langle Q_{yy}(\vec{q},0)\, Q_{zz}(\vec{q},0) \right\rangle = -\frac{1}{2}\left\langle |\delta Q_{33}(\vec{q},0)|^2 \right\rangle \tag{3.53}$$

Also, due to the time reversal symmetry of the system or microscopic reversibility (see *P. 508* in [63]):

$$\left\langle \delta\rho(\vec{q},\omega)\, Q_{yy}(\vec{q},0) \right\rangle = \left\langle Q_{yy}(\vec{q},\omega)\, \delta\rho(\vec{q},0) \right\rangle \ .$$

Thus from Eq.[3.46] $(a)$ and Eq.[3.49], we can easily get:

$$\left\langle Q_{yy}(\vec{q},0)\, Q_{zz}(\vec{q},0) \right\rangle = -\frac{2}{3}\frac{\Lambda'}{\rho_0}\frac{C_0^2}{\omega_{\scriptscriptstyle R}^2}\left\langle |\delta\rho(\vec{q},0)|^2 \right\rangle \ . \tag{3.54}$$

Thus only the single quantity $\Phi$ is needed to characterize the static averages, as seen from Eq.[3.52], [3.53] and [3.54].[4]

Finally inserting Eq.[3.49] and Eq.[3.46] into Eq.[3.38] and simplifying the expression using the static average relations given above, we obtain:

$$I_{VV}(\vec{q},\omega) = \frac{I}{\omega}\mathcal{I}m\left\{ b^2\frac{4}{3}\left(1 - \frac{\omega_{\scriptscriptstyle R}^2}{D(\omega)}\right) + \frac{\rho_0}{\Lambda'}\omega_{\scriptscriptstyle R}^2 q^2 P_l(\omega)\left(a + \frac{2\Lambda' b}{3\rho_0}r(\omega)\right)^2 \right\} \tag{3.55}$$

where $I = A\Phi^2$, $r(\omega)$, $D(\omega)$, and the longitudinal phonon propagator $P_l(\omega)$, are defined in Eq.[3.48], Eq.[3.44] and Eq.[3.47] respectively.

Following the same Laplace-Fourier transform method, one can easily get the

---

[4] We can see from Eq.[3.50] to Eq.[3.54]: $\frac{3\varpi_{\scriptscriptstyle R}^2}{4\Lambda'}\left\langle |\delta Q_{33}(\vec{q},0)|^2 \right\rangle = \frac{C_0^2}{\rho_0}\left\langle |\delta\rho(\vec{q},0)|^2 \right\rangle$, which indicates the equipartition of energy between the translational and rotational motions.

expression for $Q_{xy}(\vec{q},\omega)$ and $Q_{yz}(\vec{q},\omega)$ as:

$$Q_{xy}(\vec{q},\omega) = \frac{1}{\omega}\left(1 - \frac{\omega_{R}^{2}}{D(\omega)}\right) Q_{xy}(\vec{q},0) \tag{3.56}$$

$$Q_{yz}(\vec{q},\omega) = \left\{\frac{1}{\omega}\left(1 - \frac{\omega_{R}^{2}}{D(\omega)}\right) + \frac{9}{4}\frac{\rho_0}{\Lambda'}\omega_{R}^{2}q^{2}\left(\frac{2\Lambda'}{3\rho_m}r(\omega)\right)^{2} P_t(\omega)\right\} Q_{yz}(\vec{q},0) \tag{3.57}$$

where $P_t(\omega)$ is the transverse phonon propagator:

$$P_t(\omega) = \left[\omega^2 - \frac{q^2}{\rho_0}\left(\omega\eta_s(\omega) - \Lambda' r^2(\omega) D(\omega)\right)\right]^{-1}. \tag{3.58}$$

From Eq.[3.56], we can see that the normalized autocorrelation function of $Q_{xy}(\vec{q},\omega)$ is:

$$\frac{\langle Q_{xy}(\vec{q},\omega) Q_{xy}(\vec{q},0)\rangle}{\langle Q_{xy}(\vec{q},0) Q_{xy}(\vec{q},0)\rangle} = \mathcal{I}m\left\{\frac{1}{\omega}\left(1 - \frac{\omega_{R}^{2}}{D(\omega)}\right)\right\}. \tag{3.59}$$

Inserting Eq.[3.59] into Eq.[3.39], and again simplifying the expression using the static averages, we obtain:

$$I_{VH}(\vec{q},\omega) = \frac{I}{\omega}\mathcal{I}m\left\{b^2\left(1 - \frac{\omega_{R}^{2}}{D(\omega)}\right) + \left(\cos^2(\theta/2)\right)\frac{9}{4}\frac{\rho_0}{\Lambda'}\omega_{R}^{2}q^{2}\left(\frac{2\Lambda' b}{3\rho_0}r(\omega)\right)^{2} P_t(\omega)\right\} \tag{3.60}$$

where $I = A\Phi^2$, and the transverse phonon propagator $P_t(\omega)$ is defined in Eq.[3.58].

If we neglect the RT coupling, by setting $\mu(t) = 0$ in both Eq.[3.33] and Eq.[3.34], the spectral expression can be worked out easily:

$$I_{VH}(\vec{q},\omega) = \frac{A}{\omega}\mathcal{I}m\left\{b^2\left(1 - \frac{\omega_{R}^{2}}{D(\omega)}\right)\right\} \tag{3.61}$$

and

$$I_{VV}(\vec{q},\omega) = \frac{A}{\omega}\mathcal{I}m\left\{b^2\frac{4}{3}\left(1 - \frac{\omega_{R}^{2}}{D(\omega)}\right)\Phi^2 + a^2q^2C_0^2P_l^d(\omega)\left\langle\left|\delta\rho(\vec{q},0)\right|^2\right\rangle\right\} \tag{3.62}$$

where

$$P_l^d(\omega) = \left\{\omega^2 - \frac{q^2}{\rho_0}\left[\rho_0 C_0^2 + \omega\eta_b(\omega) + \frac{4}{3}\left[\omega\eta_s(\omega)\right]\right]\right\}^{-1} .$$

In this case, the VH spectrum is purely rotational and $\vec{q}$ independent and the VV spectrum is a sum of rotational and translational contributions as expected. The second term in Eq.[3.62] is equivalent to the term proportional to $a^2$ in Eq.[3.55], considering the relation between the static averages from Eq.[3.50] to Eq.[3.54].

Both the polarized (Eq.[3.55]) and depolarized (Eq.[3.60]) spectra contain two terms. The first term in Eq.[3.60] is

$$I_{VH}^B(\vec{q},\omega) = I \cdot b^2 \mathcal{I}m\{R(\omega)\} \text{ ,where } R(\omega) = \frac{1}{\omega}\left(1 - \frac{\omega_R^2}{D(\omega)}\right) \tag{3.63}$$

which can be looked at in two ways. First, it is exactly the backscattering depolarized spectrum, easily seen by setting $\theta = \pi$ in Eq.[3.60]. Second, from Eq.[3.59], we see it is the spectrum of $Q_{xy}(\vec{q},\omega)$, which doesn't couple to the translational motion. Thus $I_{VH}^B(\vec{q},\omega)$, the backscattering depolarized spectrum, describes the pure rotational decay. In the $I_{VH}^B(\vec{q},\omega)$ data analysis Sec.[**5.2**], $R(\omega)$ is modeled by a hybrid function:

$$R(\omega) = R_0\left\{\left[1 - (1 + i\omega\tau_R)^{-\beta_R}\right] + p_R\left[i\omega(\tau_R^{-1} + i\omega)^{a_R - 1}\right]\right\} .$$

Also 4/3 of the same term appears in the polarized spectrum in Eq.[3.60], which provides a background for the polarized spectrum. In addition to the pure rotational term, there is a second term in the depolarized spectrum, Eq.[3.60], which is due to the RT Coupling and produces the Rytov dip at high temperatures and the transverse modes at low temperatures, as seen in Fig.[3-5]. In polarized spectrum, besides the background, the rotational motion also changes the lineshape of the $q$-depedent term via RT coupling, which can be seen from the second term in Eq.[3.55]. It contains a term proportional to $a^2$, corresponding to the contribution of translational motion. It also contains the term proportional to $b^2$, which is the contribution of rotational motion, and a cross term proportional to $ab$.

RT coupling also causes a modification of both the transverse and longitudinal phonon propagators, Eq.[3.58] and Eq.[3.47], namely it reduces the shear viscosity by $\Lambda' r^2(\omega)\, D(\omega)$.

### Spectral expressions for fitting

Due to the existence of four memory functions, the spectral expressions, Eq.[3.55] and Eq.[3.60], contain too many parameters to be fit directly to experimental data. However, as shown below, two of the memory functions, $\mu(\omega)$ and $\Gamma(\omega)$, can be reduced to a single fitting parameter under one plausible assumption.

The spectral region of interest $(0 - 50\ GHZ)$ is far below the microscopic vibrational frequency $\omega_R$ $(\sim 10^3\ GHZ)$; thus $\omega^2 << \omega_R^2$. It can also be proved that $\omega^2 << \omega\Gamma(\omega)$[5], so we approximate $D(\omega)$, in Eq.[3.44], by

$$D(\omega) \approx \omega_R^2 + \omega\Gamma(\omega)\ ,$$

which means

$$\omega\Gamma(\omega) \approx D(\omega) - \omega_R^2\ .$$

Next, we assume that the transport coefficients $\mu(\omega)$ and $\Gamma(\omega)$ have the same frequency dependence and their ratio $z$ is therefore a constant, which depends on temperature, but not on frequency:

$$\mu(\omega)/\Gamma(\omega) = z\,(T)\ . \tag{3.64}$$

---

[5] This can be checked numerically by using the fitting results from the Hybrid fit to backscattering spectra, see Sec.[5.2], where $R(\varpi) = \left(1 - \frac{\varpi_R^2}{\varpi_R^2 + \varpi\Gamma(\varpi) - \varpi^2}\right)$ is modelled as hybrid function and all the parameters are known. If we assume $\varpi_R \sim 10^3 GHZ$, we can calculate $\varpi\Gamma(\varpi)$ numerically, whose imaginary and real part are both 2-3 orders larger than $\varpi^2$ in frequencies below 100 $GHZ$.

Eq.[3.48] for $r(\omega)$ thus becomes:

$$r(\omega)=\frac{\omega\mu(\omega)}{D(\omega)}=\frac{\omega z\Gamma(\omega)}{D(\omega)}=z\frac{\omega\Gamma(\omega)}{D(\omega)}=z\frac{D(\omega)-\omega_R^2}{D(\omega)}=z\left[1-\frac{\omega_R^2}{D(\omega)}\right] \tag{3.65}$$

Eq.[3.64] is exact at high temperatures, where the frequency dependence of both $\mu(\omega)$ and $\Gamma(\omega)$ disappears within the frequency range of our experiment. Yet, at low temperatures, where memory effects must be taken into account, there is no theoretical or experimental proof of Eq.[3.64]. Combining Eq.[3.63] and Eq.[3.65]:

$$r(\omega)=zR\left(\omega\right) \tag{3.66}$$

Inserting Eq.[3.66] into Eq.[3.60]:

$$\begin{gathered}I_{VH}(\vec{q},\omega)=\tfrac{I_0}{\omega}\mathcal{I}m\left[R(\omega)+\left(\cos^2\left(\theta/2\right)\right)\Lambda(q^2/\rho_0)R^2(\omega)P_t\left(\omega\right)\right]\\ \text{and } P_t\left(\omega\right)=\left\{\omega^2-(q^2/\rho_0)\{\omega\eta_s(\omega)-\Lambda R^2(\omega)/[1-R(\omega)]\}\right\}^{-1}\end{gathered} \tag{3.67}$$

where $I_0 = I\cdot b^2$ and $\Lambda(T) = \omega_R^2\Lambda' z^2$. Note that $\Lambda(T)$ is now the RT coupling constant. Putting Eq.[3.66] into Eq.[3.55]:

$$\begin{gathered}I_{VV}(\omega)=\tfrac{I_0}{\omega}\mathcal{I}m\left\{\tfrac{4}{3}R(\omega)+\tfrac{q^2}{\rho}\Lambda\left[S+\tfrac{2}{3}R(\omega)\right]^2P_l\left(\omega\right)\right\}\\ \text{and }\ P_l\left(\omega\right)=\left\{\omega^2-\tfrac{q^2}{\rho_0}\left[\rho_0C_0^2+\omega\eta_b(\omega)+\tfrac{4}{3}\left[\omega\eta_s(\omega)-\Lambda R^2(\omega)/[1-R(\omega)]\right]\right]\right\}^{-1}\end{gathered} \tag{3.68}$$

where $S = a\rho/\Lambda' bz$.

In order to apply Eq.[3.67] and Eq.[3.68], we have to model the memory functions of the shear and bulk viscosities. The shear viscosity $\eta_s\left(\omega\right)$ and bulk viscosity $\eta_b\left(\omega\right)$, describe how the simple shear and isotropic compression relax and can be measured directly in experiment. In dynamic viscosity measurements, Menon *et al* [58] showed that $\eta_s\left(\omega\right)$ has a stretched exponential behavior, as shown in Fig.[3-6]. Because of the strong coupling to structural relaxation, we assume $\eta_s\left(\omega\right)$ exhibits the same short time characteristics as structural relaxation predicted by MCT, namely the critical

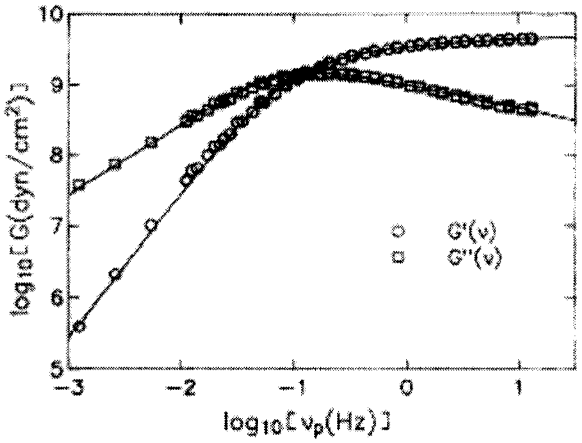

Figure 3-6: Real (circle) and imaginary (square) part of dynamic viscosity of glass-forming liquid di-n-butylphthalate. The line is a Cole-Davision fits with $\beta = 0.34$

part in the high frequency region. Thus we model $\eta_s(\omega)$ by the hybrid function Eq.[2.45]:

$$\omega\eta_s(\omega) = \eta_s^o \left\{ \left[1 - (1 + i\omega\tau_s)^{-\beta_s}\right] + p_s\left[i\omega(\tau_s^{-1} + i\omega)^{\alpha_s - 1}\right] \right\} . \tag{3.69}$$

From the limiting values of the hybrid function discussed in Sec.[**2.3.3**], we can see $\eta_s(\omega)$ has liquid-like behavior in the low frequency limit and solid-like behavior in the high frequency limit in our frequency window.

In the VV analysis, we further assume the bulk viscosity $\eta_b(\omega)$ is proportional to $\eta_s(\omega)$. Thus

$$\eta_b(\omega) + \frac{4}{3}\eta_s(\omega) = V\eta_s(\omega) \tag{3.70}$$

where

$$V = \frac{\eta_b(\omega)}{\eta_s(\omega)} + \frac{4}{3} .$$

Beyond the coupling between the viscosities and structural relaxation, which is essentially inter-molecular motion and is represented by the hybrid function, there are other processes like intramolecular motion, attenuating the longitudinal sound wave. We use a constant, which is the "regular" sound attenuation coefficient, to represent these processes. Thus the modified longitudinal phonon propagator reads:

$$P_L(\omega) = \left\{ \omega^2 - \omega_\circ^2 - i\omega\Gamma_0 - \frac{q^2}{\rho}\left[ V\omega\eta_s(\omega) - \frac{4}{3}\Lambda\frac{R^2(\omega)}{1-R(\omega)} \right] \right\}^{-1} \tag{3.71}$$

where $\omega_\circ = qC_0$ and $\Gamma_0$ is the "regular" sound attenuation coefficient.

One immediate test of the theory is that, at high temperatures, the second term of Eq.[3.67] for $I_{VH}^{\theta}(q,\omega)$ should be negative around zero frequency to produce the Rytov dip in our frequency window ( several $GHZ$ ). For high temperatures, all frequency-dependent memory functions can be replaced approximately by their $\omega \rightarrow 0$ limits ($\omega\tau << 1$ for all processes at high temperatures in the range of several $GHZ$ ):

$$R(\omega) \underset{\omega\tau<<1}{\longrightarrow} iR^0\omega\beta\tau_R$$

$$\omega\eta_s(\omega) \underset{\omega\tau<<1}{\longrightarrow} i\omega\eta_s$$

where $\eta_s$ is the static shear viscosity. The modification term to the shear viscosity in the denominator of Eq.[3.67] can be ignored, since $R^2(\omega) \propto (\omega\tau)^2 << 1$. Thus the second term in depolarized spectrum, Eq.[3.67], becomes

$$\begin{aligned} & \frac{I_0}{\omega}\mathcal{I}m\left\{ \frac{(\cos^2(\theta/2))\,\Lambda(q^2/\rho_0)R^2(\omega)}{\omega^2 - (q^2/\rho_0)\{\omega\eta_s(\omega) - \Lambda R^2(\omega)/[1-R(\omega)]\}} \right\} \\ \rightarrow\; & \frac{I_0}{\omega}\mathcal{I}m\left\{ \frac{(\cos^2(\theta/2))\,\Lambda(q^2/\rho_0)\left(iR^0\omega\beta\tau_R\right)^2}{\omega^2 - (q^2/\rho_0)\{\omega\eta_s(\omega)\}} \right\} \\ =\; & -\frac{B}{\omega^2 + (\eta_s q^2/\rho_0)^2} \end{aligned} \tag{3.72}$$

where $B = \frac{I_0\eta_s\Lambda q^4\left(R^0\beta\tau_R\right)^2}{\rho_0^2}\cos^2(\theta/2)$. This is a Lorentzitian with negative sign, which is consistent with Andersen-Pecora theory [9], [1]. We note that, at any temperature, $\omega\tau << 1$ can always be satisfied at extremely low frequencies. Thus Eq.[3.72] holds there, which means there is always a Rytov dip at sufficiently low frequencies in the

VH spectrum, although it may be too narrow to be detected experimentally.

### Microscopic derivation of the Pick-Franosch Theory

In this section, we will discuss briefly the microscopic derivation [24]. The microscopic approach is based on projection formalism identical to the Zwanzig-Mori formalism discussed in Sec.[**2.3.2**] and Appendix **A**. In this approach, the selected variables are $\delta\rho(\vec{q},0)$, $\vec{J}(\vec{q},0)$, $\overleftrightarrow{Q}(\vec{q},0)$ and $\overleftrightarrow{\dot{Q}}(\vec{q},0)$ which are the density fluctuation, momentum, anisotropic parameter, and the time derivative of the anisotropic parameter, respectively. The static averages of the selected variables are:

$$\begin{gathered}
\left\langle\left|\delta\rho\left(\vec{q},0\right)\right|^2\right\rangle = \tfrac{m^2v^2}{C_0^2} \\
\left\langle J_i\left(\vec{q},0\right)J_j\left(\vec{q},0\right)\right\rangle = \delta_{i,j}m^2v^2 \\
\left\langle Q_{ij}\left(\vec{q},0\right)Q_{kl}\left(\vec{q},0\right)\right\rangle = \Phi^2\Delta_{ij,kl} \\
\left\langle \dot{Q}_{ij}\left(\vec{q},0\right)\dot{Q}_{ij}\left(\vec{q},0\right)\right\rangle = \omega_{_R}^2\Delta_{ij,kl}
\end{gathered} \tag{3.73}$$

where $v = \sqrt{k_BT/m}$ is the thermal velocity, $C_0 = v^2/S\left(q \to 0\right)$ is the isothermal sound velocity defined in terms of the long-wavelength limit of the static structure factor, $\omega_{_R} = \sqrt{2k_bT/5I}$ is the characteristic frequency ($I$ is the momentum inertia of the molecule for a rotation around the axis perpendicular to the molecule symmetry axis). Other cross-term averages can be shown to vanish; for details see [24].

The projection operator, which projects any vector onto the subspace spanned by $\delta\rho(\vec{q},0)$, $\vec{J}(\vec{q},0)$, $\overleftrightarrow{Q}(\vec{q},0)$ and $\overleftrightarrow{\dot{Q}}(\vec{q},0)$, can be defined as:

$$\begin{aligned}
\hat{P} = {} & \left|Q_{ij}\left(\vec{q},0\right)\right\rangle \tfrac{1}{2S^2}\left\langle Q_{ij}\left(\vec{q},0\right)\right| + \left|\dot{Q}_{ij}\left(\vec{q},0\right)\right\rangle \tfrac{1}{2\omega_{_R}^2}\left\langle \dot{Q}_{ij}\left(\vec{q},0\right)\right| \\
& + \left|\delta\rho\left(\vec{q},0\right)\right\rangle \tfrac{C_0^2}{m^2v^2}\left\langle \delta\rho\left(\vec{q},0\right)\right| + \left|J_i\left(\vec{q},0\right)\right\rangle \tfrac{1}{m^2v^2}\left\langle J_i\left(\vec{q},0\right)\right|
\end{aligned} \tag{3.74}$$

Franosch *et al* [24] showed that the time evolution operator, $\hat{R}\left(t\right) = \exp\left(i\hat{L}t\right)$, can be exactly reformulated as:

$$\hat{R}\left(t\right) = \hat{R}\left(t\right)\hat{P} + \int_0^t \hat{R}\left(s\right)\hat{P}i\hat{L}\hat{R}'\left(t-s\right)ds + \hat{R}'\left(t\right) \tag{3.75}$$

where

$$\hat{R}'(t) = \hat{Q}\exp\left(i\hat{Q}\hat{L}\hat{Q}t\right)\hat{Q}$$

and $\hat{Q} = 1 - \hat{P}$. A short proof of this identity, Eq.[3.75], and its equivalence to normal Zwanzig-Mori formalism, can be found in Appendix **B**.

With the help of the static averages and Eq.[3.75], the phenomenological equations can be derived as follows. First, we write down the mass and momentum conservation laws:

$$\partial_t \delta\rho(\vec{q}, t) = iq_k J_k(\vec{q}, t)$$

and

$$\partial_t J_k(\vec{q}, t) = iq_l \sigma_{kl}(\vec{q}, t) \tag{3.76}$$

where $\sigma_{kl}(\vec{q}, t)$ is the stress tensor. The traceless part of $\overleftrightarrow{\sigma}$ is $\overleftrightarrow{\psi}$ :

$$\overleftrightarrow{\psi} = \overleftrightarrow{\sigma} - \frac{(\sigma_{xx} + \sigma_{yy} + \sigma_{zz})}{3}\overleftrightarrow{I} \ .$$

We also can write the trivial identity:

$$\partial_t^2 Q_{ij}(\vec{q}, t) = \ddot{Q}_{ij}(\vec{q}, t) \tag{3.77}$$

The stress tensor $\sigma_{kl}(\vec{q}, t)$ in Eq.[3.76] can be generated by letting $\hat{R}(t)$ act on its initial value:

$$\sigma_{kl}(\vec{q}, t) = \hat{R}(t)\,\sigma_{kl}(\vec{q}, 0) \ .$$

Inserting these results in Eq.[3.75] and evaluating all the static averages, we have the final result:

$$\begin{aligned} \sigma_{ij}(\vec{q}, t) = \delta_{ij} C_0^2 \delta\rho(\vec{q}, t) + i\delta_{ij} \int_0^t \eta_b(t-s)\, q_k v_k(\vec{q}, s)\, ds \\ - \int_0^t \eta_s(t-s)\, \tau_{ij}(\vec{q}, s)\, ds + \int_0^t \mu(t-s)\, \dot{Q}_{ij}(\vec{q}, s)\, ds + noise \end{aligned} \tag{3.78}$$

where $\eta_b(t) = \frac{n}{k_B T}\left\langle p(\vec{q}, 0) | \hat{R}'(t) | p(\vec{q}, 0) \right\rangle$, $\eta_s(t) = \frac{n}{k_B T}\left\langle \psi_{xy}(\vec{q}, 0) | \hat{R}'(t) | \psi_{xy}(\vec{q}, 0) \right\rangle$,

$\mu(t) = -\frac{1}{\omega_R^2}\left\langle Q_{xy}(\vec{q},0)\left|\hat{R}'(t)\right|\psi_{xy}(\vec{q},0)\right\rangle$. The *noise* is a term of random force orthogonal to the subspace of selected variables and will be cancelled out when calculating the correlation function. Neglecting the *noise* term, Eq.[3.78] is equivalent to the constitution relation Eq.[3.33]. Apply the same procedure to $\ddot{Q}_{ij}$ and we will have

$$\ddot{Q}_{ij}(\vec{q},t) = -\omega_R^2 Q_{ij}(\vec{q},t) - \int_0^t \Gamma(t-s)\,\dot{Q}_{ij}(\vec{q},s)\,ds + \Lambda' \int_0^t \mu(t-s)\,\tau_{ij}(\vec{q},s)\,ds + noise \tag{3.79}$$

where $\Gamma(t) = \frac{1}{\omega_R^2}\left\langle Q_{xy}(\vec{q},0)\left|\hat{R}'(t)\right|Q_{xy}(\vec{q},0)\right\rangle$, and $\Lambda' = \frac{\omega_R^2 n}{k_B T}$. Neglecting this *noise* term, Eq.[3.79] is equivalent to Eq.[3.34]. Thus the phenomenological equations of Pick *et al* [23] are recovered. Franosch *et al* [24] further showed that all the relevant memory functions have well-behaved long-time behavior, allowing the use of simple modeling functions. It is also possible to show, within the same formalism, that if general molecular shape is included (rather than requiring axial symmetry), the same expressions are obtained for the spectra although the microscopic definitions of memory kernels have to be modified [91].

# Chapter 4

# Experiments

In this chapter, we will discuss the apparatus and procedures used in experiments. In Sec.[**4.1**], the experimental setups will be discussed. The Brillouin scattering apparatus, based on a Sandercock Tandem Febry-Perot interferometer, is our main instrument and therefore will be discussed in detail. Two other instruments, Raman and photon correlation spectroscopies, will be discussed briefly. In Sec.[**4.2**], we will show how the above instruments were applied in our work and will present the full set of experimental data.

## 4.1 Experimental Apparatus

### 4.1.1 Brillouin Scattering Apparatus

**Fabry-Perot Interferometers**

Brillouin scattering spectroscopy using Fabry-Perot interferometers is a well established method for investigating the properties of materials. First let us quickly review the characteristics of a single Fabry-Perot interferometer; more details can be found in standard textbooks e.g. [95]. A single plane Fabry-Perot interferometer (*FPI*), shown in Fig.[4-1], consists of two high quality parallel mirrors separated by the optical path length $D$. This is a standard example of a multi-beam interferometer and the essential aspect of it is that a transmission maximum occurs when light of wavelength $\lambda$, incident normally on the mirrors, satisfies the round-trip resonance condition,

$$n\lambda = 2D$$

where $n$ is any integer. The FPI is a tunable band-pass filter since changing the mirror spacing shifts the resonance wavelengths.

The finesse $F$ of such an instrument is an important characteristic defined as the ratio of the frequency separation of adjacent transmission peaks $(FSR)$ to the peak width at half maximin$(FWHM)$: $F = \frac{FSR}{FWHM}$. The finesse depends on the mirror reflectivity and the departure of the mirror surfaces from ideal planes. In a real system, light is always collected from a finite size source and over a finite solid angle so that incident light is not perfectly parallel. This effect will cause an additional broadening of the transmission peak. Taking into account all these factors, a normal single pass FPI usually has a finesse of about 60. The FPI transmission function is given by:

$$T_1 = \frac{T_0}{1 + \frac{4F^2}{\pi^2}\sin^2\left(\frac{2\pi D}{\lambda}\right)} \tag{4.1}$$

where $T_0$ is the maximum possible transmission of the system. One typical transmission functions, generated by Eq.[4.1], is shown as a function of $D$ for a monochromatic incident light in Fig.[4-1]. One useful parameter, characterizing a FPI, is the contrast, which is defined as the ratio of the maximum transmission to the minimum transmission and is related to the finesse $F$ of the system:

$$C_1 = \frac{T_{\max}}{T_{\min}} = 1 + \frac{4F^2}{\pi^2}$$

The typical contrast for a single pass FPI is $\sim 1000$.

Although the finesse of a single pass FP system can be increased up to a limit of about 80, the low contrast limits its application in observing weak signals in the presence of intense elastically scattered light. This problem can be solved by using a

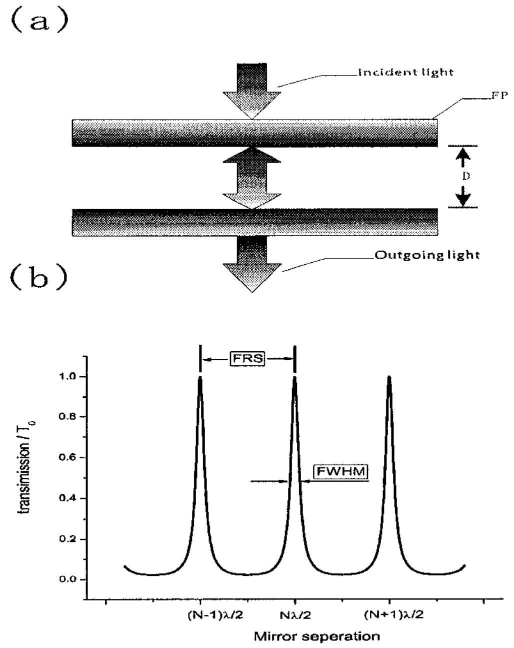

Figure 4-1: (a) A sketch of a plane F-P interferometer. (b) The transmission of monocromatic light through the interferometer as a function of mirror spacing.

multipass FP system [96], [97]. For an n-pass FP system in which the light traverses the FP $n$ times at different positions, the transmission is just the $n$th power of Eq.[4.1]:

$$T_n = (T_1)^n$$

The finesse and the contrast of the system are:

$$F_n = \frac{F}{(2^{1/n} - 1)^{1/2}}$$

$$C_n = (C_1)^n$$

For a 5-pass FP system, which is commonly used, a finesse larger than 70 and a contrast larger than $10^{10}$ can be easily achieved.

A multi-pass interferometer can provide high finesse and high contrast, However, like a single-pass FP interferometer, it suffers from the overlapping of neighboring interference orders. The interference introduces ambiguity to the analysis of the measured spectra and can even make the measurement impossible, if the spectrum contains many or broad, features. This problem can be solved by constructing interferometers consisting of two FPIs of unequal spacing in tandem operation. Light will be transmitted only when both FPIs satisfy the resonance condition simultaneously:

$$n_1\lambda = 2D_1, \text{ and } n_2\lambda = 2D_2 \tag{4.2}$$

where $n_1$ and $n_2$ are integers, and $D_1$ and $D_2$ are the mirror separations of the first and second FPI. The transmission function of a tandem FP interferometer is simply the product of the transmission functions of the two FPIs. The transmission function of such a system, where $D_2$ is slight smaller than $D_1$, is shown in Fig.[4-2]. We can see that the nearby transmission peaks have been suppressed. The mirror spacings can be scanned to produce sensible spectra with this system, only if Eq.[4.2] is accurately satisfied continuously while scanning. Therefore, while scanning, if $D_1$ is shifted by

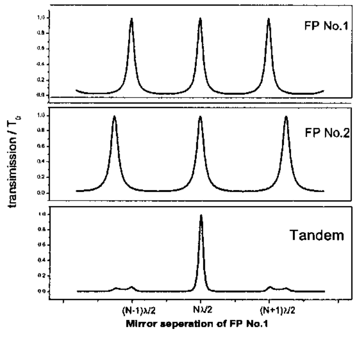

Figure 4-2: The transmission of a tandem FP interferometer, where the mirror seperations of two FPIs are different by a small amount.

$\delta D_1$, $\delta D_2$ must be shifted by:

$$\delta D_2 = \frac{\delta D_1 D_2}{D_1} \ . \tag{4.3}$$

A tandem FP interferometer (TFPI) introduced by Sandercock [98] in 1978 provides a practicable solution to Eq.[4.3]. The Sandercock TFPI, shown in Fig.[4-3], consists of two FPIs in which the scanning mirrors of both interferometers are mounted on a common translation stage. The axis of the first FP is along the scanning direction (indicated by the heavy arrow) while the second is rotated by an angle $\theta$. The spacings are adjusted so that $D_2 = 0$ when $D_1 = 0$. Therefore, the spacing of the two FPIs are related by:

$$D_2 = D_1 \cos\theta$$

which automatically satisfied the synchronization condition of Eq.[4.2] while scanning.

### Overview of Brillouin scattering instrument

The interferometer used in our brillouin scattering experiment is a Sandercock TFPI. In this TFPI, the angle between the second FP axis and the scan axis is $18.4^0$ and the mirror separation range is $0 - 27mm$. The scanning mirrors are mounted on a compound translation stage comprising a deformable parallelogram (for small dis-

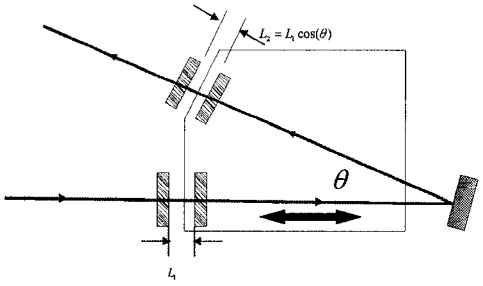

Figure 4-3: Sketch of Sandercock tandem FP interferometer

placements) attached to a crossed roller translation stage (for large displacement). The latter can be driven by a micrometer screw for obtaining the gross setting of the mirror spacing. The interferometer is scanned by means of a piezoelectric transducer acting on the deformable parallelogram. The mirrors in the interferometer are mounted in mirror holders. The position and orientation of each mirror relative to the mirror holder can be adjusted via piezoelectric transducers.

To obtain long-time stability of the system, it is necessary to apply some form of dynamic control in order to maintain both parallel alignment of the mirrors and correct spacing. Two kinds of feedback are used. First, the mirror spacing is sensed using a capactive displacement sensor in the scanning stage and the signal is used in a feedback loop to control the piezoelectric scanning transducer. Besides the capacitive displacement sensor, the final light-scattering signal is also fed back to an interferometer control box. Fine adjustments are done by the control box, to the transducers between the mirrors and holders, to maximize the integrated intensity of the central elastic peak. Therefore, a reference beam, with the same frequency as the excitation light and with stable intensity, is necessary for this feedback.

The 6-pass TFPI Brillouin scattering apparatus in our lab is shown schematically in Fig.[4-4]. Single-mode laser light, from a *Coherent innova 90* laser running at about 250 $mW$ and 5145 Å, is split by $S1$ into two beams: one for reference and the other for excitation. The excitation beam, going though a shutter (shutter-1) and polarizer, is focused on the sample in a cryostat. The reference beam, going through a shutter (shutter-2), focusing lens and neutral filter, reaches beam splitter $S2$ together with scattered light from the sample. The combined scattered beam and reference beam, are focused on a spatial filter, that defines the effective scattering volume. A telescope is used to help focus the combined beam accurately on the spatial filter. Then the beam, collimated by a lens, enters the TFPI after a second polarizer. The combination of the coupling mirror $M2$, corner-cube and the cat's-eye element ($f3$ and $M3$) reflects the beam and adjusts the beam positions to complete the 6-pass ($3 \times 2$) through the TFPI. The scattering configuration in Fig.[4-4] is for 90° scattering. The near-backscattering geometry is achieved by replacing focal lens $f1$ by the combination of flat ($Mb$) and convex ($Mc$) reflecting mirrors, as shown in the lower-left corner in the figure.

Because the frequency response of the photomultiplier tube (PMT) is much wider than the effective free spectral range of TFPI, significant background noise would be caused by the light outside the free spectral range such as Raman scattering and fluorescence from the sample and optics, ambient room light, etc. In order to eliminate these background effects, we use an Amici dispersing prism and a spatial filter as a final bandpass filter. The signal from the PMT is fed to a discriminator and preamplifier, whose output is TTL pulses. The count rate of TTL pulses is proportional to the intensity of light arriving PMT. To maintain linear response, the count rate must be kept below 40 $Kcnts/sec$ for our system. Applying the sawtooth voltage scan to the piezo-transducer, the interferometer scans back and forth linearly. The whole system acts like a high resolution tunable bandpass filter. The TTL pulses are recorded by an *EG&G* multi-channel scaler then stored in a computer. The *EG&G* Ortec multi-channel scaler has 1024 channels and is triggered and synchronized by the tandem controller. In normal operation, sequential scans are accumulated to build up the spectrum until the necessary signal-to-noise ratio is

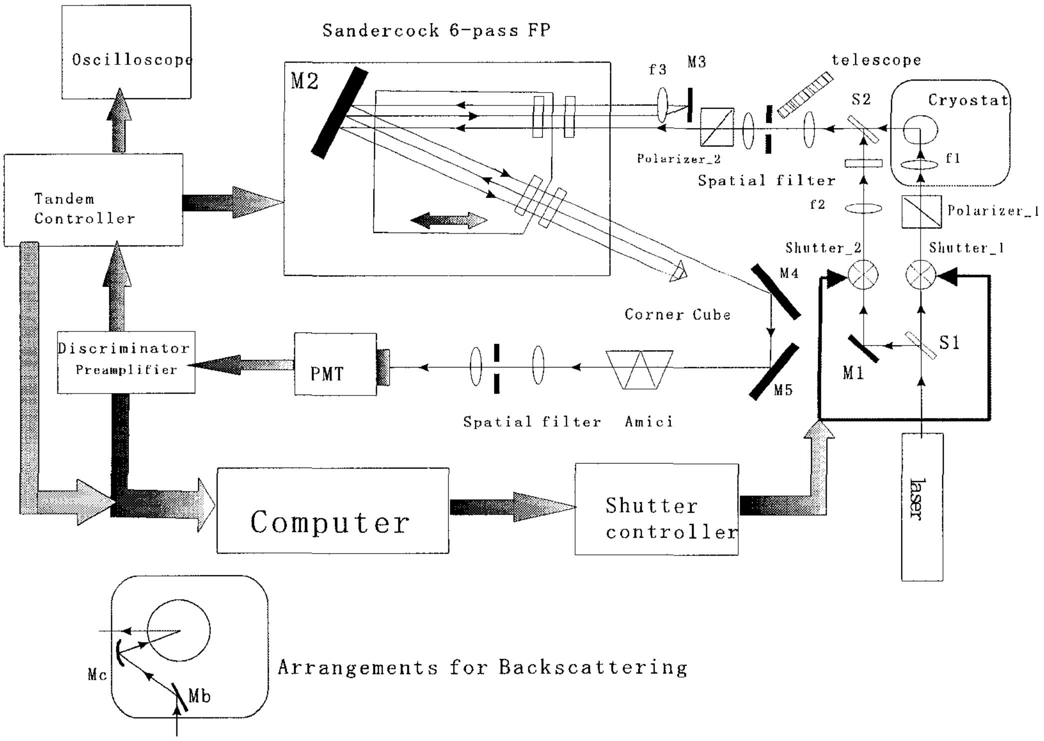

Figure 4-4: Schematic illustration of the 6-pass TFPI Brillouin scattering apparatus.

achieved. The signals are also sent to the tandem controller for feedback purpose and to oscilloscope for display purpose needed during optical alignment.

The whole Brillouin scattering apparatus is mounted on a compressed air floating optical table, in order to decouple the optics from vibration in the surrounding environment. To minimize the influence of the air motion between the FP mirrors and obtain better thermal isolation, a Plexiglas box is used to enclose the entire interferometer. To maintain the high contrast of the multi-pass FP system, masks are placed at the front and back of both FPIs, in front of the coupling mirrors and corner cube and in some other places to eliminate stray reflections from imperfect optical surfaces.

### Working mode of shutters, Frequency Calibration and Spectra-splicing

Two shutters are used in the excitation and reference beams, as shown in Fig.[4-4]. These shutters are controlled by the shutter controller, which is driven by the computer [1] and can function in two different modes. In the first mode, only shutter-1 functions and shutter-2 is always open. As discussed above, a reference beam with stable intensity is crucial for automatic stabilization. So it is necessary to block the scattered light, which is fluctuating, while the system scans through the elastic peak. The two ghosts, weak residues of the nearest transmission maxima, are important in frequency calibration and we also block the scattered light there. Therefore shutter-1 is closed when the interferometer scans through the central peak and ghosts and is open in the rest of time, however shutter-2 is always open during the whole scan. One typical spectrum with shutters working in this mode is shown in Fig.[4-5] (a), where one depolarized 90° spectrum from salol is recorded with mirror separation 10 *mm*. In the frequency regions of the central elastic peak and two ghosts, shown by symbols, the scattered light is blocked.

The direct output of the multi-channel scalar is the intensity as function of channel number. Thus a calibration is needed to map channel number to frequency in order to get the spectrum, namely intensity as a function of frequency. In order to achieve that, first, we find the center of the elastic peak in channel numbers, which is the origin of the frequency axis, by fitting the elastic peak to Lorentzitian lineshape. The ghosts can be modeled by a product of two Lorenzitians with slightly different centers. From this fit, the center of the nearest transmission peaks of the first FPI can be obtained in channel numbers. The mirror separation of the first FPI, therefore the frequency separation between the adjacent orders, is known. Assuming the piezo-transducer scans linearly, we do a linear interpolation between central peak and adjacent peak to map the channel number to frequency.

---

[1] The latest version of the Sandercock tandem controller has incorporated the shutter controlling ability, where a separate shutter controller is not needed.

One obvious shortcoming of the one-shutter mode is that we lose the information contained in the central part of the spectrum, which is usually as wide as the resolution of the instrument ($\sim 0.1$ $GHZ$). Thus contains limited information in usual cases.

However, sometime the central part of the spectrum is important, like the Rytov dip. In these situations, a second mode must be used. In this mode (two-shutter mode), the two shutters open and close alternatively in adjacent scans. In a stabilizing cycle, shutter_1 is closed, shutter_2 is open; the automatic stabilization is active and the recording system is inactive. Thus the system stabilizes itself but records nothing. The next scanning cycle is for measurement. In this cycle, shutter_2 is closed, shutter_1 is open; automatic stabilization is inactive and the recording system is active. Thus the whole spectrum, including the central part, can be recorded, as shown in Fig.[4-5] (b). Due to the lack of an elastic peak and ghosts, calibration can't be done in this spectrum. Instead, we run the system in one-shutter mode just after the spectrum in two-shutter mode is taken, which can be calibrated. This calibration will be used, assuming the system doesn't change between the two measurements.

Usually we only scan the TFPI slightly more than two orders, to keep two "ghosts" in the spectra, so that the scanning linearity of the piezo-transducer can be guaranteed. Thus the measured frequency range, for mirror separation $D$, is roughly from $-C/2D$ to $C/2D$, where $C$ is the speed of light. Thus a small mirror separation leads to a larger frequency range. On the other hand, because the total number of channels in the multi-channel scalar is fixed (1024), the spectra measured with larger mirror separation have finer frequency steps than with small mirror separation, although the frequency range is smaller. Thus in order to maximize both the number of data points and frequency range, we use a splicing approach, shown in Fig.[4-6]. The spectra shown in the upper panel are the depolarized backscattering spectra from salol at 380 $K$ obtained with different mirror separations and with a Raman spectrometer. They were spliced by optimizing the overlapping frequency region by adjusting the amplitude factor. Finally we can get a spectrum covering from 0.4 $GHZ$ to 6000 $GHZ$ by combining three Brillouin and one Raman spectra.

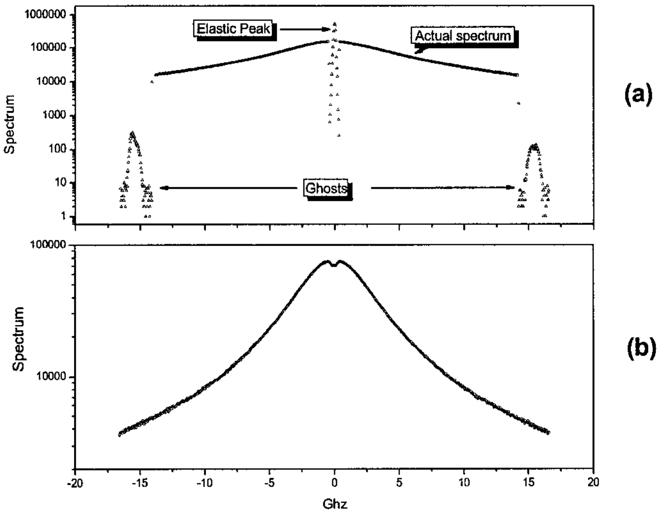

Figure 4-5: Two working modes of shutters. Two $90^0$ depolarized spectra were collected on salol at 380 $K$ with shutters working in different modes: (a) one-shutter mode; (b) two-shutter mode. See text for details.

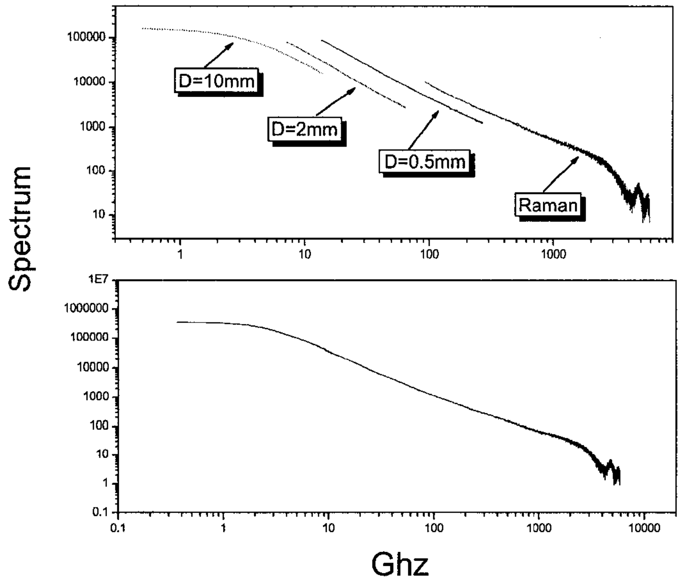

Figure 4-6: Illustration of splicing process, see text for detail.

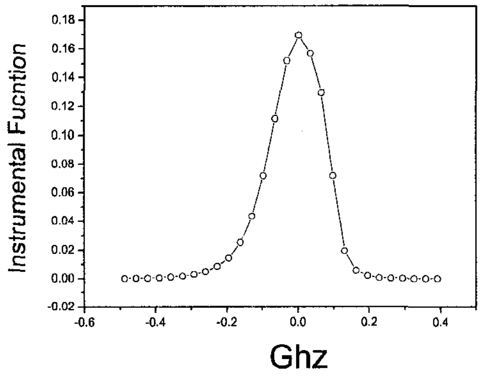

Figure 4-7: Instrumental function of TFPI measured with $D = 10\ mm$ from the scattering light from a metal surface.

**Instrumental function**

With the apparatus described above, we obtain a finesse around 110 at a mirror separation of 10 *mm*, a contrast of $10^{10}$ and a suppression of neighboring interference orders of around 300. A typical instrumental function is shown in Fig.[4-7], which is measured with $D = 10\ mm$ using the scattered light from a metal surface. This instrumental function will be convoluted with the theoretical spectrum for fitting in the next chapter.

### 4.1.2 Raman Spectroscopy

Although Raman Spectroscopy doesn't have as good resolution as a Brillouin setup, it covers a much larger frequency range. The Raman scattering apparatus is shown in Fig.[4-8]. The *Coherent innova 300C* laser operates in single-line multimode with output power of around 300 mW at 4880 Å. The laser beam is focused on the sample inside the cryostat and the scattered light is collected and focused on an intermediate slit which is used to eliminate the strong elastic scattering from the edges of samples.

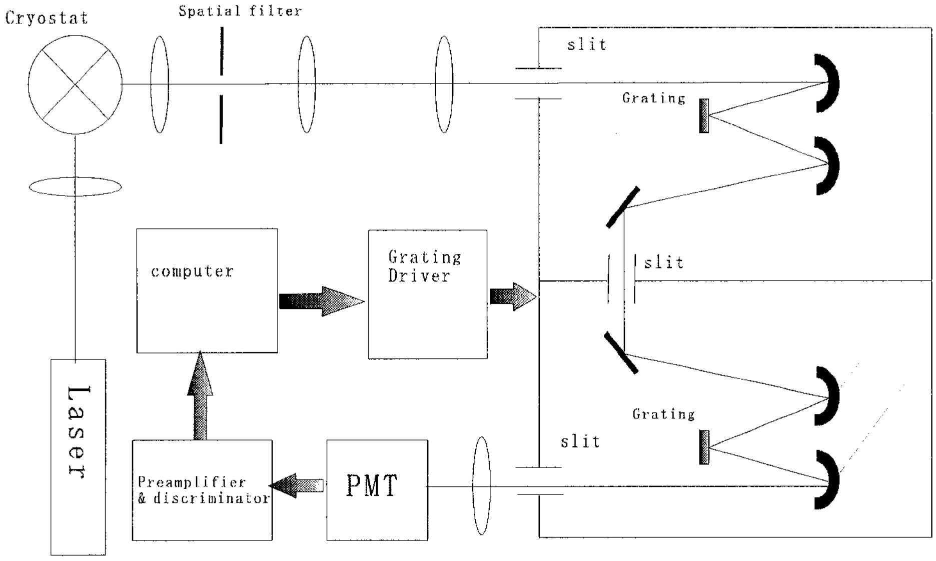

Figure 4-8: Schematic illustration of the Raman scattering aparatus

The collected light is collimated and then refocused on the entrance-slit of a Spex 1401 tandem grating spectrometer. The openings of the three slits in the spectrometer can be adjusted to optimize the throughout and the resolution. The settings usually used are $100\mu m$, $200\mu m$, $400\mu m$. The scattered light is analyzed by the gratings operated in tandem, which are driven by the stepping motor driver. Finally, the light is collected by a PMT. Signal from the PMT is sent to the discriminator/preamplifier, from which the TTL pulses are acquired by a computer equipped with an EG&G Ortec ACE-MCS multi-channel scalar as in the Brillouin setup.

### 4.1.3 Photon Correlation Spectroscopy (PCS)

Photon Correlation Spectroscopy can directly measure the relaxation time near $T_g$, where the linewidth is much too marrow to be measured by a Brillouin spectrometer. In PCS measurements, the normalized correlation function of the scattered light intensity is measured:

$$\mathfrak{C}(t)=\frac{\langle I(0)\,I(t)\rangle}{\langle I(0)\,I(0)\rangle}=\frac{\langle E^{*}(0)\,E(0)\,E^{*}(t)\,E(t)\rangle}{(\langle E^{*}(0)\,E(0)\rangle)^{2}}$$

where $E(t)$ is the electric field amplitude of the scattered light. Supposing the electric field $E(t)$ is a random complex variable with a 2-d Gaussian distribution [1], we will have :

$$\langle E^{*}(0)\,E(0)\,E^{*}(t)\,E(t)\rangle=(\langle E^{*}(0)\,E(0)\rangle)^{2}+(\langle E(0)\,E^{*}(t)\rangle)^{2}$$

Thus theoretically,

$$\mathfrak{C}(t)=1+(C(t))^{2} \tag{4.4}$$

where

$$C(t)=\frac{\langle E(0)\,E^{*}(t)\rangle}{\langle E^{*}(0)\,E(0)\rangle}$$

is the normalized correlation function of the scattered field, reflecting the dielectric fluctuation in the scattering object. However, in practice, we usually collect scattered light from more than one coherence area and Eq.[4.4] becomes:

$$\mathfrak{C}(t)=1+A\,(C(t))^{2} \tag{4.5}$$

where $A$ is a spatial coherence factor depending on the numbers of coherence areas collected [1].

Fig.[4-9] is a schematic diagram of the experimental PCS setup. In our PCS setup, a *Spectra Physics 165 Argon* laser with a single-mode etalon operating at 4880 Å is used as the excitation source. The exciting beam is focused on the sample in the cryostat. The scattered light is first collimated by a cylindrical lens. After a polarizer, the collimated light is collected by the fiber optic detection system. The fiber optic assembly which consists of a micro-collection GRID lens, 1X2 coupler which splits the input fiber optic to provide two outputs and two FC connectors is made by OZ Optics (Carp, Ontario, Canada). The focal length of the GRID lens is about 30 cm. The FC

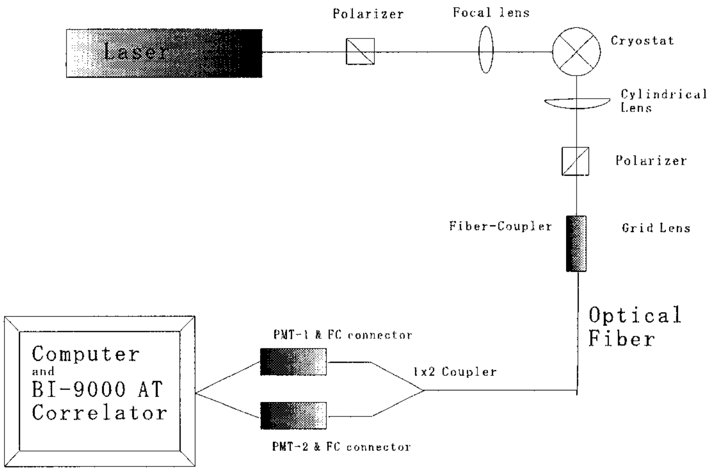

Figure 4-9: Experimental setup for Photon Correlation Spectroscopy

connector sockets are mounted directly on the PMT assemblies, which each contain a PMT, discriminator and preamplifier. The use of fiber optics eliminates the pinholes and lenses used in the traditional PCS apparatus. This fiber optic detection system was tested on polystyrene suspensions. The spatial coherence factor, $A$ in Eq.[4.5], is $A = 0.98$, much closer to the theoretical maximum of 1.0 than what can be achieved with conventional optics. Thus in the PCS data analysis, we will take $A = 1$.

The signal from the PMT assembly is sent to a BI-9000AT digital correlator made by the Brookhaven Instrument Co. (Holtsville, NY). The BI-9000AT has an ISA computer interface and is installed in a personal computer. This correlator is constructed with a semi-logarithmic channel layout configuration with a time range from 0.1 $\mu s$ to 1000 $s$, which is crucial in studying the slow stretched dynamics. An autocorrelation from the signal of a single PMT or a crosscorrelation function from the signals of both PMTs can be constructed by the BI-9000AT. The crosscorrelation mode avoids the after-pulse effect of the PMT when fast processes are studied.

### 4.1.4 Sample Preparation, Cryostat and Temperature Controller

*Salol* samples for our light-scattering experiments were prepared by triple vacuum distillation of stock phenyl salicylate purchased from Sigma Chemical Company. The final distillation was made into cylindrical glass sample cells which were then flame sealed under vacuum. The sample was mounted in a copper housing on the cold finger of an Oxford LN2 cold-finger cryostat with a ITC-4 temperature controller connected to a platinum resistance thermometer attached near the top of the cold finger. Liquid Gallium-Indium alloy was used to provide thermal contact between the sample cell and the bottom of the copper housing. For the PCS experiments, to have more precise temperature readings, a second platinum resistance thermometer was attached to the bottom of the copper housing close to the sample and was monitored with an Omega RTD digital thermometer. The readings obtained with this second thermometer were $\sim 1\ K$ higher than the first thermometer, indicating a small temperature gradient in the cryostat. Brillouin, Raman, and PCS experiments were carried out with the same sample and cryostat to maintain consistency in the temperature measurements.

## 4.2 light-scattering Experiments and Raw Data

*Salol* (phenyl salicylate, $T_m = 316$ K, $T_g = 218$ K) is a fragile molecular glassforming material that supercools easily. It has been studied extensively with a wide range of experimental techniques, so a great deal of information is available in the literature. Experiments in which the depolarized backscattering spectra of salol were compared with predictions of the mode coupling theory (MCT) indicated that $T_C$, the critical temperature of MCT, is $T_C = 256 \pm 5\ K$ [107]. Some of the relevant properties of salol are collected in Table.[**4.1**].

There have been several previous polarized and depolarized Brillouin scattering studies of *Salol*. The evolution of the depolarized (VH) spectrum from a high-

| Formula | $C_{13}H_{10}O_3$ |
|---|---|
| Chemical structure | Fig.[4-10] |
| Molecular weight | 214.21 |
| $T_M$ $(K)$ | 316 |
| $T_B$ $(K)$ | 446 |
| $T_g$ $(K)$ | 218 |
| Density $(gm/cm^3)$ | $\rho = 1.4516 - 8.57 \times 10^{-4} T\,(K)$[99] |
| Refractive Index | $n = 1.718 - 4.321 \times 10^{-4} T\,(K)$[99] |
| Viscosity | Eq.[4.6] [103], [104], [105] |
| Sound Velocity $(m/\sec)$ | $C_o = 2448 - 3.23T\,(K)$[106] |
| $T_C\,(MCT\ temperature)$ | $256 \pm 5$ $K$[107]; $253 \pm 4$ $K$[108]; |
|  | 266 $K$[109]; $250 \pm 5$ $K$[110] |
| $\lambda\,(MCT$ exp$ponent\ parameter)$ | 0.70[107]; 0.73 [108], [110] |

Table 4.1: Properties of salol

temperature doublet to a low-temperature triplet was studied by Fabelinski *et al* [2], [4], [101], Vaucamps *et al* [102], Enright and Stoicheff [99], and Wang and Zhang [16]. The polarized (VV) spectrum was studied by Wang and Zhang [16] and by Dreyfus *et al* [106].

The total depolarized light-scattering cross section of salol was previously measured and compared with the estimated value for dipole-induced-dipole scattering, the major non-rotational contribution to the total intensity [111]. The results indicated that rotational dynamics account for approximately 97% of the total scattering intensity due to its very anisotropic chemical structure shown in Fig.[4-10], justifying the use for salol of the theories discussed in Sec.[**3.3.2**] in which depolarized scattering due to mechanisms other than rotational dynamics are neglected.

The shear viscosity $\eta_s$ of *Salol* was measured by Jantsch [103], Laughlin and Uhlmann [105], and Cukierman *et al* [104] for temperatures between 416 $K$ and 213 $K$. In this temperature range, the viscosity increases from $1.2 \times 10^{-2} P$ to $4.8 \times 10^{12} P$. The combined viscosity data is plotted in Fig.[5-11] together with an extended free-volume fit to Eq.[2.2]: (which gives $\eta_s$ in Poise).

$$\log_{10}(\eta_s) = -2.157 + 123.0/\left\{T - 261.2 + \left[(T - 261.2)^2 + 3.984T\right]^{1/2}\right\} \tag{4.6}$$

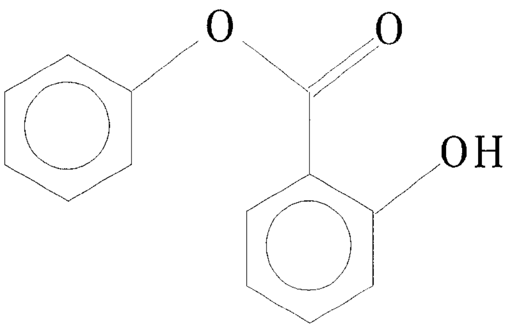

Figure 4-10: Chemical Structure of Salol. ( From [100] )

### 4.2.1 Brillouin and Raman scattering

Three sets of light-scattering spectra have been measured: $173^0$ VH near-backscattering, 90° VH and VV spectra from salol at temperatures: $380\ K, 370\ K, 360\ K, 350\ K, 340\ K, 330\ K, 320\ K, 310\ K, 300\ K, 295\ K, 290\ K, 285\ K, 280\ K, 275\ K$,$270\ K, 265\ K, 260\ K, 250\ K, 240\ K, 230\ K, 220\ K, 210\ K$. In all experiments, the cryostat was allowed to restabilize for at least a half hour, after changing the temperature.

In depolarized backscattering measurements, three mirror separations were used: $10\ mm$, $2\ mm$, $0.5\ mm$, and the shutters worked in the one-shutter mode. To extend the spectra to higher frequencies for analyses, Raman scattering spectra were obtained. Raman spectra were accumulated in $90^o$ HT geometry, taking $\sim$ 30 minutes per run. (At frequencies in the Raman range, depolarized 90° and depolarized backscattering spectra are indistinguishable). The combined interferometric + Raman VH backscattering intensity spectra are shown in Fig.[4-11]. However, the susceptibility spectra $\chi''(\omega)$, which are related to the intensity spectra $I(\omega)$ through the fluctuation-dissipation theorem [63], [89]:

$$\chi''(\omega) = \left( \frac{1 - \exp\left(-\frac{\hbar\omega}{k_B T}\right)}{2\hbar} \right) I(\omega) \tag{4.7}$$

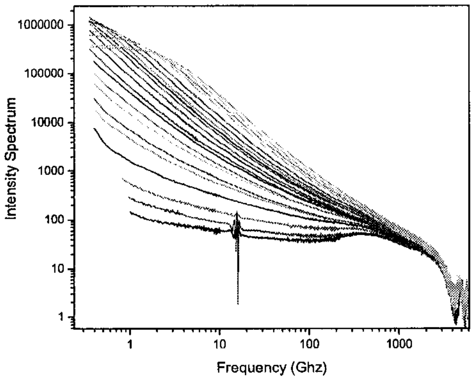

Figure 4-11: Spliced backscattering depolarized spectra of salol. From top to bottom: 380 $K$, 370 $K$, 360 $K$, 350 $K$, 340 $K$, 330 $K$, 320 $K$, 310 $K$, 300 $K$, 295 $K$, 290 $K$, 285 $K$, 280 $K$, 275 $K$, 270 $K$, 265 $K$, 260 $K$, 250 $K$, 240 $K$, 230 $K$, 220 $K$, 210 $K$. The breaks in low temperature spectra are due to the leakage of polarized scattering.

show more identifiable features than intensity spectra. In our frequency window, $\omega/2\pi < 200\ GHZ$, $\hbar\omega \ll kT$, so that Eq.[4.7] reduces to its classical form:

$$\chi''(\omega) = \frac{\omega}{2k_BT} I(\omega) \ . \tag{4.8}$$

The complete set of susceptibility spectra obtained from the data of Fig.[4-11] with Eq.[4.8] is shown in Fig.[4-12].

In the 90° VH measurements, two mirror separations were used: 10 *mm* and 2 *mm*, and the shutters worked in the two-shutter mode. The spectra are shown in Fig.[3-5]. For the 90° VV spectra shown in Fig.[4-13], two mirror separations were used: 10 *mm* and 2 *mm*, and the shutters worked in the one-shutter mode.

### 4.2.2 Photon Correlation Spectroscopy

Photon correlation spectra were obtained at temperatures of 221.8 $K$, 224.4 $K$, 226.4 $K$, 231.3 $K$, 236.1 $K$, 241.3 $K$, and 246.1 $K$ with a scattering angle of 90°. 488

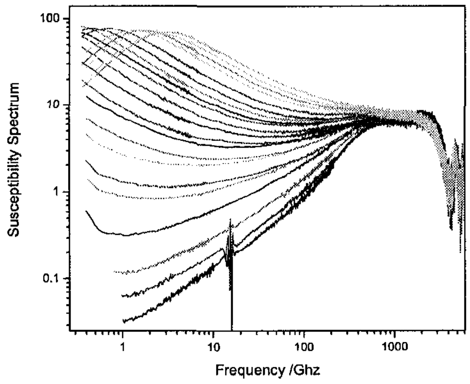

Figure 4-12: Backscattering VH susceptibility spectra of salol. From top to bottom: 380 $K$, 370 $K$, 360 $K$, 350 $K$, 340 $K$, 330 $K$, 320 $K$, 310 $K$, 300 $K$, 295 $K$, 290 $K$, 285 $K$, 280 $K$, 275 $K$, 270 $K$, 265 $K$, 260 $K$, 250 $K$, 240 $K$, 230 $K$, 220 $K$, 210 $K$. The breaks in low temperature spectra are due to the leakage of VV scattering.

Figure 4-13: Spliced raw $90^0$ polarized spectra of salol, from top to bottom: 380 $K$, 370 $K$, 360 $K$, 350 $K$, 340 $K$, 330 $K$, 320 $K$, 310 $K$, 290 $K$, 280 $K$, 270 $K$, 260 $K$, 240 $K$, 220 $K$, 210 $K$. (The spectra have been shifted along $Y$ axis for clarity.)

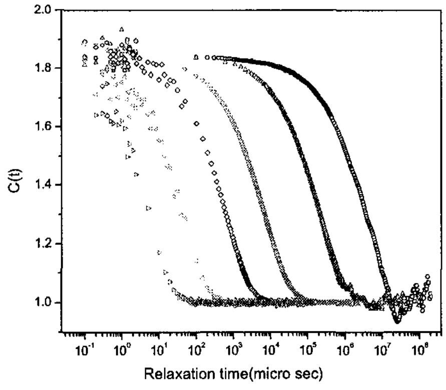

Figure 4-14: Depolarized photon correlation spectra of salol (scattering light intensity autocorrelation ). From right to left: 221.8, 226.4, 231.4, 236.1, 241.3 and 246 K.

*nm* incident laser light from a *Spectra Physics 165 Argon* laser provided 20mW of single-mode power at the sample. The incident light was vertically polarized, and horizontal polarization was selected for the scattered light (VH). Correlation data was accumulated for 5 to 10 minutes with count rates of 5 to 10 $Kcts/sec$. At the lowest temperature, 20 minute runs were necessary. The normalized correlation functions $C(t)$, are shown with in Fig.[4-14].

# Chapter 5

# Data Analysis and Results

After reviewing the Pick-Franosch theory and laying out the experimental details, in this Chapter, we will show our data analysis. In the analysis, we focus mainly on two issues: first, whether the Pick-Franosch theory can provide both reasonable fits and fitting parameters to both VH and VV spectra over the whole temperature range from above $T_m$ to below $T_g$; second, whether the signature of RT coupling, predicted by the theory, can be identified clearly in the VV spectrum.

In order to make our analysis sensible, it is important to limit the number of free fitting parameters. First, in Chapter **3**, we have simplified the spectral expressions for fitting by assuming $\Gamma(\omega)/\mu(\omega)$ is frequency independent. Second, in the fittings, we used as much information from the literature as possible, including the refractive index, mass density, isothermal sound speed, and static viscosity, given in Table.[**4.1**]. Third, as shown in Fig.[5-1], we divided the whole fitting procedure into four sequential steps. In the first step, we analyzed PCS data and the $\alpha$ peaks in the VH backscattering susceptibility spectra to obtain the rotational relaxation time $\tau_R(T)$. The resulting $\tau_R(T)$ values were used to fit the VH backscattering spectrum with the hybrid function,. In the third step, we fit the VH 90° spectra with the backscattering parameters fixed from the second step, and determined the coupling constant $\Lambda$ and shear viscosity memory function $\eta_s(\omega)$. The VV 90° spectra were analyzed in the

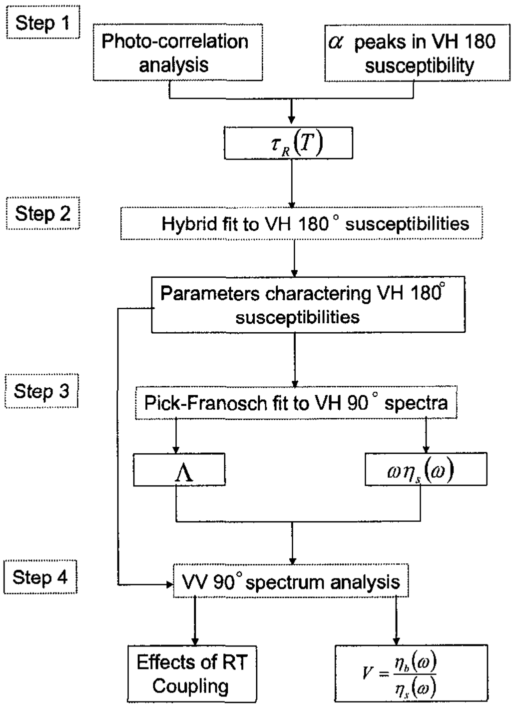

Figure 5-1: Flow diagram of 4-step fitting procedure.

last step to pinpoint the effects of RT Coupling , with all the parameters obtained in the previous stages fixed, namely the backscattering parameters, coupling constant $\Lambda$ and shear viscosity memory function $\eta_s(\omega)$. With this 4-step strategy, we managed to limit the number of free fitting parameters to no more than 4, and to 3 in most cases.

## 5.1 The Rotational Relaxation Time $\tau_R(T)$

The temperature evolution of the orientation relaxation time $\tau_R(T)$ is an important piece of information and can be obtained by combining the PCS data, from 3 $K$ to 25 $K$ above $T_g$, and the $\alpha$ peaks in VH backscattering susceptibility spectra, from

310 $K$ to 380 $K$. These two techniques measure the pure rotational dynamics, in the time and frequency domain respectively.

The normalized autocorrelation function of the scattered field, $C(t)$, can be modelled as a KWW function:

$$C(t) = f_K \exp\left(-\left(t/\tau_K\right)^{\beta_K}\right) .$$

Thus, the measured intensity autocorrelation function, Eq.[4.5], is:

$$\mathfrak{C}(t) = 1 + A_1 \exp\left(-2\left(t/\tau_K\right)^{\beta_K}\right) \tag{5.1}$$

where the relaxation time $\tau_K$, stretching exponent $\beta_K$, and $A_1 = \left(f_K\right)^2$, were free fitting parameters in the fits. We fit the correlation functions to Eq.[5.1]; the fits are shown in Fig.[5-2] together with the experimental $\mathfrak{C}(t)$ data. The $\tau_R$s are plotted in Fig.[5-5] as circles. The $\beta_K$ values and amplitudes are nearly constant: $\beta_K \sim 0.635$ and $A_1 \sim 0.835$, are plotted as functions of temperature in Fig.[5-3]. The fact that $f_K = \sqrt{A_1} \sim 0.91$ is less than *one* indicates that there are fast relaxation processes outside of the time window of the PCS experiment, and it is the $\alpha$ relaxation in the long time region that we have measured.

The VH backscattering spectrum measures the pure rotational dynamics from which the spectral density is, according to Eq.[3.67],

$$I_{VH}^{B}(\omega) = \frac{I_0}{\omega} \mathcal{I}mR(\omega)$$

where $\frac{1}{\omega}\mathcal{I}mR(\omega)$ is the normalized autocorrelation function of $Q_{xy}\left(\vec{q},\omega\right)$, shown in Eq.[3.59], and can be described by the hybrid function in the frequency range below the microscopic peak ($\sim 10^3 GHZ$):

$$\frac{1}{\omega}R(\omega) = \frac{1}{\omega}R_0 \left\{\left[1 - \left(1 + i\omega\tau_R\right)^{-\beta_R}\right] + p_R\left[i\omega\left(\tau_R^{-1} + i\omega\right)^{a_R - 1}\right]\right\}$$

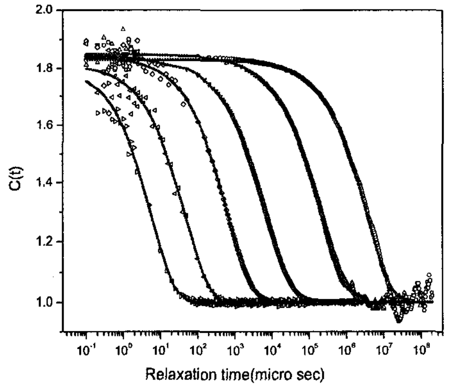

Figure 5-2: Depolarized photon correlation spectra of salol (scattered light intensity autocorrelation ). Scatters are the experimental data and lines are KWW fits. From right to left: 221.8, 226.4, 231.4, 236.1, 241.3 and 246 K.

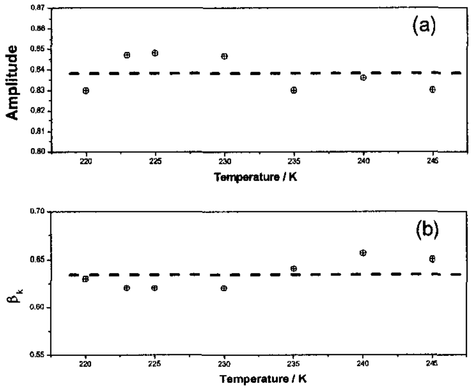

Figure 5-3: Fitting parameters from PCS plotted as a function of temperature. (a) amplitude of $\alpha$ relaxation $A_1$; (b) stretching exponent $\beta_k$.

The susceptibility spectrum, related to the intensity spectrum by Eq.[4.8], in our frequency range, reads:

$$\begin{array}{l} \chi^B_{VH}(\omega) = \frac{\omega}{2k_BT} I^B_{VH}(\omega) \\ = A_{cd}\mathcal{I}m\left\{[1-(1+i\omega\tau_R)^{-\beta_R}] + p_R[i\omega(\tau_R^{-1}+i\omega)^{a_R-1}]\right\} \end{array} . \tag{5.2}$$

where $p_R$ is the ratio of the critical contribution to the C.D. contribution, and $R_0$ and $k_BT$ are absorbed into the amplitude $A_{cd}$. In the $\alpha$ peak region, only the CD part of Eq.[5.2] contributes:

$$\chi^B_{VH}(\omega) = A\mathcal{I}m\left\{[1-(1+i\omega\tau_R)^{-\beta_R}]\right\}. \tag{5.3}$$

The $\alpha$ region of the susceptibility spectra $\chi^B_{VH}(\omega)$ are shown in Fig.[5-4], for temperatures between 310 $K$ and 380 $K$ where they exhibit a visible $\alpha$ peak. These $\alpha$ peaks were fit to Eq.[5.3]. $A_{cd}$, $\tau_R$ and $\beta_R$ were free fitting parameters. The resulting $\beta_R$ values, which slightly depend on the selected fitting range, vary between 0.77 and 0.80. The resulting $\tau_R$ values for $T$ between 310 $K$ and 380 $K$ are included in Fig.[5-5] as squares.

In order to bridge the gap between PCS and VH backscattering data, we carried out a free-volume fit, Eq.[2.2], to the $\tau_R(T)$, which is shown in Fig.[5-5]:

$$\log_{10}(\tau_R) = -11.05 + 234.81/\left\{T - 248.44 + \left[(T-248.44)^2 + 6.185T\right]^{1/2}\right\} \tag{5.4}$$

where $\tau_R$ is in seconds. With this fit, we estimate $T_g \simeq 219.8K$. The $\tau_R(T)$ values obtained from this fit were used to fix the $\tau_R(T)$ values in $R(\omega)$ for the temperatures from 250 $K$ to 310 $K$.

Since we have both $\tau_R(T)$, Eq.[5.4], and $\eta_s(T)$, Eq.[4.6], the Deybe equation, Eq.[2.5], can be tested [53], [58]. In Fig.[5-6] $\eta_s$ in $10^{-2}$ Poise is plotted together with $\tau_R \cdot T$ in $10^{-2} ns \cdot K$, which was scaled by 80 to match $\eta_s$ at high temperatures, as

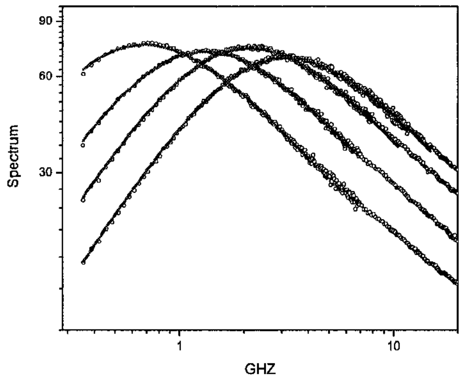

Figure 5-4: Cole-Davison fits to the $\alpha$ peak of VH backscattering susceptibility spectra. Points are experimental data and the lines are fits. From left to right: 320 $K$, 340 $K$, 360 $K$, and 380 $K$,.

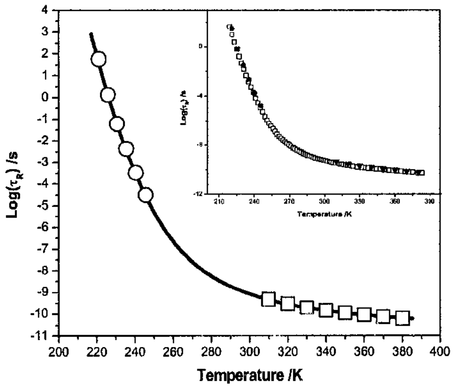

Figure 5-5: Temperature evolution of the rotational relaxation time, $\tau_R$, in Salol. Circles are fitting results from VH backscattering spectra; squares are fitting results from PCS, and the line is the free-volume fit. In the inset, $\tau_R$ from PCS and backscattering analyses are plotted together with $\tau_{diel}$ from [113].

$\beta_s$, and $\tau_s$. Fits were carried out using three different fitting ranges ($1-5$, $1-10$, and $1-20$ $GHZ$) and two different weighting functions: $S$ $[wt(i) = y_i^{-1/2}]$ and $U$ $[wt(i) = 1]$. The resulting fits for each $T$ were nearly indistinguishable, although there was slight scatter in the resulting fit parameters. Fig.[5-12] shows one fit for each temperature from 280 $K$ to 250 $K$. The (averaged) values of the parameters $I_0$, $\Lambda$, $\beta_s$, and $\tau_s$ are given in Part B of Table.[**5.2**]. For $T \leq 250$ $K$, the fits showed strong anticorrelation between $I_0$ and $\Lambda$. For $T > 280$ $K$ where the spectrum is dominated by the rotational component $R(\omega)$, the fits obtained through this 4-parameter strategy are less successful.

In the transition region, the translation-rotation coupling constant $\Lambda$ was found to increase with decreasing temperature, an effect which is presumably due to the increasing density. We note that a similar temperature dependence for $\Lambda$ was observed by Dreyfus et al in $ZnCl_2$ [118] and metatoluidine [19]. $\beta_s$ was found to be smaller than $\beta_R$ and decreases as the temperature decreases. The small $\beta_s$, indicating very nonexponential behavior of $\eta_s(\omega)$, has also been found in dynamic viscosity measurements [58], where $\beta_s \sim 0.3$ was found.

### 5.3.3 The low-temperature region

For temperatures below $\sim$ 250 K, the $I_{VH}^{90}(\omega)$ spectra exhibit narrow transverse Brillouin components superimposed on a slowly varying background from the rotational $R(\omega)$ term. The main features of the spectrum are (1) the amplitude of the Brillouin line relative to the rotational background, (2) the frequency $\omega_B$ of the Brillouin line, and (3) the Brillouin linewidth $\Delta\omega_B$. These spectra can be fit quite well by damped harmonic oscillator functions, and the fits show that at the lowest temperatures the observed linewidth is predominantly instrumental.

Since so little information is contained in these low-temperature spectra, the number of free fitting parameters must be restricted. We examined the effect of changing the parameters in Eq.[5.9] for low temperatures, which showed that (a) $\Lambda$: increasing

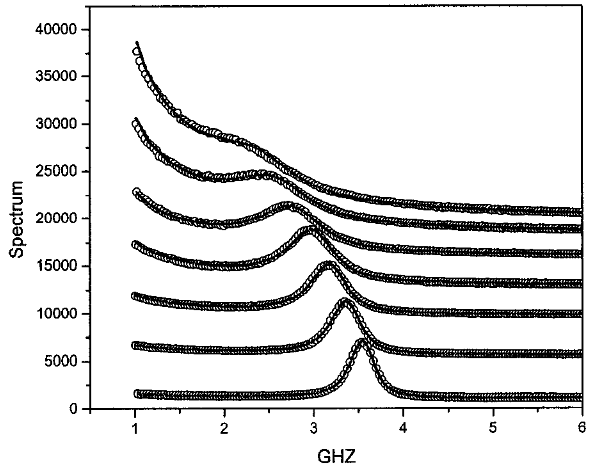

Figure 5-12: Pick-Franosch theory fits to the VH $90^0$ spectra in the crossover region. From top to bottom: 280 $K$, 275 $K$, 270 $K$, 265 $K$, 260 $K$, 255 $K$ and 250 $K$. (The spectra have been shifted along $Y$ axis for clarity.)

| T($K$) | $\eta_s(Pa \cdot s)$ | $q^2/\rho$ $10^9 m/kg$ | $\Lambda$ $10^7 Pa$ | | | $I_0$ | $\chi^2$ |
|---|---|---|---|---|---|---|---|
| **A. High-temperture** | | | $\Lambda$ | $\eta_s/Pa \cdot s$ | $\delta$ | $I_0$ | $\chi^2$ |
| 380 | 2.23E-3 | 639.6 | 1.56 | 2.65E-3 | 6.11E+3 | 1.09E+6 | 3.4 |
| 370 | 2.46E-3 | 638.3 | 1.46 | 2.67E-3 | 1.50E+4 | 1.07E+6 | 7.9 |
| 360 | 2.78E-3 | 637.1 | 1.42 | 3.06E-3 | 1.65E+4 | 1.19E+6 | 8.2 |
| 350 | 3.22E-3 | 635.8 | 1.63 | 4.30E-3 | 1.38E+4 | 1.13E+6 | 2.4 |
| **B. Transition** | | | $\Lambda$ | $\beta_s$ | $\tau_s$ $(ns)$ | $I_0$ | $\chi^2$ |
| 280 | 9.91E-2 | 627.9 | 1.64 | 0.49 | 0.293 | 1.47E+6 | 5.8 |
| 275 | 2.09E-1 | 627.4 | 1.82 | 0.30 | 0.750 | 1.37E+6 | 3.5 |
| 270 | 5.24E-1 | 626.9 | 2.03 | 0.23 | 2.13 | 1.19E+6 | 1.1 |
| 265 | 1.63 | 626.4 | 2.22 | 0.21 | 6.91 | 1.20E+6 | 2.3 |
| 260 | 6.54 | 625.9 | 2.60 | 0.19 | 28.6 | 8.28E+5 | 1.4 |
| 255 | 3.35E+1 | 625.4 | 2.60 | 0.18 | 157.0 | 8.22E+5 | 2.2 |
| 250 | 2.30E+2 | 624.9 | 4.90 | 0.14 | 1.10E+3 | 4.14E+5 | 1.2 |

Table 5.2: Parameters from Pick-Franosch fits to 90° VH salol Spectra. $\eta_s$ in the second column and $q^2/\rho$ in the third column were taken from literature values.

$\Lambda$ increases the amplitude of the Brillouin peak (since it appears in the numerator of $R_1(\omega)$) and also slightly decreases $\omega_B$ because of the negative term proportional to $\Lambda$ in the denominator. $\Lambda$ couples strongly to $I_0$ in this temperature region. (b) $p_s$: increasing $p_s$ primarily increases the linewidth $\Delta\omega_B$ while also slightly increasing $\omega_B$. (c) $\tau_s$: If $\beta_s$ is fixed, then increasing $\tau_s$ strongly increases the Brillouin frequency $\omega_B$ while also increasing the linewidth $\Delta\omega_B$.

The choice of "fixed" and "free" parameters is obviously arbitrary. If the constraint $p_s = p_R$ is maintained, then at temperatures below 250K the theoretical linewidths are too small. To obtain reasonable fits, we can either let $p_s$ vary independently, or else we can maintain the $p_s = p_R$ constraint and introduce an additional damping constant $\gamma_0$ as is frequently done in analyzing $I_{VV}$ Brillouin spectra. We analyzed the Spectra for 210, 220, 230, and 240 $K$ using both of these approaches.

1. $p_s$ free: For these fits, the parameters of $R(\omega)$ were fixed at the values found from the VH backscattering spectra. The value of $I_0$ was fixed by plotting the full VH 90° spectrum and the rotational part $\frac{I_0}{\omega}\,\mathrm{Im}\,R(\omega)$, and adjusting $I_0$ so that the rotational part $\frac{I_0}{\omega}\,\mathrm{Im}\,R(\omega)$ coincides with the data in the frequency region above the Brillouin peak where only the rotational part survives. $\beta_s$ was arbitrarily fixed at 0.15. This left three free fitting parameters: $\Lambda, \tau_s$, and $p_s$. The resulting fits are shown in Fig.[5-13]. The corresponding fit parameters are shown in Part A1 of Table.[**5.2**].

2. $p_s = p_R$ : The second set of low-temperature fits was carried out with the constraint $p_s = p_R$. An additional "normal" damping $\gamma_0$ was introduced by adding a damping term $i\omega\gamma_0$ to $\omega\eta_s(\omega)$ in the denominator of Eq.[5.9]. For these low-temperature spectra it was not possible to obtain good fits with the p values in Table.[**5.1**]. A reasonable modification was found to be $p_s = p_R$ fixed at one-half the values in the Table. These values are shown in Table.[**5.2**] in the last column of Part A2. In the fits, we again fixed $I_0$ by visual scaling. $\beta_s$ was arbitrarily fixed at 0.15. This left three free fitting parameters: $\Lambda, \tau_s$, and $\gamma_0$. The resulting values of $\Lambda$ and $\tau_s$ are shown in Part A2 of Table.[**5.2**]. These fits show that, since so little information is contained in the low-temperature spectra, the parameters obtained have considerable

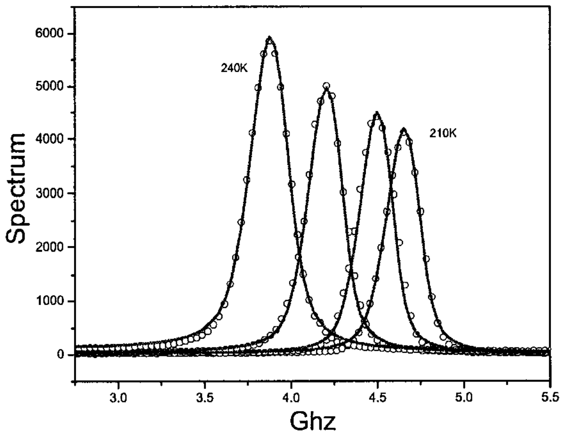

Figure 5-13: Pick-Franosch theory fits [$p_s$ free] to the low temperature VH $90^0$ spectra. From top to bottom: 240 $K$, 230 $K$, 220 $K$ and 210 $K$.

uncertainties.

### 5.3.4 The interpolation region

$I^{90}_{VH}(\omega)$ spectra for the temperature range $285 \leq T \leq 340K$ are shown in Fig.[5-15]. At the highest temperatures in this range there is a slight residue of the high-temperature Rytov dip at $\omega = 0$. At the lowest temperature a slight bulge in the wings signals the emergence of the TA mode. For these eight spectra, the high-temperature approximation used for $T \geq 350K$, where viscoelasticity was ignored is no longer justified, while the spectra lack sufficient structure to permit use of the four-parameter fitting procedure used for $250 \leq T \leq 280K$. We therefore arbitrarily fixed the remaining parameters, except for $I_0$, by interpolation. The R-T coupling constant $\Lambda$ has essentially the same value at $T = 350$ $K$ (1.63) and 280 $K$ (1.64); we therefore fixed $\Lambda = 1.63$ for this range. For $\beta_R$ and $\tau_R$, we scaled $\beta_R$ and $\tau_R$ to overlap $\beta_s$ and $\tau_s$ for $T < 280$ $K$, with both plotted as functions of temperature, and took the scaled $\beta_R$ and $\tau_R$ as $\beta_s$ and $\tau_s$ above 280 $K$. This procedure for $\tau_s$ is shown

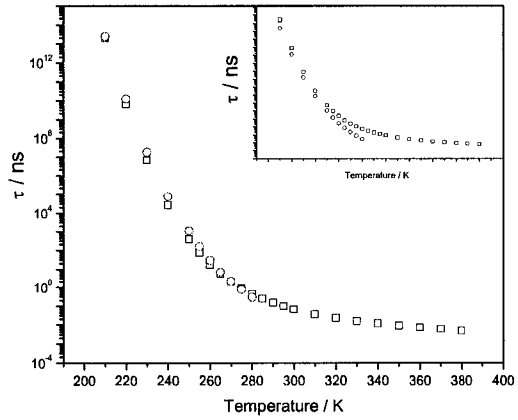

Figure 5-14: The temperature evolution of rotational relaxation time $\tau_R$ (square) from Table.[**5.1**] and relaxation time for shear viscosity $\tau_s$ (circle) from Table. [**5.2**] and Table.[**5.3**]. In the main frame, $\tau_R$ are scaled by a factor of 16.8 to match $\tau_s$. And we take the scaled $\tau_R$ values above 280 $K$ as $\tau_s$ at corresponding temperatures. The unscaled $\tau_R$ and $\tau_s$ are shown in the inset.

in Fig.[5-14], where $\tau_R$ is scaled by a factor of $\sim$ 16.8 to match $\tau_s$ from 280 $K$ to 210 $K$, where the relaxation time increases by 12 orders. The resulting values of the interpolated $\Lambda, \beta_s$ and $\tau_s$ are given in Part B of Table.[**5.3**]. We then fit the spectra to Eq.[5.9] by varying $I_0$ only. The resulting fits are shown in Fig.[5-15] as solid lines. The fits indicate that the parameters obtained by our interpolation process provide a reasonable description of the data.

We have therefore obtained good fits to the salol $I_{VH}^{90}(\omega)$ spectra over the complete temperature range from 210 $K$ to 380 $K$ and will now turn to the VV 90° spectra analysis.

| T$(K)$ | $\eta_s(Pa \cdot s)$ | $q^2/\rho$ $10^9 m/kg$ | $\Lambda$ $10^7 Pa$ | | | $I_0$ | |
|---|---|---|---|---|---|---|---|
| **A1. Low-temp** | | | $\Lambda$ | $\beta_s^*$ | $\tau_s$ $(ns)$ | $I_0^*$ | $p_s$ |
| 240 | 2.47E+4 | 623.9 | 12.6 | 0.15 | 7.44E+4 | 1.4E+5 | 1.53E-2 |
| 230 | 7.35E+6 | 623.0 | 19.1 | 0.15 | 1.78E+7 | 6.0E+4 | 1.53E-2 |
| 220 | 5.55E+9 | 622.0 | 21.6 | 0.15 | 1.21E+10 | 7.0E+4 | 8.51E-3 |
| 210 | 1.04E13 | 621.1 | 17.2 | 0.15 | 2.49E+13 | 9.0E+4 | 2.12E-3 |
| **A2. Low-temp** | | | $\Lambda$ | $\beta_s^*$ | $\tau_s$ $(ns)$ | $I_0^*$ | $p_s = p_R$ |
| 240 | 2.47E+4 | 623.9 | 7.7 | 0.15 | 9.15E+4 | 2.50E+5 | 1.50E-3 |
| 230 | 7.35E+6 | 623.0 | 13.8 | 0.15 | 2.04E+7 | 1.00E+5 | 1.10E-3 |
| 220 | 5.55E+9 | 622.0 | 17.7 | 0.15 | 1.32E+10 | 1.00E+5 | 6.00E-4 |
| 210 | 1.04E13 | 621.1 | 16.9 | 0.15 | 3.77E+13 | 3.00E+5 | 1.40E-4 |
| **B. interpltn** | | | $\Lambda^*$ | $\beta_s^*$ | $\tau_s^*$ $(ns)$ | $I_0$ | $\chi^2$ |
| 340 | 3.85E-3 | 634.6 | 1.63 | 0.400 | 8.68E-3 | 1.17E+6 | 0.89 |
| 330 | 4.81E-3 | 633.4 | 1.63 | 0.390 | 1.18E-2 | 9.36E+5 | 2.0 |
| 320 | 6.41E-3 | 632.3 | 1.63 | 0.380 | 1.72E-2 | 1.08E+6 | 3.4 |
| 310 | 9.38E-3 | 631.1 | 1.63 | 0.375 | 2.76E-2 | 1.21E+6 | 3.5 |
| 300 | 1.58E-2 | 630.0 | 1.63 | 0.370 | 5.08E-2 | 1.14E+6 | 16 |
| 295 | 2.21E-2 | 629.5 | 1.63 | 0.360 | 7.37E-2 | 1.16E+6 | 15 |
| 290 | 3.31E-2 | 628.9 | 1.63 | 0.355 | 1.14E-1 | 1.29E+6 | 24 |
| 285 | 5.42E-2 | 628.4 | 1.63 | 0.350 | 1.88E-1 | 1.29E+6 | 8.5 |

Table 5.3: Parameters from Pick-Franosch fit to 90° VH salol Spectra. $\eta_s$ in the second column and $q^2/\rho$ in the third column were taken from literature. The numbers in columns with * were fixed by interpolation.

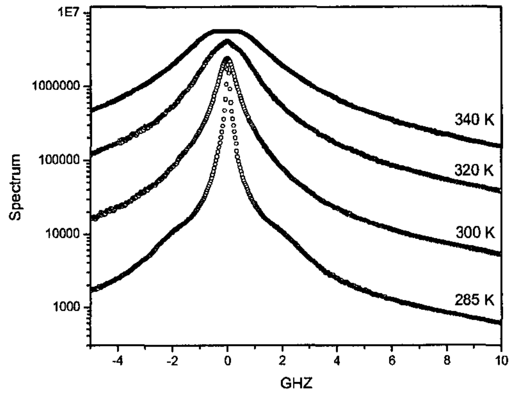

Figure 5-15: Pick-Franosch theory fits to the VH $90^0$ spectra in the interpolation region. From top to bottom: 340 $K$, 320 $K$, 300 $K$ and 285 $K$. (The spectra have been shifted along $Y$ axis for clarity.)

## 5.4 VV 90° Spectra

As discussed in Sec.[**3.3.2**], the VV 90° spectrum, Eq.[3.68], contains two terms. The first term, which is $q$-independent, is the pure rotational contribution and the background of the VV 90° spectrum. On top of the background, there is a second $q$-dependent term that contains most of the interesting information. The effect of RT coupling in the VV spectrum, the difference between full Pick-Franosch theory, Eq.[3.55], and the density-fluctuation-only model, Eq.[3.62], also lies in this second $q$-dependent term.

The VV 90° spectrum and the scaled VH backscattering spectrum at 350 $K$ are shown in Fig.[5-16] (a) in a log-log plot and in Fig.[5-16] (b) in a linear-log plot. The VH backscattering spectrum is scaled to match the VV 90° spectrum at high frequencies (30 – 50 $GHZ$), where the second $q$-dependent term dies out:

$$I_{VV}(\omega)_{(\omega>>\omega_B)} = \frac{I_0}{\omega}\mathcal{I}m\left[\frac{4}{3}R(\omega)\right] \tag{5.12}$$

where $\omega_B$ is the position of the Brillouin peak. Numerical subtraction of the two spectra yields the difference spectrum shown in Fig.[5-16] (c), which is negative in the low frequency range and essentially zero above 20 $GHZ$. Thus the obtained $q$-dependent difference spectrum can be analyzed, according to the Pick-Franosch theory, by the following expression, as seen from Eq.[3.68]:

$$I_{dif}(\omega) = \frac{I_0}{\omega}\mathcal{I}m\left\{\frac{q^2}{\rho}\Lambda\left[S+\frac{2}{3}R(\omega)\right]^2 P_L(\omega)\right\} \tag{5.13}$$

where:

$$P_L(\omega) = \left\{\omega^2-\omega_o^2-i\omega\Gamma_0-\frac{q^2}{\rho}\left[V\omega\eta_s(\omega)-\frac{4}{3}\Lambda\frac{R^2(\omega)}{1-R(\omega)}\right]\right\}^{-1} \tag{5.14}$$

and $\omega_o = qC_0$ is the 'bare' frequency shift due to the isothermal sound response and $\Gamma_0$ is the "regular" sound attenuation coefficient. If RT coupling is ignored, according to Eq.[3.62], we have

$$I^d_{dif}(\omega) = \frac{A}{\omega}\mathcal{I}m[P^d_L(\omega)] \tag{5.15}$$

$$P^d_L(\omega) = \left[\omega^2-\omega_o^2-i\omega\Gamma_0-\frac{q^2}{\rho}V\omega\eta_s(\omega)\right]^{-1} \tag{5.16}$$

where $A = Ia^2q^2C_0^2\left\langle|\delta\rho(\vec{q},0)|^2\right\rangle$. We will call Eqs.[5.15] and [5.16] the density-fluctuation-only model.

In this section, we analyze the difference spectra obtained by the procedure above, which are VV spectra with the rotational background removed. First, we characterize the difference spectra with a damped oscillator model, from which we can get the position and linewidth of the Brillouin peak. Before proceeding with the detailed fittings, we fix two parameter: $I_0$ and $\Gamma_0$. Finally, in the last two subsections, we will carry out the density-fluctuation-only and the Pick-Franosch fits to the difference spectra $I_{dif}(\omega)$ in order to evaluate the changes the RT coupling causes.

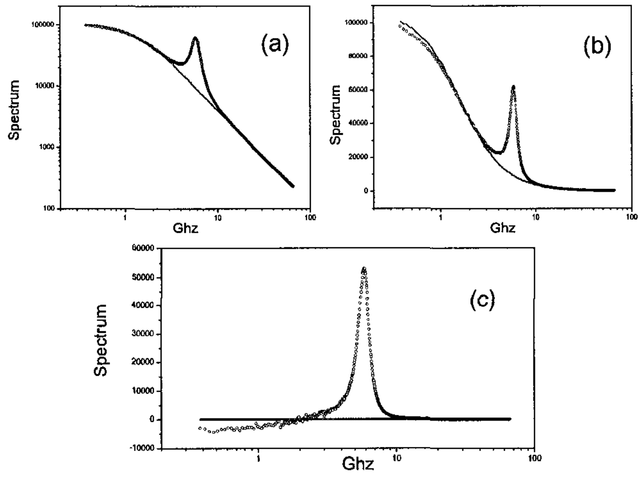

Figure 5-16: Comparation of VV $90^0$ spectrum and VH backscattering spectrum from *Salol* at 350 *K*. VH backscattering spectrum is scaled to overlap VV $90^0$ spectrum from 30 to 50 *GHZ*. (a) two spectra in log-log scale; (b) two spectra in linear-log scale; (c) difference spectrum.

### 5.4.1 Damped oscillator fitting

The difference spectrum around the Brillouin peak can be approximately fit by a damped harmonic oscillator function, from which the position and linewidth of the Brillouin peak can be obtained. The damped harmonic oscillator function can be expressed as:

$$I_{DO}(\omega) = \frac{I_0}{\omega}\mathcal{I}m\left\{(\omega^2 - \omega_B^2 - i\omega\Gamma_B)^{-1}\right\} \tag{5.17}$$

where $I_0$, $\omega_B$ and $\Gamma_B$ were treated as free fitting parameters. The values obtained for $\omega_B$ and $\Gamma_B$ are given in Table.[**5.4**] and plotted as functions of temperature in Fig.[5-17](a) and (b). As *Salol* is cooled from above the melting temperature $T_m$ down to the glass transition temperature $T_g$, the position of the Brillouin peak $\omega_B$ moves monotonically to higher frequencies, see Fig.[5-17] (b), while the width of the Brillouin peak $\Gamma_B$ first increases, and reaches a maximum at around 310 $K$, then decreases again, see Fig.[5-17] (a). The relaxation time $\tau_L$, appropriate for the longitudinal viscosity, can be estimated at the maximum linewidth, where $\omega_B\tau_L \sim 1$. This gives $\tau_L = 0.0224\ ns$ at 310 $K$, which is consistent with $\tau_s$ from the VH analysis: $\tau_s = 0.0276\ ns$.

At high temperatures well above $T_m$, where no memory effect exists, $\omega_B$ should be equal to $\omega_\circ = qC_0$, which can be calculated from the refractive index and isothermal sound speed. Calculated $\omega_\circ = qC_0$ values are plotted as a dash line in Fig.[5-17] (b) and differ from $\omega_B$ by $\sim$ 3% at the highest four temperatures, which is within experimental error. We arbitrarily increased $\omega_\circ$ by 3% to agree with $\omega_B$ at high temperatures as indicated by the solid line in Fig.[5-17] (b). At low temperatures, $\omega_B$ is much larger than $\omega_\circ$, which indicates that viscoelastic effects are important in the supercooled liquid.

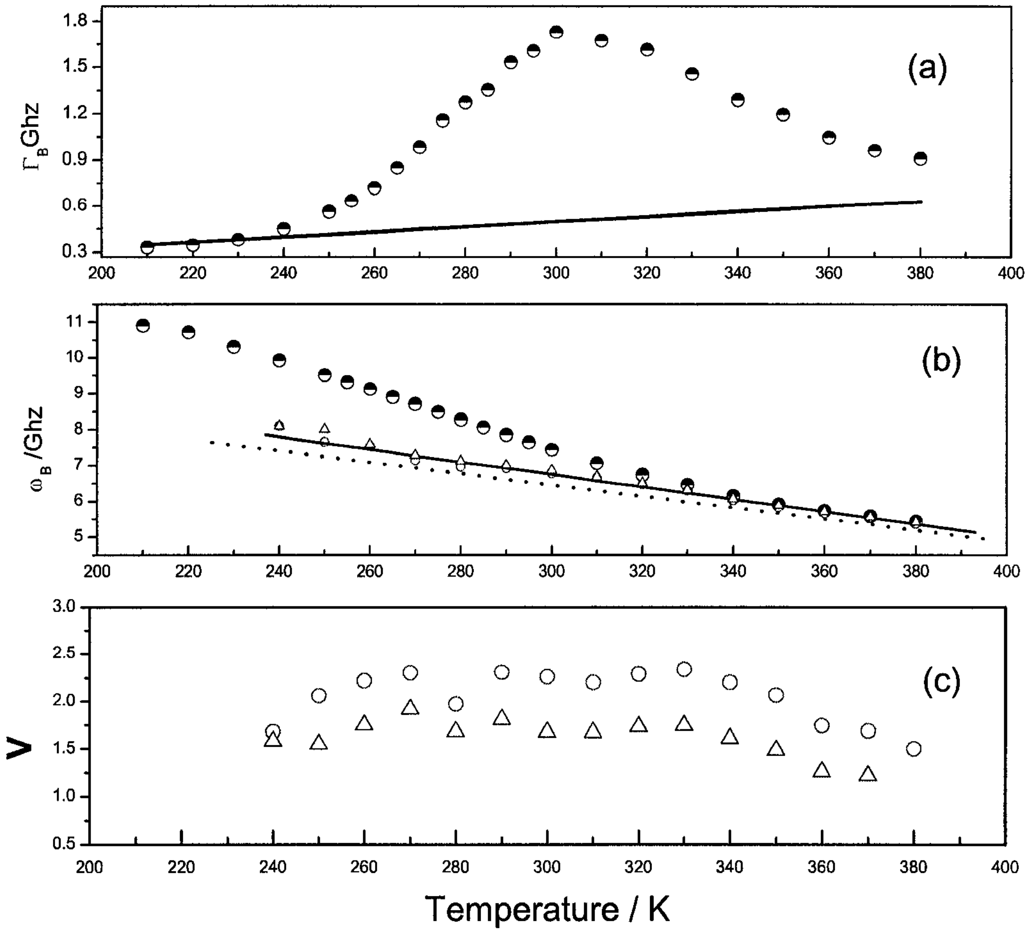

Figure 5-17: Temperature evolution of fitting parameters in VV $90^0$ analysis. (a) half-filled circles are linewidth of brillouin peak obtained from damped oscillator fit; solid line is $T/600$.; (b) half- filled circles are the $\varpi_B$ values from damped oscillator fits to Brillouin peak; Broken line is calculated from ultrasomic data, Solid line is the value in broken line increased by 3%; open circles are $\varpi_0$ values obtained from the full fits, with $\Gamma_0 = T/600$; triagnles are $\varpi_0$ values obtained from the density-only fits, with $\Gamma_0$ $= T/600$ (c) temperature evolution of $V$ from full fits (circles) and density-only fits (triangle) .

### 5.4.2 Fixing $I_0$ and $\Gamma_0$

In the Pick-Franosch theory, Eqs.[5.13] and [5.14], the free fitting parameters are $I_0$, $V$, $\Gamma_0$, $\omega_\circ$ and $S$. The amplitude $I_0$ can be fixed independently. We fit the full $I_{VV}^{90}$ spectrum between 40 and 60 $GHZ$, where the spectrum is purely rotational according to Eq.[5.12], using the parameters for $R(\omega)$ given in Table.[**5.1**]. $I_0$ is the single free fitting parameter and the $I_0$ values obtained from the fits are given in Table.[**5.4**].

The term $\Gamma_0$ in the propagator Eq.[5.14] is conventionally included to represent "regular" anharmonic damping of the sound waves. Since in the deeply supercooled and glassy region the structural relaxation time is so long, the Brillouin linewidth at those temperatures is usually considered to be due to those anharmonic processes. Therefore $\Gamma_0$ can be determined in this temperature region. Since anharmonic damping processes often tend to become stronger with increasing temperature, $\Gamma_0$ may increase with $T$. Brodin *et al* [81] used $\Gamma_0$ proportional to $T$ in analyses of *Propylene Carbonate* Brillouin spectra. We followed the same idea. As shown in Fig.[5-17] (b), we drew a straight line going through the origin and make it match $\Gamma_B$ at the lowest three temperatures ( 210, 220 *and* 230 $K$) as closely as possible. With some arbitrariness, we obtained a relation

$$\Gamma_0 = T/600 \ \ (GHZ) \tag{5.18}$$

shown by the straight line in Fig.[5-17] (a)

Finally we have only three parameters left undetermined for fitting: $V$, $\omega_\circ$ and $S$, where $V$ represents the relative strength of the bulk and shear viscosities, $\omega_\circ$ is the "bare" frequency shift and can be compared to the calculated $\omega_\circ = qC_0$, and $S = \left(\frac{a}{b}\right)\left(\frac{\rho}{\Lambda' z}\right)$ is proportional to the ratio between the scattering strengths from translational and rotational fluctuations. In the next two sections, we will carry out the fits without and with RT coupling in order to evaluate the changes this coupling causes.

### 5.4.3 Density-fluctuation-only fits

The spectral expression for the density-fluctuation-only model is given by Eqs.[5.15] and [5.16]. In the fits, we fix the parameters appearing in $R(\omega)$ from backscattering fits in Table.[**5.1**], $\eta_s(\omega)$ from the $I_{VH}^{90}$ fits in Table.[**5.2**] and Table.[**5.3**] and $\Gamma_0 = T/600$. This is a conventional analysis of Brillouin scattering spectra, similar to that carried out previously for many other materials (e.g. [80], [81], [92], [122], [119]). $A$, $V$, and $\omega_\circ$ are the free parameters. The choice $\Gamma_0 = T/600$, Eq.[5.18], was found to produce values of $\omega_\circ$ shown in Fig.[5-17] (b) as triangles which agree with the adjusted $\omega_\circ$ shown by the solid line. These "density-fluctuation-only" fits are shown in Figs.[5-18] and [5-19] by broken lines. While the fits are generally excellent, for temperatures above 280 $K$ the low-frequency regions of the fits become increasingly less satisfactory because the spectra become negative while the theoretical fits are always positive. We found that that $V \sim 1.9$, independent of temperature, in the temperature range 240 $K$ to 340 $K$, although $\eta_s$ changes by seven orders of magnitude in this range.

### 5.4.4 Fits to the Pick-Franosch theory

Next, we fit the difference spectra using the full theory of Eqs.[5.13] and [5.14]. Similar to the density-fluctuation-only model fits, $\omega_\circ$, $V$, and $S$ are the free fitting parameters. The fit results for 240 $K$ $-300$ $K$ are shown in Fig.[5-19], and for 300 $K$ – 380 $K$ in Fig.[5-18] where we have included both the full fits (solid lines), and the density-fluctuation-only fits (broken lines). At low temperatures the fits are indistinguishable, showing that RT coupling is unimportant in the frequency range of our spectra. At higher temperatures, the low-frequency region is fit much better with the full theory than with the density-fluctuation-only analysis, showing that RT coupling, which is ignored in the conventional density-fluctuation-only analysis, is the source of the negative region. For temperatures below 290 $K$, the effects of RT coupling are limited to frequencies too low to be visible within the spectral window accessible to our

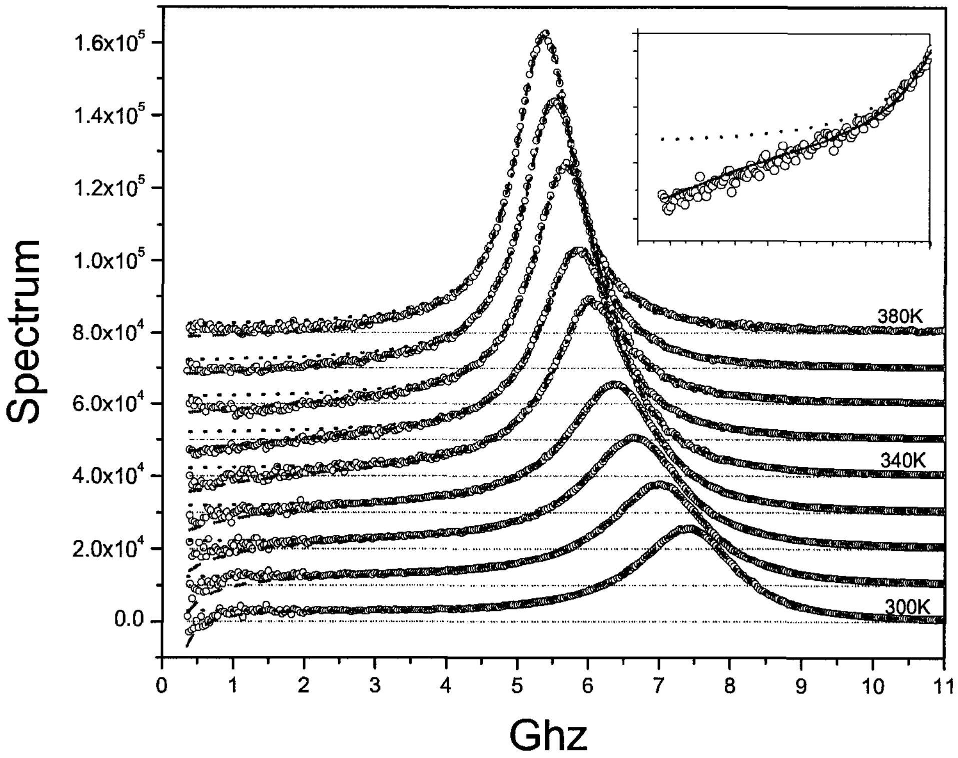

Figure 5-18: Pick-Franosch and density-fluctuation-only fits to the difference spectra at high temperatures. From top to bottom:380 $K$, 370 $K$, 360 $K$, 350 $K$, 340 $K$, 330 $K$, 320 $K$, 310 $K$, 300 $K$. The low frequency part of spectrum at 350 $K$ is shown in inset. (The spectra have been shifted along $Y$ axis for clarity.)

experiments.

The viscosity ratio $V$ computed from these full fits is included in Table.[**5.4**], and is also plotted in Fig.[5-17] (c) as circles. In the temperature range $250 \leq T \leq 350$ $K$, $V \sim 2.2$, indicating that in this region $\eta_s$ and $\eta_b$ are essentially equal ($\eta_b \approx 0.9\eta_s$). The values obtained are similar to, but slightly larger than, those found in the density-fluctuation-only fits, where $V \approx 1.9$. This $\sim$ 15% difference between the two $V$ values can be attributed to the viscosity modification term,$-\frac{4}{3}\Lambda\frac{R^2(\omega)}{1-R(\omega)}$, due to the existence of RT coupling. Although the $V$s are different, the $\omega_\circ$ values obtained in the two approaches are essentially indistinguishable, as shown in Table.[**5.4**] and plotted Fig.[5-17] (b). In Fig.[5-17] (b), we plotted the calculated $\omega_\circ = qC_0$ from the measure refractive index and ultrasonic results. We found that $\omega_\circ$ (circles) from fits match very well the line obtained by moving the calculated $\omega_\circ$ values up by 3%. This fact shows that $\Gamma_0 = 600/T$ is a good estimate. The $S$ parameter, proportional to the ratio between the rotational and translational light-scattering contributions, increases with increasing temperature.

### 5.4.5 Discussion of the VV dip and RT Coupling

The VV dip phenomenon, shown in Fig.[5-18] and in its inset, is a consequence of RT coupling. This coupling effect enters the theoretical $I_{VV}(\omega)$ twice: once in the longitudinal propagator (or response function) $P_L(\omega)$ where it produces the $\eta_s$ reduction, the last term in Eq.[5.14], and also in the optical coupling function $(S+\frac{2}{3}R(\omega))^2$ where $S$ represents the conventional density fluctuation coupling. Both of these modifications have the same physical origin: the uniaxial strain that characterizes a longitudinal acoustic mode is a superposition of compression and shear strain. In liquids composed of anisotropic molecules, the fluctuating longitudinal strain induces rotational fluctuations resulting both in the reduction of $\eta_s$ and the opening of new scattering channel. Referring to the equation of motion for $\overleftrightarrow{Q}$ (Eq.[3.34]), the steady-state solution gives $Q_{ij}$ proportional to the strain rate $\tau_{ij}$. Therefore, for oscillatory LA waves

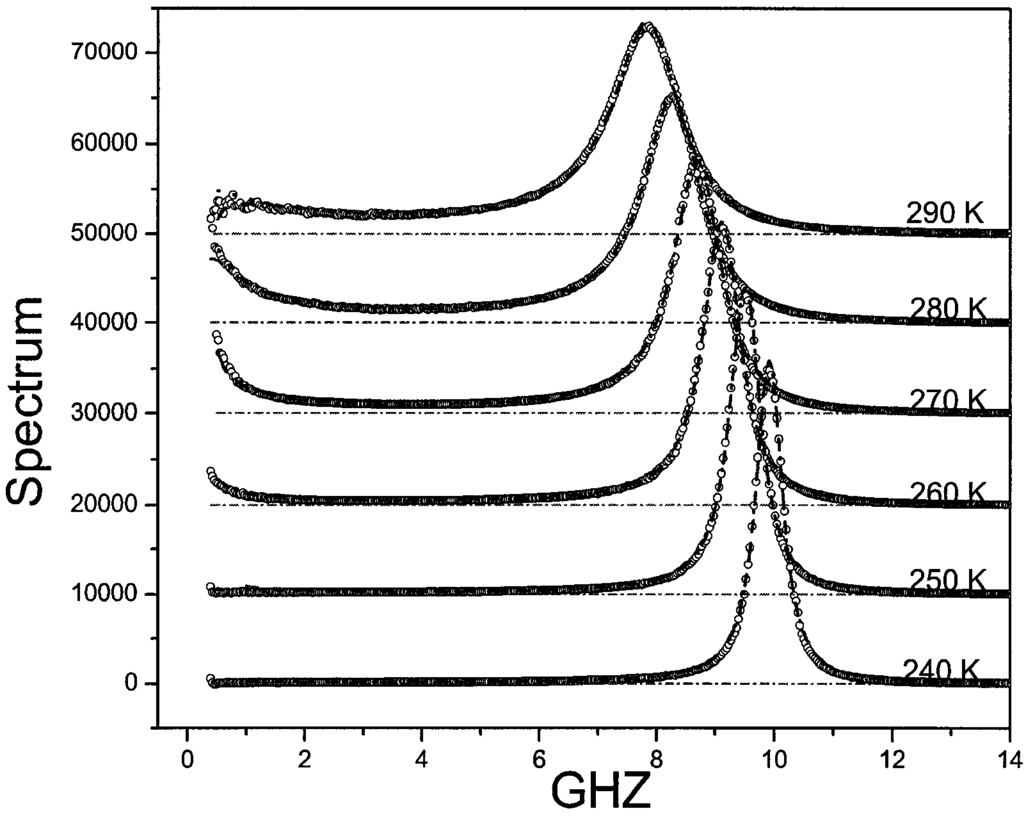

Figure 5-19: Pick-Franosch and density-fluctuation-only fits to the difference spectra at low temperatures. From top to bottom: 290 $K$, 280 $K$, 270 $K$, 260 $K$, 250 $K$, and 240 $K$. (The spectra have been shifted along $Y$ axis for clarity.)

| T ($K$) | $\mathrm{I}_{VH}^{back}$ | Hi-$\omega$-fit | Damped oscil. fit | | Density only | | Full fits | | |
|---|---|---|---|---|---|---|---|---|---|
| | scaling | $I_0$ | $\omega_{\mathrm{B}}$ GHZ | $\Gamma_{\mathrm{B}}$ GHZ | $\omega_{\mathrm{o}}$ GHZ | V | $\omega_{\mathrm{o}}$ GHZ | S | V |
| 380 | 0.158 | 9.46E+5 | 5.41 | 0.94 | 5.41 | 0.984 | 5.36 | 7.41 | 1.42 |
| 370 | 0.179 | 1.02E+6 | 5.57 | 1.04 | 5.55 | 1.21 | 5.51 | 7.47 | 1.69 |
| 360 | 0.170 | 1.04E+6 | 5.73 | 1.09 | 5.70 | 1.26 | 5.66 | 7.35 | 1.75 |
| 350 | 0.165 | 9.65E+5 | 5.92 | 1.13 | 5.88 | 1.48 | 5.83 | 6.97 | 2.07 |
| 340 | 0.175 | 1.01E+6 | 6.13 | 1.31 | 6.06 | 1.61 | 6.02 | 7.01 | 2.20 |
| 330 | 0.155 | 9.43E+5 | 6.46 | 1.50 | 6.31 | 1.74 | 6.28 | 6.90 | 2.34 |
| 320 | 0.162 | 9.44E+5 | 6.75 | 1.65 | 6.51 | 1.73 | 6.47 | 6.85 | 2.29 |
| 310 | 0.173 | 1.01E+6 | 7.09 | 1.70 | 6.70 | 1.67 | 6.63 | 6.67 | 2.20 |
| 300 | 0.166 | 1.05E+6 | 7.49 | 1.66 | 6.87 | 1.68 | 6.77 | 6.56 | 2.25 |
| 290 | 0.15 | 1.06E+6 | 7.90 | 1.50 | 7.01 | 1.81 | 6.92 | 6.11 | 2.31 |
| 280 | 0.174 | 1.10E+6 | 8.30 | 1.21 | 7.12 | 1.68 | 7.10 | 6.05 | 1.97 |
| 270 | 0.167 | 9.94E+5 | 8.72 | 0.967 | 7.28 | 1.91 | 7.18 | 5.72 | 2.30 |
| 260 | 0.178 | 9.41E+5 | 9.13 | 0.769 | 7.59 | 1.75 | 7.51 | 5.03 | 2.21 |
| 250 | 0.214 | 4.50E+5 | 9.52 | 0.625 | 7.81 | 1.71 | 7.79 | 5.24 | 2.06 |
| 240 | 0.218 | 1.79E+5 | 9.93 | 0.520 | 8.10 | 1.68 | 8.10 | 5.10 | 1.68 |

Table 5.4: Fitting parameters from VV analysis

in the low-frequency limit (where $\omega\tau << 1$), if $\delta\rho_{ij}$ is real, then $\delta Q_{ij}$ is imaginary. In this limit, the optical coupling function in Eq.[5.13]

$$C(\omega) = [S + (2/3)R(\omega)]^2 \tag{5.19}$$

becomes

$$[S + \frac{2}{3}R(\omega)]^2 \underset{\omega\to 0}{\longrightarrow} [S + i\omega\frac{2}{3}R_0\beta_R\tau_R]^2 \underset{\omega\to 0}{\longrightarrow} [S^2 + i\omega\frac{4}{3}R_0\beta_R\tau_R]$$

and, Eqs.[5.13] and [5.14] in this limit give,

$$\begin{aligned} I_{dif}(\omega) &\underset{\omega\to 0}{\longrightarrow} \frac{I_0 q^2\Lambda}{\rho\omega_0^4}[S^2\eta_L\frac{q^2}{\rho_0} - S\omega_0^2\frac{4}{3}R_0\beta_R\tau_R] \\ &= \frac{I_0 q^4\Lambda\eta_L S}{\rho\omega_0^4}[\frac{S}{\rho_0} - \frac{4}{3}\frac{\omega_\circ}{q^2}R_0\beta_R\frac{\tau_R}{\eta_L}] \end{aligned}$$

Its first part represents the Mountain mode detected (up to a scaling factor) by the density fluctuations. The second part always decreases the corresponding intensity. In fact, in this low frequency limit, there will be another positive spectrum contribution due to the thermal diffusion mode, which is left out in the Pick-Franosch theory. Thus, although there is always a negative term, it can create a dip only when it is strong enough to reverse the sign of total spectrum by overcoming the positive contributions from Mountain mode and thermal diffusion mode. The appearance of the VV dip therefore requires that the RT coupling and anisotropic light-scattering contribution have to be strong enough. This is the case for salol, but it is certainly not a general rule. If the molecules are not sufficiently anisotropic, there will be no VV dip. This is different from the Rytov dip in the VH spectrum, although the two dips have the same origin. As indicated in Eq.[3.72], the second $q$ dependent part is always negative at low frequencies, which means the Rytov dip always exists in liquids of anisotropic molecules.

Beyond the low-frequency limit, the negative region in the VV dip can be analyzed along the same line. For density-fluctuation only models, the optical coupling function is replaced by a real positive coupling constant. In Eqs.[5.15] and [5.16] for $I(\omega)$, this constant multiplies the imaginary part of $P_L(\omega)$; the real part of $P_L(\omega)$ plays no role. In Eqs. [5.13] and [5.14], with RT coupling included, $C(\omega) = [S+(2/3)R(\omega)]^2$ is complex; the real part of $C(\omega)$ multiplies the imaginary part of $P_L(\omega)$ and the imaginary part of $C(\omega)$ multiplies the real part of $P_L(\omega)$; the sum of these two products determines the spectrum. In Figure.[5-20], we show the 350 $K$ difference spectrum obtained from the fit (top), the *Re* and *Im* parts of $C(\omega)$ (middle), and the *Re* and *Im* parts of $P_L(\omega)$ (bottom). At low frequencies, the imaginary part of $C(\omega)$ is large, and it multiplies the real part of $P_L(\omega)$ which is negative, producing the low-frequency negative region in $I_{dif}(\omega)$.

From Table.[**5.4**], we can see that, for *Salol*, $S$ in the optical coupling function has values from 5.5 to 7, depending on the temperature, and are much larger than $R_0 = 0.9$. This is the reason why the VV dip phenomenon is only observed in low frequencies at high temperature, where $\omega\tau_R \sim 1$ and the imaginary part of $R(\omega)$ has a maximum. While, at lower temperatures, the $\alpha$ peaks of $R(\omega)$ have moved out of our frequency window, which means $\omega\tau_R \gg 1$ and the imaginary part of $R(\omega)$ is very small. Thus no VV dip is observed in our experiment at those temperatures.

We therefore conclude that the VV-dip phenomenon observed in this experiment is indeed a consequence of RT coupling as described by the theory [24], [23]. The reason that it has not been observed previously is suggested by the upper panel of Fig.[5-16] The VV dip is much weaker than the pure rotational background. It is only when the *difference* spectrum is examined that the small low-frequency VV dip becomes apparent.

### 5.4.6 Relation between the Mountain Mode and the VV dip

Besides the VV dip, the Mountain mode is an other important temperature-dependent feature that appears in the IVV-90 spectra. Both of them become much more visible after subtraction of the pure rotational contribution to give $I_{dif}(\omega)$.

The much-studied "Mountain mode", produced by the coupling of the sound wave to structural relaxation, is too narrow to be detected by Brillouin spectroscopy at low temperatures, where $\omega_B\tau_L >> 1$ and $\tau_L$ is the relaxation time appropriate for longitudinal acoustic waves assumed to be equal to $\tau_s$. As $T$ increases, $\omega_B\tau_L$ decreases and the Mountain mode gets broader and detectable for Brillouin spectroscopy. In *Salol,* it first appears at the low-frequency edge of the difference spectrum near $T = 260\ K$ and broadens with increasing $T$. By $T = 300\ K$ it has become a nearly flat contribution on the low-frequency side of the Brillouin peak and then gets weaker above. However, at 300 $K$, the new "VV-dip" phenomenon begins to appear, causing the difference spectrum to become negative at the lowest frequencies. By 350 $K$, the negative VV-dip region extends up to about 2 $GHZ$.

The fact that the Mountain mode appears at lower temperatures than the VV-dip is a result of $\tau_R$, which controls the strength of the VV dip, being about 15 times larger than $\tau_L$ for *Salol.* In reference [23], synthetic spectra were generated using the full theory and were fit with a density-fluctuation-only model with results similar

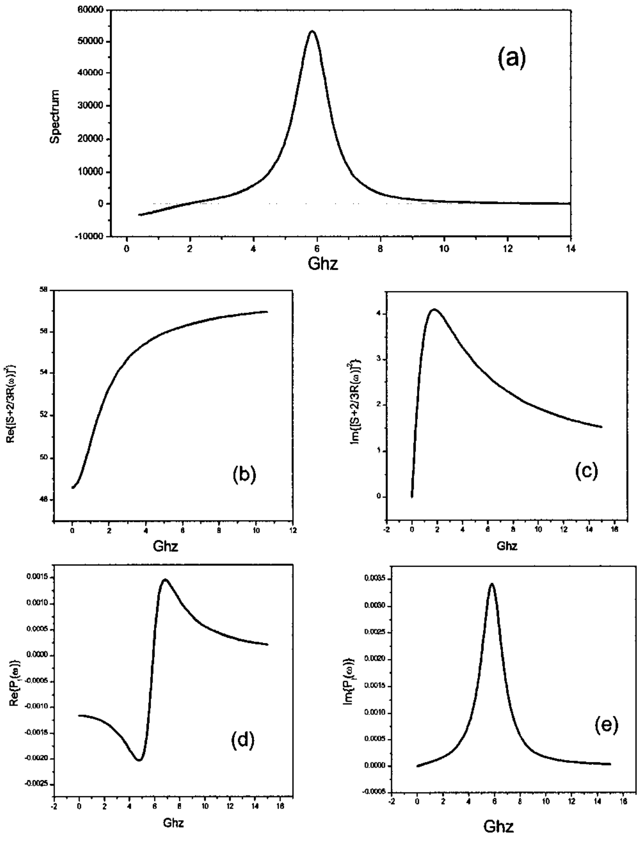

Figure 5-20: Illustration of origin of the VV dip. Top: theoretical fit to the difference spectrum for 350 $K$ $(a)$; Center: real $(b)$ and imaginary $(c)$ part of $[S+(2/3)R(\varpi)]^2$; Bottom: real $(d)$ and imaginary $(e)$ part of the propagator: $P_L\,(\varpi)$.

to those shown here. However, in their calculations, $\tau_L$ and $\tau_R$ were assumed to be equal, so the Mountain mode and the VV-dip occur simultaneously. Fortunately, the large difference between the two relaxation times in *Salol* results in a convenient temperature separation of the two effects.

## 5.5 Comparison with previous experiments

*Salol* has frequently been studied in light-scattering experiments before. The temperature evolution of $I_{VH}^{90}(\omega)$ was first reported by Fablinskii *et al* using photographic detection [2]. They found that the "doublet separation" ( the Rytov dip) can be followed down to 320 $K$ where it disappears, reappearing again (as TA modes) at ~275 $K$. Enright and Stoicheff [99] used photoelectric detection and analyzed their spectra with the two-variable Andersen-Pecora theory [9]. They found that the Rytov dip disappears on cooling at 335 $K$, while the TA modes first appear at ~275 $K$, which is very close to our results. Wang *et al* [16] obtained results for $I_{VH}^{90}(\omega)$ spectrum consistent with those of Enright and Stoicheff. The difference between these results and those of Fabelinskii *et al* is presumably due to differences in instrumental resolution.

Sidebottom and Sorensen performed PCS experiments on *Salol* using small angle scattering (1.1° and 2.3°). For temperatures between 239 K and 218 K they observed a mode - which they designated as the "Mountain mode"- that they fit to the KWW function. The values of $\tau_R$ and $\beta_R$ that they found are in reasonably good agreement with ours with an apparent temperature offset of about 3 $K$. We believe that what they observed was the rotational spectrum which is much more intense that the Mountain mode. The fact that they found values for $\tau_R$ and $\beta_R$ at these small angles similar to those we found at 90° shows that $R(\omega)$ is $q$-independent as we have assumed.

The temperature evolution of the $I_{VV}^{90}(\omega)$ polarized Brillouin spectrum of *Salol* has been studied by Wang *et al* [16] and Dreyfus *et al* [106]. Both experiments found temperature-dependent frequencies and linewidths similar to those reported here. Both, however, analyzed the data assuming that the translational and rotational dynamics produce independent spectra which can therefore be analyzed as a simple superposition. While this procedure gives good fits to the data, the VV-dip phenomenon reported here shows that it is not strictly correct.

# Chapter 6

# Conclusion

Extensive light-scattering experiments, including Brillouin, Raman and photon correlation spectroscopies, have been done to study the rotational and translational dynamics and their coupling in a glassforming liquid of anisotropic molecules, *Salol.* Three sets of Brillouin spectra, VH backscattering, VH 90° and VV 90°, were measured together with VH PCS and Raman spectra, which provide additional information about the rotational dynamics beyond the Brillouin experiments. the Pick-Franosch theory of light-scattering was used to analyzed the data under the assumptions:

1. the susceptibility of pure rotational dynamics $R(\omega)$ and transport coefficients $\eta_b(\omega)$ and $\eta_s(\omega)$ are all modeled by hybrid functions,
2. two ratios of transport coefficients, $\Gamma(\omega)/\mu(\omega)$ and $\eta_b(\omega)/\eta_s(\omega)$, are assumed to be independent of $\omega$.

VH backscattering spectra were first fit by the hybrid function to determine $R(\omega)$. This part of the analysis, together with PCS, fixed all the parameters characterizing the pure rotational dynamics, which were used in VH 90° and VV 90° fittings. The obtained rotational relaxation time $\tau_R(T)$ agrees approximately with dielectric results $\tau_{diel}(T)$ in the literature. With the help of shear viscosity data from the literature, we showed $\eta_s/(\tau_R \cdot T)$ stays constant down to roughly $1.2T_g$ and then increases by a factor about 4 from $1.2T_g$ to $T_g$, indicating a low-temperature separation of the time scales.

In the VH 90° fitting, the 23 spectra were divided into 4 temperature ranges due to their qualitatively different forms. At high temperatures, where clear Rytov dips are observed, the static shear viscosity obtained from the fits agrees with the rheological measurements. In the transition and low temperature range, where the transverse mode is well-developed, the obtained $\tau_s(T)$ values are about 15 times smaller than $\tau_R(T)$, over a temperature range where the relaxation time changes by 12 orders of magnitude. The stretching coefficients for the shear viscosity, $\beta_s$, was found to be smaller than for $\beta_R$. The translation-rotation coupling constant $\Lambda$ was found to increase with decreasing temperature, an effect which is presumably due to the increasing density. In the interpolation range, there is not enough spectral structure for analysis but the parameters interpolated from the parameters in other temperature ranges can still fit the spectra.

The difference spectrum between VV 90° and VH backscattering spectra, are analyzed last with the help of parameters from both VH backscattering and VH 90° fittings. The difference spectrum shows the VV-dip at high temperatures and low frequencies. The difference spectra were first analyzed by a density-fluctuation-only model, which neglects RT coupling. This density-fluctuation-only model can fit difference spectra well except where VV-dip is. However, the Pick-Franosch theory can fit all the difference spectra including the VV-dips. Thus we conclude that the VV-dip is a consequence of RT coupling and related to – but less apparent than – the Rytov dip in VH 90° spectra. The bulk viscosity was found to be proportional to the shear viscosity from 250 $K$ to 350 $K$: $\eta_b(\omega) \simeq 0.9\eta_s(\omega)$. Compared with $\eta_s(\omega)$ obtained from density-fluctuation-only fits, we found the RT coupling reduces the shear viscosity by roughly 15%.

In conclusion, we conclude from the work reported in this thesis : 1. The Pick-Franosch theory can be used to analyze both depolarized and polarized spectra from a glassforming liquids of anisotropic molecules consistently and produces reasonable fitting parameters; 2. The RT coupling does effect the lineshape of the polarized spectrum and leads to a VV-dip at low frequencies of the difference spectrum at high temperatures, which can be described well by the theory.

# Appendix A

# Zwanzig-Mori Formalism

Let's consider a vector space as defined in Sec.[**2.3.2**] Projection operators are defined as:

$$\widehat{P} = \frac{|A(0)\rangle\langle A(0)|}{\langle A(0)|A(0)\rangle}$$

and

$$\hat{Q} = 1 - \widehat{P}$$

. The Zwanzig-Mori Formalism starts from the following identity:

$$\frac{1}{A} - \frac{1}{B} = \frac{1}{A}(B - A)\frac{1}{B}$$

. Thus

$$\frac{1}{A} = \frac{1}{B} + \frac{1}{A}(B - A)\frac{1}{B} \tag{A.1}$$

If we choose $A = s - i\hat{L}$; $B = s - i\hat{Q}\hat{L}$, where $\hat{L}$ is the Liouvillian, then

$$\frac{1}{s - i\hat{L}} = \frac{1}{s - i\hat{Q}\hat{L}} + \frac{1}{s - i\hat{L}}\left(i\hat{P}\hat{L}\right)\frac{1}{s - i\hat{Q}\hat{L}}. \tag{A.2}$$

Eq.[A.2] is called *the Mori identity.* The Laplace transform is usually defined as $F(s) = \int_0^\infty F(t)\exp(-st)\,dt$. If we do Laplace inversion on Eq.[A.2], we have:

$$\exp\left(i\hat{L}t\right) = \exp\left(i\hat{Q}\hat{L}t\right) + \int_0^t d\tau \exp\left(i\hat{L}\tau\right) i\hat{P}\hat{L}\exp\left(i\hat{Q}\hat{L}(t-\tau)\right) \tag{A.3}$$

The time derivative of the dynamic variable $A(t) = \exp\left(i\hat{L}t\right)A(0)$ is:

$$\frac{dA(t)}{dt} = \exp\left(i\hat{L}t\right)\left(i\hat{L}A(0)\right) = \exp\left(i\hat{L}t\right)\left(\widehat{P}+\hat{Q}\right)\left(i\hat{L}A(0)\right) \tag{A.4}$$

Substituting Eq.[A.3] into Eq.[A.4] and replace $\widehat{P}$ with its definition:

$$\frac{dA(t)}{dt} = i\Omega A(t) + \exp\left(i\hat{L}t\right)\hat{Q}\left(i\hat{L}A(0)\right) \tag{A.5}$$

where

$$\Omega = \frac{\langle \hat{L}A(0)|A(0)\rangle}{\langle A(0)|A(0)\rangle} = -i\frac{\left\langle \dot{A}(0)|A(0)\right\rangle}{\langle A(0)|A(0)\rangle}.$$

Replace $\exp\left(i\hat{L}t\right)$ in Eq.[A.5] by Eq.[A.3]:

$$\frac{dA(t)}{dt} = i\Omega A(t) + \exp\left(i\hat{Q}\hat{L}t\right)\hat{Q}i\hat{L}A(0) + \int_0^t d\tau \exp\left(i\hat{L}\tau\right) i\hat{P}\hat{L}\exp\left(i\hat{Q}\hat{L}(t-\tau)\right)\hat{Q}i\hat{L}A(0). \tag{A.6}$$

The second term is usually called the random force

$$F(t) = \exp\left(i\hat{Q}\hat{L}t\right)\hat{Q}i\hat{L}A(0) \tag{A.7}$$

which is a vector orthogonal to $A(0)$ :

$$\langle F(t)|A(0)\rangle = 0\ .$$

Because $\hat{Q}$ is a projection operator, so that $\hat{Q}\hat{Q} = 1$, we have

$$\exp\left(i\hat{Q}\hat{L}t\right)\hat{Q} = \hat{Q}\exp\left(i\hat{Q}\hat{L}t\right)\hat{Q} = \hat{Q}\exp\left(i\hat{Q}\hat{L}\hat{Q}t\right)\hat{Q}$$

which can be verified easily by expansion of the exponential. The term in the integral of Eq.[A.6] contains:

$$i\hat{P}\hat{L}F\left(t\right) = i\hat{P}\hat{L}\hat{Q}F\left(t\right) = \frac{\langle i\hat{L}\hat{Q}F\left(t\right)\left|A(0)\right\rangle}{\langle A(0)|A(0)\rangle}|A(0)\rangle\ .$$

Because $\hat{L}$ and $\hat{Q}$ are Hermitian:

$$\langle i\hat{L}\hat{Q}F\left(t\right)\left|A(0)\right\rangle = -\langle F\left(t\right)\left|\hat{Q}i\hat{L}A(0)\right\rangle = -\langle F\left(t\right)\left|F(0)\right\rangle$$

Thus Eq.[A.6] can be simplified:

$$\frac{dA(t)}{dt} = i\Omega A(t) - \int_{o}^{t} d\tau\Gamma(t-\tau)A(\tau) + F(t)$$

where

$$\Gamma(t) = \frac{\langle F(0)|\exp(-i\widehat{Q}\widehat{L}\widehat{Q}t)|F(0)\rangle}{\langle A(0)|A(0)\rangle}\ .$$

# Appendix B

# Short proof of Eq.[3.74] and its equivalence to conventional Zwanzig-Mori formalism

We can write:

$$\hat{R}(t) = \hat{R}(t)\left(\widehat{P} + \hat{Q}\right) = \hat{R}_P(t) + \hat{R}_Q(t)$$

where $\hat{R}_P(t) = \hat{R}(t)\widehat{P}$ and $\hat{R}_Q(t) = \hat{R}(t)\hat{Q}$. From the equation of motion $\hat{R}(t) = \exp\left(i\hat{L}t\right)$,

$$\partial_t\left(\hat{R}(t)\right) = \hat{R}(t)\, i\hat{L}$$

one finds:

$$\frac{d\hat{R}_Q(t)}{dt} = \hat{R}_P(t)\, i\hat{L}\hat{Q} + \hat{R}_Q(t)\, i\hat{L}\hat{Q} \tag{B.1}$$

Differential equation [B.1] can be solved with the initial condition $\hat{R}_Q(t=0) = Q$:

$$\hat{R}_Q(t) = \hat{Q}\exp\left(i\hat{L}\hat{Q}t\right) + \int_0^t \hat{R}_P(s)\, i\hat{L}\hat{Q}\exp\left(i\hat{L}\hat{Q}(t-s)\right) ds$$

.The first term can be written as:

$$R^{'}(t) = \hat{Q}\exp\left(i\hat{L}\hat{Q}t\right) = \hat{Q}\exp\left(i\hat{Q}\hat{L}\hat{Q}t\right)\hat{Q}\ .$$

Thus collecting terms, we will have Eq.[3.74] :

$$\hat{R}(t) = \hat{R}(t)\hat{P} + \int_{0}^{t}\hat{R}(s)\hat{P}i\hat{L}\hat{R}^{'}(t-s)\,ds + \hat{R}^{'}(t)\ .$$

This equation can be proved to be equivalent to the Mori identity Eq.[A.3]. Inserting Eq.[3.74] into Eq.[A.4]:

$$\frac{dA(t)}{dt} = i\Omega A(t) + B$$

where

$$B = \left\{\hat{R}(t)\hat{P} + \int_{0}^{t}\hat{R}(s)\hat{P}i\hat{L}\hat{R}^{'}(t-s)\,ds + \hat{R}^{'}(t)\right\}\hat{Q}i\hat{L}A(0)\ . \tag{B.2}$$

The First term in Eq.[B.2] vanishes because $\hat{P}$ and $\hat{Q}$ don't overlap. The third term gives the random force $F(t)$ in Eq.[A.7]. The second term can be shown to correspond to the memory term: $\int_{o}^{t} d\tau\Gamma(t-\tau)A(\tau)$, following the same steps as in Appendix A.

# Appendix C

# Note on the static averages

We have chosen the scattering vector to be along the $\hat{z}$ direction, which will bring some simplification. For example, let's consider the following function: $f(x, y, z) = \partial_i G(x, y, z)$, where $i = x \textit{ or } y \textit{ or } z$. Let 's do Fourier transformation on it, according to Eq.[3.37]:

$$\begin{aligned} FT(f(x,y,z)) &= FT(\partial_k G(x,y,z)) \\ &= FT\left(\hat{k}\cdot\nabla G(x,y,z)\right) \\ &= \hat{k}\cdot\vec{q}FT(G(x,y,z)) \\ &= q\delta_{k,z}FT(G(x,y,z)) \end{aligned}$$

Thus quite a few derivative terms will vanish during the Fourier transformation in the derivation in Chapter [**3**], which simplifies the expressions a lot.

# Appendix D

# Relation between parameters in KWW and Cole-Davision functions

In [49], Lindsey *et al* gave the following relations between parameters in the KWW Eq.[2.3] and Cole-Davision Eq.[2.4] functions:

$$\beta_k = \begin{array}{ll} 0.970\beta_{CD} + 0.144 & (\beta_{CD} \in [0.2, 0.6]) \\ 0.683\beta_{CD} + 0.316 & (\beta_{CD} \in [0.6, 1.0]) \end{array}$$

and

$$\tau_K = \tau_{CD}\left(1.184\beta_{CD} - 0.184\right)$$

# Bibliography

[1] B. Berne and R. Pecora *Dynamical light-scattering*, (Wiley, 1976) (Dover, 2000).

[2] I.L. Fabelinskii, L.M. Sabirov, and V.S. Starunov, *Phys. Lett.* **29A**, 414 (1969).

[3] V.S. Starunov, E.V. Tiganov, and I.L. Fabelinskii, *ZhETF Pisma* **5**, 317 (1967) [*Sov. Phys. JETP Lett.* **5**, 260 (1967).

[4] V.S. Starunov and I.L. Fabelinskii, *Zh. Eksp. Teor. Fiz.* **66**, 1740 (1974); *Sov. Phys. JETP* **39**, 854 (1974).

[5] G.I.A. Stegeman and B.P. Stoicheff, *Phys. Rev. Lett.* **54**, 1286 (1964); *Phys. Rev. A.* **1**, 1160 (1968).

[6] M. Leontovich, Izv. *Akad. Nauk. USSR Ser. Fiz.* **5**, 148 (1941), [*J. Phys. USSR* **4**, 499 (1941)]; *Bull. Acad. Sci. USSR Phys. Ser.* **4**, 499 (1941).

[7] S.M. Rytov, *Sov. Phys. JETP* **6**, 401 (1958).

[8] C. Tanford, *Physical Chemistry of Macromolecules* (Wiley, 1961), **p. 436**.

[9] H.C. Andersen and R. Pecora, *J. Chem. Phys.* **54** 2584 (1971), **55**, 1496 (1972).

[10] T. Keyes and D. Kivelson, *J. Chem. Phys.* **54**, 1786 (1971).

[11] T. Keyes and D. Kivelson, *J. Phys. (Paris)* **33**, C1-231 (1972).

[12] T. Keyes and D. Kivelson, *J. Chem. Phys.* **56**, 1876 (1972).

[13] C.H. Wang, *Mol. Phys.* **41**, 541 (1980).

[14] W. Lempert and C.H. Wang, *J. Chem. Phys.* **76**, 1283 (1982); C.H. Wang and Q.-L. Liu, *J. Chem. Phys.* **78**, 4363 (1983).; C.H. Wang, R.J. Ma, G. Fytas, and Th. Dorfmuller, *J. Chem. Phys.* **78**, 5863 (1983).

[15] C.H. Wang and J. Zhang, *J. Chem. Phys.* **85**, 794 (1986); C.H. Wang, *Mol. Phys.* **58**, 497 (1986); C.H. Wang, X.R. Zhu, and J.C. Shen, *Mol. Phys.* **62**, 794 (1987).

[16] C.H. Wang and J. Zhang, *J. Chem. Phys.* **85**, 794 (1986).

[17] C. Dreyfus, A. Aouadi, R.M. Pick, T. Berger, A. Patkowski, and W. Steffen, *Europhys. Lett.* **42**, 55 (1998); *J. Phys. Condens. Matt.* **11**, A139 (1999).

[18] C. Dreyfus, A. Aouadi, R.M. Pick, T. Berger, A. Patkowski, and W. Steffen, *Eur. Phys. J. B* **9**, 401 (1999).

[19] C. Dreyfus and R.M. Pick, *unpublished.* (Draft: Nov 2001).

[20] C. Dreyfus, A. Aouadi, J. Gapinski, M. Matos-Lopes, W. Steffen, A. Patkowski, and R. M. Pick, *Phys. Rev. E* **68**, 011204 (2003).

[21] G. Monaco *et al* 2003 (in preparation).

[22] P.J. Chappell and D. Kivelson, *J. Chem. Phys.* **76**, 1742 (1982).

[23] R.M. Pick, T. Franosch, A. Latz, and C. Dreyfus, *Eur. Phys. J. B* **31**, 217 (2003); (Cond-Mat/0209204).

[24] T. Franosch, A. Latz, and R.M. Pick, *Eur. Phys. J. B* **31**, 229 ( 2003); (Cond-Mat/0209205).

[25] Zarzycki, J, *Glass and the vitreous state* ( Cambridge: Cambridge University Press)

[26] Greer, *Science* **267**, 753-756 (1995).

[27] J.M.V. Blashard P. Lillford (eds) *The Glassy State in Foods* (Nottingham Univ.Press, Nottingham, 1993).

[28] J.H. Crowe, J.F. Carpenter, & L.M Crowe, *Annu.Rev.Physiol.* **60**, 73-103 (1998).

[29] P.G. Debenedetti *Metastable liquids, Concepts and Principles* (Priceton Univ. Press, Princeton, 1996).

[30] C.A. Angel *Science* **267** 1924 (1995).

[31] M.D. Ediger, C.A. Angell, S.R. Nagel, *J.Phys.Chem.*, **100.** 13200 (1996).

[32] C.A. Angel, K.L. Ngai, G.B. Mckenna P.F. McMillan and S.W. Martin, *J.App.Phys.* **88**, 3113 (2000).

[33] P.Lunkenheimer, U. Scheider, R.Brand and A.Loild *Contemp.Phys.* **41** 15 (2000).

[34] P.G. Debenedetti and F.H. Stillinger *Nature* **410**, 259(2001).

[35] F.H. Stillinger, *Science* **267** 1935(1995).

[36] M. Goldstein, *J. Chem. Phys.* **51**, 3728 (1969).

[37] F.H. Stillinger and T. A. Weber, *Phys. Rev. A.* **25**, 978 (1982).

[38] S Sastry, P.G. Debenedetti, F.H. Stillinger, *Nature* **393**, 554 (2000).

[39] L. Angelani, R. Di Leonardo, G. Ruocco, A. Scala, and F. Sciortino, *Phys. Rev. Lett.* **85**, 5356 (2000).

[40] K. Broderix, K. K. Bhattacharya, A. Cavagna, A. Zippelius, and I. Giardina, *Phys. Rev. Lett.* **85**, 5360 (2000).

[41] T. S. Grigera, A. Cavagna, I. Giardina and G. Parasi, *Phys. Rev. Lett.* **88**, 55502 (2002).

[42] A. Liu and S. R. Nagel, (eds.), *Jamming and Rheology: Constrained Dynamics on Microscopic and Macroscopic Scales*, Taylor & Francis, London, (2001).

[43] A. J. Liu and S. R. Nagel, *Jamming is not Just Cool Any More* Nature **396**, 21 (1998).

[44] H. A. Makse, J. Brujic and S. F. Edwards, *Statistical Mechanics of Jammed Matter: Jamming is even cooler than you thought*, to be published.

[45] C.A. Angel *J. Non.-Cryst. Solids.* **13,** 131, (1991).

[46] N. Menon and S. R. Nagel *Phys. Rev. Lett.* **74**, 1230-1233 (1995).

[47] M.H. Cohen and G.S. Grest, *J. Non-Cryst. Solids* **61-62**, 749 (1984); G.S. Grest and M.H. Cohen, *Adv. Chem. Phys.* **48**, 455 (1981).

[48] W. Kob and H. C. Anderson, *Phys. Rev. E* **52** 4134 (1996).

[49] C.P. Lindsey and G.D. Patterson, *J. Chem. Phys.* **73**, 3348 (1980).

[50] C.A. Angel and J. C. Tucker, *J. Chem. Phys.* **78**, 278 (1974).

[51] R. Richert, *J. Non.-Cryst. Solids*, **172**, 209 (1994).

[52] M.T. Cicerone, M.D. Ediger, *J. Chem. Phys.* **105**, 10521 (1996).

[53] I. Chang and H. Sillescu, *J. Phys. Chem. B*, **101**, 8794 (1997).

[54] L. A. Deschenes and D. A. Vanden Bout, *Science*, **292**, 255 (2001).

[55] C. Donati, S.C. Glotzer,P.H Poole, *Phys. Rev. Lett.* **82**, 5064, 21 (1999); N. Lacevic, F.W. Starr, T.B. Schrder, S.C. Glotzer, *J. Chem. Phys.* **119**, 7372, (2003).

[56] M.D. Ediger Annu., *Rev. Phys. Chem.* **51**, 99 (2000).

[57] F. Fujura, B. Geil, H.H. Sillescu, and G. Fleisher., *Z.Phys.B Cond. Matt.* **88** 195(1992).

[58] N. Menon, S. R. Nagel, and D. C. Venerus, *Phys. Rev. Lett.* **73**, 963 (1994).

[59] P.W. Anderson,, *Science* **267**, 1615(1995).

[60] J. H. Gibbs *J. Chem. Phys.* **25**, 185 (1956); J. H. Gibbs and E.A. DiMarzio, *J. Chem. Phys.* **28**, 373 (1958).

[61] W. Gotze in *Liquids, Freezing and the Glass Transition*, eds J.P. Hansen et al, North-Holland, Amsterdam (1989).

[62] J. P. Boon and S. Yip *Molecular Hydrodynamics* (McGraw-Hill 1980) (Dover 2000).

[63] L. E. Reichl *A Modern Course in Statistical Physics*, (University of Texas Press 1980).

[64] H.Z. Cummins, *J. Phys.: Condens. Matt.* **11** A95 (1999).

[65] W. Gotze and L. Sjogren, *Rep. Prog. Phys.* **55**, 241 (1992).

[66] K. Kawasaki *Ann. Phys., NY* **61** 1; *Phys. Rev.* **150** 291 (1966).

[67] Bengtzelius U *Phys. Rev. A* **34** 5059 (1986).

[68] T. Franosch, M. Fuchs, W. Götze, M. R. Mayr and A. P. Singh *Phys. Rev. E.* **55**, 7153 (1997).

[69] M. Fuchs, *Transport Theory Stat. Phys.* **24,** 855 (1995).

[70] L. Fabbian, W. Götze, F. Sciortino, P. Tartaglia and F. Thiery, *Phys. Rev. E.* **59,** R1347 (1998).

[71] Sow-Hsin Chen, Wei-Ren Chen and Francesco Mallamace, *Science*, **300**, 619-622 (2003).

[72] K. N. Pham *et al., Science,* **296**, 104 (2002).

[73] S. P. Das and G. F. Mazenko, *Phys. Rev. A* **34**, 2265 (1986).

[74] W. Gotze and L. Sjogren, *J. Phys. C* **21**, 3407 (1988).

[75] C. Donatil, S. C. Glotzer, P. H. Poole, W. Kob, and S. J. Plimpton *Phys. Rev. E* **60**, 3107 (1999).

[76] H.Z. Cummins,G Li,W. Du, Y.H. Hwang and G.Q. Shen *Prog. Theor. Phys. Suppl.* **126** 21 (1997).

[77] P. Lunkenheimer, A. Pimenov and A. Loidl, *Phys. Rev. Lett.* **78** 2995 (1997).

[78] G. Li, W.M. Du, X. K. Chen, H.Z. Cummins and N.J. Tao *Phys. Rev. A* **45** 3867 (1992).

[79] W. van Megen and S. Underwood *Phys. Rev. E* **47** 248 (1993).

[80] S.V. Adichtev, St. Benkhof, Th. Blochowitz, V.W. Novikov, E. Rossler, Ch. Tschirwitz, and J. Wiedersich, *Phys. Rev. Lett.* **88**, 055703 (2002).

[81] A. Brodin, M. Frank, S. Wiebel, G.Q. Shen,1, J. Wuttke and H. Z. Cummins *Phys. Rev.E* 65, 051503 (2002).

[82] Rayleigh, Lord, *Phil. Mag.* **41**, 107, 274, 447 (1871); *ibid*, 12, 81 (1881).

[83] M. Smoluchowski, *Ann. Phys.* **25**, 205 (1908).

[84] A. Einstein, *Ann. Phys.* **33**, 1275 (1910).

[85] L. Brillouin, *Comptes Rendus* **158**, 1331 (1914); *Ann. Phys.* **17**, 88 (1922).

[86] E. Gross *Nature* **126,** 201 (1930); **129**, 722 (1932).

[87] L., Landau and G. Plazcek *Phys. Zeit. Sow.* **5**, 172 (1934).

[88] R.D. Mountain, *Rev. Mod. Phys.* **38**, 205 (1966); *J. Res. Natl. Bur. Standards* **72A**, 95 (1968).

[89] P. M. Chaiken and T. C. Lubensky, *Principles of condensed matter physics* ( Cambridge 1995).

[90] L. D. Landau and E. M. Lifshitz, *Fluid Mechanics*, Addison-Wesley, Reading, Mass.(1960).

[91] M.G. Schultz and T. Franosch, in preparation.

[92] D. Fioretto, L. Comez, G. Socino, L. Verdini, S. Corezzi, and P.A. Rolla, *Phys. Rev. E* 59, 1899 (1999); G. Monaco, L.Comez, and D. Fioretto, *Philos. Mag. B* 77, 463 (1998); D. Fioretto, M. Mattarelli, C. Masciovecchio, G. Monaco, G. Ruocco, and F. Sette, *Phys. Rev. B* **65**, 224205 (2002); D. Fioretto, C. Masciovecchio, M. Mattarelli, L. Palmieri, G. Ruocco, and F. Sette, *Philos. Mag. B* **83**, 273 (2002).

[93] G. Monaco, D. Fioretto, L. Comez, and G. Ruocco, *Phys. Rev.E* **63**, 061502 (2001).

[94] J. Frenkel *Kinetic Theory of Liquids* (Dover, 1955).

[95] M. Born and E. Wolf, *Principles of Optics* 5th ed. Pergamon Press, Oxford, (1975).

[96] D.S. Bedboroagh and D.A. Jackson, J. Phys. E, 11, 473 (1978).

[97] J.R. Sandercock, in "*Proc. 2nd Int. Conf. on light-scattering in Solids*" edit by Balkanski, (1971).

[98] J.R. Sandercock, *Solid State Commun.* 26 547 (1978).

[99] G.D. Enright and B.P. Stoicheff, *J. Chem. Phys.* **64**, 3658 (1976).

[100] NIST Chemistry WebBook, http://webbook.nist.gov/chemistry/.

[101] L.M. Sabirov, V.S. Starunov, and I.L. Fabelinskii, *Zh. Eksp. Teor. Fiz.* **60**, 146 (1971); *Sov. Phys. JETP* **33**, 82 (1971).

[102] C. Vaucamps, J.P. Chabrat, L. Letamendia, G. Nouchi, and J. Rouch, *Optics Communications* **15**, 201 (1975).

[103] V.O. Jantsch, *Z. Kristallogr.* **108**, 185 (1956).

[104] M. Cukierman, J.W. Lane, and D.R. Uhlmann, *J. Chem. Phys.* **59**, 3639 (1973).

[105] W.T. Laughlin and D.R. Uhlmann, *J. Phys. Chem.* **76**, 2317 (1972).

[106] C. Dreyfus, M.J. Lebon, H.Z. Cummins, J. Toulouse, B. Bonello, and R.M. Pick, Phys. Rev. **69**, 3666 (1992); **76**, 1763 (1996).

[107] G. Li, W.M. Du, A. Sakai, and H.Z. Cummins, *Phys. Rev. A* **46**, 3343 (1992).

[108] G. Hinze, D.B. Brace, S.D. Gottke, and M.D. Fayer, *J. Chem. Phys.* **113**, 3723 (2000).

[109] Y. Yang and K.A. Nelson, *Phys. Rev. Lett.* **74**, 4883 (1995).

[110] H.Z. Cummins, W.M. Du, M. Fuchs, W. Gotze, S. Hildebrand, A. Latz, G. Li, and N.J. Tao, *Phys. Rev. E* **47**, 4223 (1993).

[111] H.Z. Cummins, G. Li, W.M. Du, R.M. Pick, and C. Dreyfus, *Phys. Rev. E* **53**, 896 (1996); **55**, 1232 (1997).

[112] P.K. Dixon, L. Wu, S.R. Nagel, B.D. Williams, and J.P. Carini, *Phys. Rev. Lett.* **65**, 1108 (1990).

[113] F. Stickel, E.W. Fischer, and R. Richert, J. Chem. Phys. **102**, 6251 (1995).

[114] D.L. Sidebottom and C.M. Sorenson, *Phys. Rev. B* **40**, 461 (1989).

[115] S.-H. Chong and W. Gotze, *Phys. Rev. E* **65**, 051201 (2002); S.-H. Chong and W. Gotze *Phys. Rev. E* **65**, 041503 (2002).

[116] S.-H. Chong, W. Gotze, and A. P. Singh *Phys. Rev. E* **63**, 011206 (2001).

[117] W. Gotze, A.P. Singh and Th.Voigtmann *Phys. Rev. E.* **61**, 6934 (2000).

[118] C. Dreyfus, M.J. Lebon, F. Vivicorsi, A. Aouadi, R.M. Pick, and H.Z. Cummins, *Phys. Rev. E* **63**, 041509 (2001).

[119] J. Wiedersich, N. Surovtsev, and E. Rossler, *J. Chem. Phys.* **113**, 1143 (2000).

[120] J. Wiedersich, *private communication* (2002).

[121] H. Cang, V.N. Novikov, and M. D. Fayer,*Phys. Rev. lett* **90**, 197401 (2003); *J. Chem. Phys.* **118**, 2800 (2003).

[122] L. Gomez, D. Fiorreto, and F. Scaponi, and G. Monaco, *J. Chem. Phys.* **119**, 6032 (2003).